

5

LEED Theory

Basic Formalisms

As mentioned in Section 2.2, a kinematic, that is, single-scattering, theory of LEED cannot describe experimental intensities with an accuracy that is sufficient to determine atomic positions and other non-structural information about surfaces. This degree of accuracy requires the inclusion of multiple scattering at a level of sophistication that is similar to that of electronic band structure calculations; in fact, some early versions of LEED theory employed methods of 3-D band structure theory, such as Bloch waves and pseudopotentials. However, the goal of surface structure determination by iterative optimisation of atomic positions with lower-dimensional periodicity and sometimes large 2-D unit cells requires very efficient calculational schemes of the multiple scattering of electrons.

This chapter reviews the main methods of LEED theory in recent use. More complete descriptions of the variety of basic methods developed for LEED can be found in earlier publications [5.1–5.3]. After basic geometrical considerations in Section 5.1, our account describes low-energy electron scattering by a single atom in terms of phase shifts in Section 5.2.1. The treatment of multiple scattering using plane waves and spherical waves is addressed in Section 5.2.2. This approach is then applied to the scattering by clusters of atoms in Section 5.2.3, and in particular to nanoparticles (NanoLEED) in Section 5.2.4. Electron scattering by 2-D infinite monolayers and multilayers of atoms is described in Section 5.2.5, with both exact and iterative schemes. This is followed in Section 5.2.6 by 2-D layers of finite or infinite thickness, representing the surface of bulk crystals.

Symmetry plays an important role, not only in terms of understanding and classifying structures, but also in accelerating the computations and reducing computer memory usage and is, therefore, extensively treated in Section 5.3. Approximations can also greatly reduce computational efforts and are described in Section 5.4 for tensor LEED (TLEED), frozen LEED and diffuse LEED (DLEED). Section 5.5 discusses thermal effects and, to some extent, structural disorder, which must be taken into account for accurate structure determination. Chapter 6 continues the treatment of LEED theory for special categories of materials and structures, including quasicrystals and modulated structures. Chapter 6 also addresses the practical issues involved in actual quantitative structural determination.

5.1 Diffraction Geometry

The most common experimental approach to LEED consists of a well-collimated (i.e., ‘parallel’) beam of near-mono-energetic electrons incident on a flat surface. If the surface is periodic, as is often the case with the surface of a single crystal, such geometry creates a series of well-collimated diffracted beams yielding a pattern of sharp spots on a display. If such a surface has long-range disorder, as in a poorly ordered overlayer of added atoms or molecules, the diffraction pattern will have diffuse intensity distributed between any spots due to ordered parts of the surface. The case of a quasicrystal surface produces a pattern with sharp spots.

For studying nanostructures it may also be useful to consider a convergent beam that is focused on a particular nanoscale region of a surface, for example a nanoparticle supported by a surface. One may also direct a collimated beam onto a single nanostructure and observe the diffusely scattered electrons. We shall in this chapter describe methods for calculating LEED intensities for all these different kinds of geometry.

For a collimated beam incident on a planar surface, the beam is normally represented in the vacuum outside the surface as a plane wave $e^{i\mathbf{k}_0\mathbf{r}}$ with wave vector \mathbf{k}_0 , see Figure 5.1.

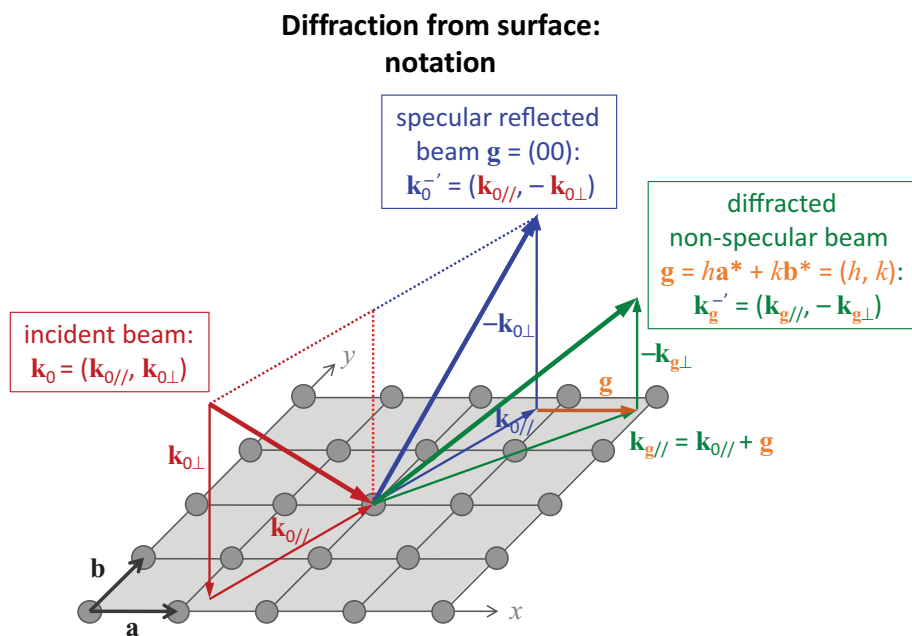


Figure 5.1 Diffraction from a periodic surface with 2-D lattice vectors \mathbf{a} and \mathbf{b} (grey). The beam incident \mathbf{k}_0 on the surface (red) is specularly reflected into the (00) beam (blue); it also diffracts into non-specular beams \mathbf{k}_g^- (green), where \mathbf{g} (orange) is any 2-D reciprocal lattice vector (h, k) .

We have

$$|\mathbf{k}_0| = \frac{\sqrt{2m_e E}}{\hbar} = \frac{2\pi}{\lambda}, \quad \mathbf{k}_0 = (k_{0x}, k_{0y}, k_{0z}), \quad (5.1)$$

$$k_{0x} = |\mathbf{k}_0| \cos \varphi \sin \vartheta, \quad k_{0y} = |\mathbf{k}_0| \sin \varphi \sin \vartheta, \quad k_{0z} = |\mathbf{k}_0| \cos \vartheta,$$

where E and m_e are the kinetic energy and mass of the electron, respectively, while ϑ and φ are the polar and azimuthal angles of \mathbf{k}_0 with respect to the surface normal and the x -axis, respectively.

As explained in Chapter 2, a 2-D periodic surface structure with a 2-D reciprocal lattice (\mathbf{a}^* , \mathbf{b}^*) causes diffracted plane waves (beams) $A_{\mathbf{g}} e^{i\mathbf{k}_{\mathbf{g}} \mathbf{r}}$ with wave vectors $\mathbf{k}_{\mathbf{g}}$, such that $|\mathbf{k}_{\mathbf{g}}| = |\mathbf{k}_0|$ (for energy conservation), and $\mathbf{k}_{\mathbf{g}} = \mathbf{k}_0 + \mathbf{g} = (k_{0x} + g_x, k_{0y} + g_y, k_{0z})$ (due to parallel momentum exchange with the surface), where $\mathbf{g} = 2\pi(h\mathbf{a}^* + k\mathbf{b}^*)$ (to satisfy Laue conditions in 2-D), see Figure 5.2. The indices h and k are often used to label the diffracted beams, for example, the beam (h, k) ; h and k are often integers, for example, beams $(0, 0)$ or $(2, 1)$, and can be fractional in the presence of superlattices, for example, $(1/2, 0)$ or $(1/4, 3/4)$. As a result of energy conservation, we have in the vacuum outside the surface:

$$k_{\mathbf{g}_z}^{\text{outside}} = -\sqrt{\left(\frac{2\pi}{\lambda}\right)^2 - (k_{0x} + g_x)^2 - (k_{0y} + g_y)^2}$$

$$= -\sqrt{\frac{2m_e E}{\hbar^2} - (k_{0x} + g_x)^2 - (k_{0y} + g_y)^2}. \quad (5.2)$$

Diffraction from atomic layer: notation

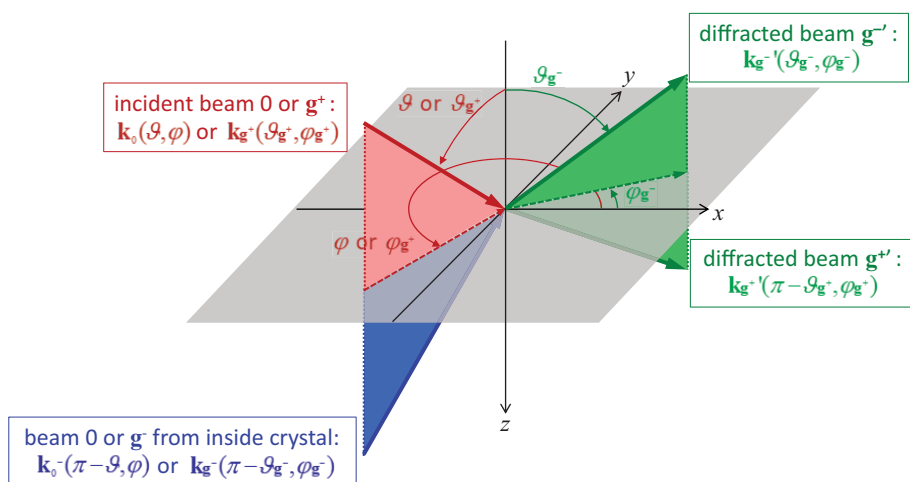


Figure 5.2 Diffraction from a 2-D periodic layer (grey), showing typical nomenclature for beams and angles. The + and – signs refer to beam propagation into versus out of the crystal, respectively; primes indicate scattered (reflected or diffracted) beams. The incident beam (red) can arrive directly from the electron source (\mathbf{k}_0) or may have already been diffracted by an atomic layer above it ($\mathbf{k}_{\mathbf{g}}^+$). The beam incident from inside the crystal (blue) may have been specularly reflected from a deeper layer (\mathbf{k}_0^-) or may have been otherwise diffracted from a deeper layer ($\mathbf{k}_{\mathbf{g}}^-$).

The negative sign in front of the square root signifies a wave travelling away from the surface into vacuum. If the argument of the root is positive, we obtain a propagating wave that can reach a distant external detector. However, if the argument is negative, due to large $|g_x|$ or $|g_y|$, the wave becomes evanescent (exponentially decaying): it travels parallel to the surface and cannot reach a distant detector.

Inside the surface, the LEED electrons feel a different energy due to any electric dipole layer present at the surface (this dipole layer is related to the work function that keeps the material's electrons from spilling out of a surface): this manifests itself as an upward energy shift by the 'inner potential', V_0 , relative to vacuum. This inner potential may depend on the electron energy.

In addition, LEED electrons can suffer energy losses to the material; those electrons that lose energy are removed from consideration, since we assume measurement at the same energy as the nominal incident beam's energy, that is, we only follow electrons that undergo elastic scattering. This loss of electrons to inelastic processes is commonly represented by a damping of the LEED wave amplitudes through an imaginary part of the inner potential, iV_{0i} , or, equivalently, by an inelastic mean free path (IMFP), which severely limits the penetration depth of electrons into the surface. The imaginary part of the inner potential usually depends on the electron energy, for example rising with energy to represent a decreasing inelastic mean free path. The imaginary part of the inner potential is the main contributor to the energy width of peaks in $I(V)$ curves (other contributions come from the energy spread of the electron source and the energy resolving grids, as well as simple overlap of neighbouring peaks).

As a result, the LEED electron's energy, which is E in vacuum, becomes complex inside the surface: $E + V_0 + iV_{0i}$. We obtain, inside the material, a wave vector with unchanged components parallel to the surface ($k_{0x} + g_x, k_{0y} + g_y$) and a modified complex component perpendicular to the surface:

$$k_{gz}^{\text{inside}} = -\sqrt{\frac{2m_e}{\hbar^2}(E + V_0 + iV_{0i}) - (k_{0x} + g_x)^2 - (k_{0y} + g_y)^2}. \quad (5.3)$$

Inside the surface all 'plane' waves decay exponentially in the directions perpendicular to the surface, due to damping, in addition to the exponential decay whenever $|g_x|$ or $|g_y|$ is large. All of these waves can potentially reach and transmit electrons from one atomic layer to the next. However, the larger $|g_x|$ and $|g_y|$ are, the stronger the exponential decay will be: as a result, we can truncate the number of plane waves used, especially when layer spacings are large. For smaller layer spacings, plane waves with larger $|g_x|$ and $|g_y|$ can reach from layer to layer and must therefore be included; in fact, this growth in number of plane waves rapidly becomes computationally unstable, so that one must avoid using plane waves with small layer spacings. The solution is to use spherical waves in small layer spacings, that is, to combine such closely-spaced atomic planes into a layer with two or more atomic planes, within which a spherical-wave treatment is performed.

Consequently, most LEED formalisms represent a surface as one or more 2-D infinite slabs of finite thickness; these slabs are separated by layer spacings of at least

about 0.1 nm (1 Å). Within slabs, spherical waves are used, while between and outside slabs plane waves are used. We will describe both cases in the following.

5.2 Scattering Theory

We shall stepwise build a scattering theory by starting with the simplest scatterer, a single atom. We then consider electron multiple scattering from a cluster of several atoms: this will lead in particular to diffraction from nanoparticles. In this section, we will discuss the case of a 2-D periodic layer of atoms, an important ingredient of extended surfaces. We shall then assemble such atomic layers into a surface that is thick enough to include the penetration depth of LEED electrons.

We shall assume that a collimated incident electron beam can be represented by a plane wave and that the scattering of LEED electrons is elastic. The case of a convergent LEED beam will be allowed and represented as a linear combination of a continuous set of plane waves; this case will be discussed in the context of diffraction from nanoparticles.

We shall ignore electron spin and magnetic effects. These assumptions have proved adequate to match theory to experiment for the vast majority of surfaces studied.

We also adopt the successful muffin-tin model of the scattering by a solid, chosen for its computational efficiency. This model represents each atom core as a spherically symmetric potential, as sketched in Figure 5.3, which also shows common terminology. The potential within the ‘muffin radius’ of each atom is frequently derived from atomic or band structure calculations, as described briefly in Section 2.2.3. Section 6.1.6 gives methods to calculate the ‘muffin-tin potential’ for the individual

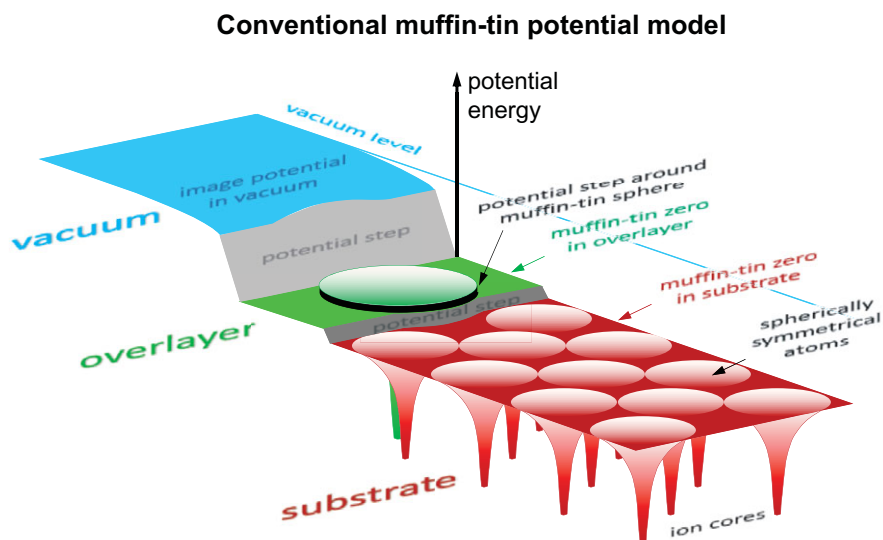


Figure 5.3 Schematic drawing of the LEED muffin-tin potential, indicating terminology

atoms from the free atom potentials and the surrounding potentials in the surface slab; there we also describe a new method that avoids artificial potential steps (Section 6.1.6.3), such as the potential step shown in Figure 5.3 surrounding the adatom in the overlayer (such steps are also frequent in more complex substrates, e.g., covalent, compound and ionic materials, but are unusual in close-packed metallic substrates, as illustrated in Figure 5.3).

Usually, the radii of the muffin-tin spheres have been chosen so that they just touch each other, but overlapping spheres are helpful, as discussed in Section 6.1.6.3. Between these atomic spheres are regions of constant potential: usually a single constant potential value, called muffin-tin zero or muffin-tin constant, or also inner potential, suffices for the entire material, especially in compact materials; in more complex cases different values can be given to different layers parallel to the surface, for example in overlayers of adatoms or admolecules, leading to potential steps between layers. This muffin-tin constant ends with a more or less abrupt potential step outside the surface, where the potential rises gradually to the vacuum level in the form of the image potential. While these potential steps outside the surface and between layers produce both reflection and refraction (change of direction), the reflection is relatively weak and usually neglected, except in very low energy electron diffraction (VLEED).

5.2.1 Atomic Scattering: Phase Shifts

It is convenient to use the phase shift formalism to describe plane-wave scattering by the spherical atomic scattering potential of the muffin-tin model, as follows. A plane wave e^{ikr} is scattered by a single atom into an outgoing wave $f(\vartheta)\frac{e^{ikr}}{r}$, centred on that atom, in the asymptotic limit of large distances r from the scatterer; here ϑ is the scattering angle. The scattering factor $f(\vartheta)$ for a spherical potential can be expressed in terms of a series of ‘spherical’ waves (more properly called ‘partial’ waves, centred on the atom) with amplitudes t_l given by the phase shifts δ_l according to:

$$f(\vartheta) = -4\pi \sum_{l=0}^{\infty} (2l+1)t_l P_l(\cos \vartheta), \quad t_l = -\frac{\hbar^2}{2m_e} \frac{1}{2ik} (e^{2i\delta_l} - 1) = -\frac{\hbar^2}{2m_e} \frac{1}{k} \sin \delta_l e^{i\delta_l}, \quad (5.4)$$

where P_l are Legendre polynomials. The amplitudes t_l are elements of the so-called t -matrix \mathbf{t} . In practice, the series over the angular quantum number l can be truncated at $l = l_{\max} \sim 5$ to 10 for common LEED energies up to about 400 eV. Such phase shifts depend on the atomic element (and also on its ionic charge), as well as on the electron energy. The phase shifts themselves are obtained by numerical integration of the radial Schrödinger equation within the spherical atomic potential from the origin at $r = 0$ to the muffin-tin radius r_m , where the radial wave function has the resulting value $R_l(r_m)$ and radial derivative $R'_l(r_m)$:

$$e^{2i\delta_l} = \frac{L_l h_l^{(2)}(kr_m) - h_l^{(2)'}(kr_m)}{h_l^{(1)'}(kr_m) - L_l h_l^{(1)}(kr_m)}, \quad L_l = \frac{R'_l(r_m)}{R_l(r_m)}. \quad (5.5)$$

Here $h_l^{(1)}$ and $h_l^{(2)}$ are spherical Hankel functions of the first and second kinds, respectively; their radial derivatives $h_l^{(1)'}$ and $h_l^{(2)'}$ are also used.

For a spherical atomic potential, the matrix \mathbf{t} is diagonal, with elements $t_{lm,l'm'} = t_l \delta_{ll'}$ (using the Kronecker symbol, with value 1 when $l = l'$ or 0 otherwise, and the magnetic quantum number $m = -l, \dots, l$). The spherical atomic potential needed for the integration of the radial Schrödinger equation is typically obtained from solutions of the electronic structure of atoms in solids, for which many schemes are available and are often provided together with LEED codes. In some cases, phase shifts must be pre-calculated, stored and input to the LEED code, while, in other cases, the phase shifts are calculated within the LEED code only when needed. In many cases the spherical atomic potential is obtained from a superposition of free atom potentials.

An essential point is here the choice of the muffin-tin radius. For clean metal surfaces with close packed lattices this works well; the muffin-tin radius is chosen as half of the nearest neighbour distance in the bulk. For ionic or covalent compounds the choice of the muffin-tin radii is less obvious: choosing half of the inter-atomic distance in the elemental or compound bulk structures as the muffin-tin radius leads to large discontinuities of the individual potentials to the interstitial muffin-tin constant; with covalent bonds this generates a large interstitial volume which is poorly described by a constant potential and thus uniform electron density. Such potential discontinuities do not appear explicitly in the LEED multiple scattering formalism; nevertheless, the choice of the muffin-tin radius does affect the calculated LEED intensities, in particular in the lower energy range below about 50–80 eV.

Until recently, the muffin-tin model was restricted to non-overlapping spheres. It has been shown that the use of overlapping spheres leads to the same secular equations as non-overlapping spheres and the same formalism can be used with overlapping spheres provided that the muffin-tin radii do not exceed the centres of the neighbouring potentials [5.4]. The use of overlapping spheres allows minimising the potential steps between the muffin-tin spheres. This method has been developed by J. Rundgren [5.5] and applied to calculating phase shifts for surface structures where the differing environment of each atom in the surface slab can be taken into account. This method led in a number of cases to a substantial improvement of the LEED analysis compared to separately calculated phase shifts from distinct elemental bulk structures.

For a more realistic non-spherical atomic potential (often called a full potential), the matrix \mathbf{t} becomes non-diagonal: all its elements can be non-zero, making their computation and the calculation of multiple scattering more complex. Some attempts have been made to include full potentials in the multiple scattering formalism [5.6–5.9], but no LEED code currently in use for structure determination includes such full potentials, to our knowledge.

Thermal atomic vibrations are normally and conveniently treated through ‘temperature-dependent’ phase shifts of the individual atoms, based on the Debye–Waller formalism of X-ray diffraction. This assumes isotropic and uncorrelated vibrations, thus neglecting correlations of vibrations between neighbouring atoms, as are present in phonons. Thermal vibrations tend to decrease the intensity of diffracted beams, as they redirect intensity to a more diffuse background in all scattering directions. With

the Debye model of thermal vibrations, the intensity scattered by a crystal atom in the single-scattering (kinematic) limit is multiplied by the Debye–Waller factor:

$$e^{-2M} = e^{-\frac{3\hbar^2|\mathbf{s}|^2 T}{m_a k_B \Theta_D^2}}, \quad (5.6)$$

where \mathbf{s} is the momentum transfer, T the sample temperature, m_a the atomic mass of the surface atoms, k_B the Boltzmann constant and Θ_D the Debye temperature of the material. For the multiple-scattering (dynamical) case of LEED, one assumes that the scattering amplitude $f(\vartheta)$ of each atom is multiplied by the Debye–Waller factor to yield an effective scattering amplitude $e^{-M}f(\vartheta)$, expressed in terms of effective ‘temperature-dependent’ phase shifts, after which multiple scattering is calculated as in the case of no thermal effect. This temperature-dependent scattering amplitude can be simply obtained by replacing the previously discussed phase shifts δ_l by the following modified temperature-dependent phase shifts (with m_e the electron mass):

$$\delta_l(T) = \frac{1}{2i} \ln \left[1 - \frac{4kim_e}{\hbar^2} t_l(T) \right]. \quad (5.7)$$

This approximation is widely used: it assumes isotropic thermal motion while correlation effects are ignored; the thermal motion of each atom is assumed to be independent from its neighbours. A more detailed discussion of thermal effects is given in Section 5.5.

5.2.2 Multiple Scattering: Plane Waves and Spherical Waves

To efficiently treat the multiple scattering of electrons by an assembly of atoms, we will select simple wave types to represent the full LEED wave function. Specifically, as discussed in Section 5.2, we will express the full electron wave function as a linear combination of either plane waves or ‘spherical’ waves (more accurately, if less evocatively, called ‘partial’ waves). The plane waves are a natural choice for a well-collimated incident beam and well-collimated diffracted beams due to a 2-D periodic surface and because the muffin-tin model contains regions of constant potential. The spherical waves are convenient in view of the assumed spherical shape of the atomic scattering potentials. Using spherical waves centred on each atom is called a ‘multi-centre expansion’.

An alternative approach is the ‘one-centre expansion’, in which all spherical waves are centred on the same point (not necessarily an atomic nucleus): its main disadvantage is the need for larger angular momenta l , roughly proportional to the outer radius of the cluster of atoms that it describes, instead of the atomic radius in the multi-centre expansion: this increases the computational time considerably. Hence the one-centre expansion is rarely used in LEED.

Most LEED theories use both plane waves and spherical waves in different parts of the calculations: as mentioned, plane waves are often used outside and between slabs of atoms, while spherical waves are often used within slabs of atoms, as well as within

clusters of atoms; this mixed approach is sometimes called ‘combined space method’. Spherical waves are thus also convenient within nanoparticles.

The spherical waves can be limited in number by the size of the phase shifts: as mentioned, this number is often truncated at $l = l_{\max} \sim 5$ to 10 for common LEED energies. For each value of the angular quantum number l , there are $2l + 1$ allowed values of the magnetic quantum number m . This results in a total of $(l_{\max} + 1)^2$ partial waves for a given value of l_{\max} .

The plane waves are given by the 2-D reciprocal lattice of a periodic surface: $\mathbf{k}_g^\pm = \mathbf{k}_0^\pm + \mathbf{g} = (k_{0x} + g_x, k_{0y} + g_y, \pm k_z)$, where $\mathbf{g} = 2\pi(h\mathbf{a}^* + k\mathbf{b}^*)$. Here we have added signs \pm to represent two sets of plane waves: those moving into a surface (+) and those moving out of a surface (−). The number of plane waves used is limited by the fact that for large $|g_x|$ or $|g_y|$ the waves become strongly evanescent on both sides of an atomic layer and therefore do not carry electrons from one atomic layer to another.

5.2.3 Multiple Scattering in a Cluster of Atoms

The scattering of electrons by an assembly of atoms can, in principle, be solved self-consistently and relatively efficiently through a multiple-scattering approach. Multiple scattering means that we allow an initially simple electron wave to scatter from individual atoms as many times as needed; normally, each subsequent scattering contributes a decreasing correction to the resulting total wave. Self-consistency is obtained when the multiple scattering converges.

However, scattering in LEED can be strong, depending on the atoms, scattering angles and electron energies involved and can prevent such convergence. In that case, it is still often possible to obtain a self-consistent solution, at a higher computational cost, with a closed formula. Typically, multiple scattering can be written as an infinite series of terms corresponding to increasing numbers of scatterings (e.g., a non-scattered term plus a single-scattering term plus a double-scattering term plus a triple-scattering term, etc.), as symbolically illustrated with the series $1 + x + x^2 + x^3 \dots$. This series can usually be summed into a closed formula, here $(1 - x)^{-1}$, which normally involves an inversion: since the mathematical quantities, like x here, involved in LEED are matrices, we perform matrix inversion in closed form. The computational expense of matrix inversion is often much larger than for a convergent series expansion, but it gives an exact and self-consistent solution of the multiple scattering problem. More effective and common than full matrix inversion is the method of Gaussian elimination and back substitution, which is also exact and self-consistent.

Much work has identified other efficient convergent multiple-scattering LEED schemes. We here describe the dominant approach, which is based on the Korringa–Kohn–Rostoker (KKR) methodology. It uses the atom scattering matrix \mathbf{t} and propagates spherical waves $h_l^{(1)}(kr)Y_{lm}(\vartheta, \varphi)$ through regions of constant potential between atoms, in accordance with the muffin-tin model.

We start by describing the multiple scattering between a pair of atoms: this will then be extended to multiple scattering within a cluster of N atoms, before considering

one periodic plane of atoms, several periodic planes of atoms, and ultimately an infinitely deep surface of atoms.

In this process, we in effect propagate simple spherical waves all the way from one atom *nucleus* to another, while the scattering itself is completely contained in the *t*-matrix: it is as if we had point scatterers representing dimensionless atoms but having the scattering properties of real extended atoms. As a result, the argument r in $h_l^{(1)}(kr)Y_{lm}(\vartheta, \varphi)$ will be taken as the distance between two atomic nuclei.

Suppose that a wave has been scattered from one atom in a pair of atoms: leaving that first atom is a wave that can be expressed as a linear combination of spherical waves. To include the effect of a subsequent scattering by the other atom, we must then express how a spherical wave of given angular momentum $L' = (l', m')$ centred on the first atom at \mathbf{r}_1 propagates to the second one, and how it decomposes into spherical waves centred and incident on that second atom at \mathbf{r}_2 . The result is given by a Green's function, which, for a constant potential between the atoms, takes the following form:

$$\bar{G}_{LL'}^{21} = -4\pi i \frac{2m_e}{\hbar^2} k \sum_{L_1} i^{l_1'} a(L, L', L_1) h_{l_1}^{(1)}(k|\mathbf{r}_2 - \mathbf{r}_1|) Y_{L_1}(\mathbf{r}_2 - \mathbf{r}_1). \quad (5.8)$$

Here, $k = |\mathbf{k}_g^\pm|$, while $L_1 = (l_1, m_1)$ runs over all values of l_1 and m_1 compatible with $L = (l, m)$ and $L' = (l', m')$, namely $|l - l'| \leq l_1 \leq l + l'$ and $m + m' = m_1$ (this summation will be assumed implicitly throughout this book, unless otherwise stated). This compatibility corresponds to non-zero values of the Clebsch–Gordan (or Gaunt) coefficients

$$a(L, L', L_1) = \int Y_L^*(\Omega) Y_{L'}(\Omega) Y_{L_1}^*(\Omega) d\Omega, \quad (5.9)$$

where Ω ranges over all values of solid angle.

Equation (5.8) gives the amplitude of the spherical wave $L = (l, m)$ centred on and arriving at the second atom at \mathbf{r}_2 due to a spherical wave $L' = (l', m')$ centred on and leaving the first atom at \mathbf{r}_1 . The Hankel function $h_{l_1}^{(1)}$ and the spherical harmonic Y_{L_1} describe the propagation, while the Clebsch–Gordan coefficients are due to the expansion of a spherical wave centred on one atom into spherical waves centred on the second atom.

We now have the tools to express an arbitrary scattering path involving the given pair of atoms 1 and 2. Consider the path drawn in Figure 5.4: the matrix expression $\mathbf{t}^2 \bar{\mathbf{G}}^{21} \mathbf{t}^1 \bar{\mathbf{G}}^{12} \mathbf{t}^2 \bar{\mathbf{G}}^{21} \mathbf{t}^1$ should be read, from right to left, as first a scattering \mathbf{t}^1 at atom 1 (labelled by the superscript 1), followed by propagation $\bar{\mathbf{G}}^{21}$ from atom 1 to atom 2 (superscripts '21'), then a scattering \mathbf{t}^2 at atom 2, followed by propagation $\bar{\mathbf{G}}^{12}$ back to atom 1, scattering there again and finally propagating again with $\bar{\mathbf{G}}^{21}$ to atom 2 for a final scattering \mathbf{t}^2 there. This particular multiple-scattering path involves four scatterings and three inter-atomic propagations. It can be extended to arbitrary length. The matrix notation implies summation over intermediate spherical waves of all possible angular momenta $L = (l, m)$.

Multiple scattering by two atoms

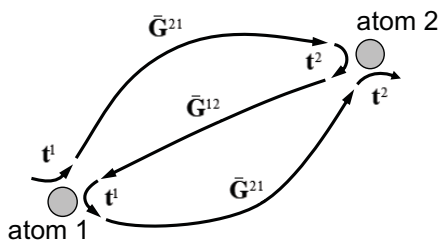


Figure 5.4 A multiple scattering path for a pair of atoms, showing nomenclature

We can now express and sum up all possible scattering paths, of any length, within the pair of atoms 1 and 2. We classify these paths according to the terminal atom, that is, whether each path ends at atom 1 or at atom 2, resulting in two series \mathbf{T}^1 and \mathbf{T}^2 , respectively:

$$\mathbf{T}^1 = \mathbf{t}^1 + \mathbf{t}^1 \bar{\mathbf{G}}^{12} \mathbf{t}^2 + \mathbf{t}^1 \bar{\mathbf{G}}^{12} \mathbf{t}^2 \bar{\mathbf{G}}^{21} \mathbf{t}^1 + \mathbf{t}^1 \bar{\mathbf{G}}^{12} \mathbf{t}^2 \bar{\mathbf{G}}^{21} \mathbf{t}^1 \bar{\mathbf{G}}^{12} \mathbf{t}^2 + \dots, \quad (5.10)$$

$$\mathbf{T}^2 = \mathbf{t}^2 + \mathbf{t}^2 \bar{\mathbf{G}}^{21} \mathbf{t}^1 + \mathbf{t}^2 \bar{\mathbf{G}}^{21} \mathbf{t}^1 \bar{\mathbf{G}}^{12} \mathbf{t}^2 + \mathbf{t}^2 \bar{\mathbf{G}}^{21} \mathbf{t}^1 \bar{\mathbf{G}}^{12} \mathbf{t}^2 \bar{\mathbf{G}}^{21} \mathbf{t}^1 + \dots. \quad (5.11)$$

In these two infinite series, we first have the single scattering from atom 1 (\mathbf{t}^1) or atom 2 (\mathbf{t}^2), respectively. Next comes the double-scattering term, followed by triple scattering and then quadruple scattering, etc. All paths in Eq. (5.10) end at atom 1, while all paths in Eq. (5.11) end at atom 2. The meaning of \mathbf{T}^1 and \mathbf{T}^2 can be easily understood by neglecting all multiple scattering, such that $\mathbf{T}^1 = \mathbf{t}^1$ and $\mathbf{T}^2 = \mathbf{t}^2$: we obtain the scattering matrix of the single atoms individually; the full expressions for \mathbf{T}^1 and \mathbf{T}^2 simply add to that all the multiple-scattering paths between the two atoms.

The two series Eqs. (5.10) and (5.11) can be solved self-consistently in closed form, once we specify the proper phases of the incident wave. If the incident wave is $e^{i\mathbf{k}_{\text{in}}\mathbf{r}}$, there is an amplitude ratio of $e^{i\mathbf{k}_{\text{in}}(\mathbf{r}_1 - \mathbf{r}_2)}$ between the amplitudes of this wave arriving from the outside at atoms 1 and 2. We shall insert this phase factor within the definition of $\bar{\mathbf{G}}^{21}$, which now becomes

$$\bar{G}_{LL'}^{21} = -4\pi i \frac{2m_e}{\hbar^2} k \sum_{L_1} i^{L_1} a(L, L', L_1) h_{L_1}^{(1)}(k|\mathbf{r}_2 - \mathbf{r}_1|) Y_{L_1}(\mathbf{r}_2 - \mathbf{r}_1) e^{i\mathbf{k}_{\text{in}}(\mathbf{r}_1 - \mathbf{r}_2)}. \quad (5.12)$$

The same expression with \mathbf{r}_1 and \mathbf{r}_2 exchanged gives $\bar{G}_{LL'}^{12}$. Inspection shows that Eqs. (5.10) and (5.11) are very closely linked, namely:

$$\mathbf{T}^1 = \mathbf{t}^1 + \mathbf{t}^1 \bar{\mathbf{G}}^{12} \mathbf{T}^2, \quad (5.13)$$

$$\mathbf{T}^2 = \mathbf{t}^2 + \mathbf{t}^2 \bar{\mathbf{G}}^{21} \mathbf{T}^1. \quad (5.14)$$

Now, Eqs. (5.13) and (5.14) constitute a self-consistent set of equations that can be solved in closed form for \mathbf{T}^1 and \mathbf{T}^2 . Using matrix notation, we get

$$\begin{pmatrix} \mathbf{T}^1 \\ \mathbf{T}^2 \end{pmatrix} = \begin{pmatrix} \mathbf{I} & -\mathbf{t}^1 \bar{\mathbf{G}}^{12} \\ -\mathbf{t}^2 \bar{\mathbf{G}}^{21} & \mathbf{I} \end{pmatrix}^{-1} \begin{pmatrix} \mathbf{t}^1 \\ \mathbf{t}^2 \end{pmatrix}, \quad (5.15)$$

where \mathbf{I} is a unit matrix and everything is known on the right-hand side. The dimension of the matrices \mathbf{I} , \mathbf{G} , \mathbf{t} , and \mathbf{T} is determined by the maximum number of phase shifts required to describe the atomic scattering: if $l \leq l_{\max}$, and all values of m such that $-l \leq m \leq l$ are included, then this dimension is $(l_{\max} + 1)^2$ (the larger matrix to be inverted will have double that dimension). We note that the geometrical series obtained by expanding the large-matrix inversion of Eq. (5.15) reproduces Eqs. (5.10) and (5.11), similar to $(1 - x)^{-1} = 1 + x + x^2 + \dots$. Equation (5.15) is rigorously valid even if Eqs. (5.10) and (5.11) do not converge well or do not converge at all, because Eqs. (5.13) and (5.14) are rigorous and do not depend on convergence of the series.

We can now generalise these results from a pair of atoms to a cluster of N atoms at positions \mathbf{r}_1 through \mathbf{r}_N . Equation (5.15) becomes

$$\begin{pmatrix} \mathbf{T}^1 \\ \mathbf{T}^2 \\ \mathbf{T}^3 \\ \vdots \\ \mathbf{T}^N \end{pmatrix} = \begin{pmatrix} \mathbf{I} & -\mathbf{t}^1 \bar{\mathbf{G}}^{12} & -\mathbf{t}^1 \bar{\mathbf{G}}^{13} & \dots & -\mathbf{t}^1 \bar{\mathbf{G}}^{1N} \\ -\mathbf{t}^2 \bar{\mathbf{G}}^{21} & \mathbf{I} & -\mathbf{t}^2 \bar{\mathbf{G}}^{23} & \dots & -\mathbf{t}^2 \bar{\mathbf{G}}^{2N} \\ -\mathbf{t}^3 \bar{\mathbf{G}}^{31} & -\mathbf{t}^3 \bar{\mathbf{G}}^{32} & \mathbf{I} & \dots & -\mathbf{t}^3 \bar{\mathbf{G}}^{3N} \\ \vdots & \vdots & \vdots & \ddots & \vdots \\ -\mathbf{t}^N \bar{\mathbf{G}}^{N1} & -\mathbf{t}^N \bar{\mathbf{G}}^{N2} & -\mathbf{t}^N \bar{\mathbf{G}}^{N3} & \dots & \mathbf{I} \end{pmatrix}^{-1} \begin{pmatrix} \mathbf{t}^1 \\ \mathbf{t}^2 \\ \mathbf{t}^3 \\ \vdots \\ \mathbf{t}^N \end{pmatrix}. \quad (5.16)$$

The matrix to be inverted now has dimension $N(l_{\max} + 1)^2$, proportional to the number of atoms in the cluster (again, computationally this matrix is actually not inverted: more efficient standard methods are available to solve this equation). Solving Eq. (5.16) produces the amplitudes \mathbf{T}^i of outgoing waves at each atom $i = 1, \dots, N$, due to the incident plane wave $e^{i\mathbf{k}_{\text{in}} \cdot \mathbf{r}}$. To obtain the amplitude of a total outgoing plane wave $e^{i\mathbf{k}_{\text{out}} \cdot \mathbf{r}}$, we must combine the waves leaving the different atoms with appropriate phases:

$$\mathbf{T} = \sum_{i=1}^N e^{i(\mathbf{k}_{\text{in}} - \mathbf{k}_{\text{out}}) \cdot \mathbf{r}_i} \mathbf{T}^i. \quad (5.17)$$

We next generalise this result to the case of a non-planar incident wave [5.10], such as a convergent spherical wave with an arbitrary angular profile; it will result in diffraction in all directions instead of diffraction into specific beams. We can represent a general incident wave as a continuous superposition of plane waves $\varphi(\mathbf{k}_{\text{in}}; \mathbf{r}) = (2\pi)^{-\frac{3}{2}} e^{i\mathbf{k}_{\text{in}} \cdot \mathbf{r}}$ with amplitudes $A(\mathbf{k}_{\text{in}})$, so that the total incident electron wave function can be written as an integral over all incident directions contained within a suitable solid angle Ω_{in} :

$$\Psi_{\text{in}}(\mathbf{r}) = \int_{\Omega_{\text{in}}} A(\mathbf{k}_{\text{in}}) \varphi(\mathbf{k}_{\text{in}}; \mathbf{r}) d\mathbf{k}_{\text{in}} = (2\pi)^{-\frac{3}{2}} \int_{\Omega_{\text{in}}} A(\mathbf{k}_{\text{in}}) \exp(i\mathbf{k}_{\text{in}} \cdot \mathbf{r}) d\mathbf{k}_{\text{in}}. \quad (5.18)$$

At a position \mathbf{R} far from the scattering cluster, the wave scattered by the cluster of N atoms at positions \mathbf{r}_i becomes:

$$\Psi_{\text{sc}}(\mathbf{R}) = -\sqrt{\frac{\pi}{2}} \frac{1}{k^2} \frac{e^{ikR}}{R} \sum_{i,L} e^{-ik\hat{\mathbf{R}}\mathbf{r}_i} Y_L'(\hat{\mathbf{R}}) X_L^i(k, \mathbf{r}_i, \Omega_{\text{in}}), \text{ with} \quad (5.19)$$

$$X_L^i(k, \mathbf{r}_i, \Omega_{\text{in}}) = \sum_{L'} \int_{\Omega_{\text{in}}} A(\mathbf{k}_{\text{in}}) e^{i\mathbf{k}_{\text{in}}\mathbf{r}_i} Y_{L'}^*(\hat{\mathbf{k}}_{\text{in}}) d\hat{\mathbf{k}}_{\text{in}} T_{LL'}^i, \quad (5.20)$$

using $T_{LL'}^i$ from Eq. (5.16) and the notation $\hat{\mathbf{v}}$ for the unit vector in the direction of any vector \mathbf{v} .

We can write Eq. (5.19) as $\Psi_{\text{sc}}(\mathbf{R}) = \frac{e^{ikR}}{R} f(\theta_{\text{sc}}, \varphi_{\text{sc}})$ to highlight the similarity with the atomic scattering factor $f(\theta_{\text{sc}})$, which has no azimuthal dependence. This results in the following differential cross-section into solid angle Ω_{sc} :

$$\frac{d\sigma}{d\Omega}(\Omega_{\text{sc}}) = (2\pi)^3 \frac{|f(\Omega_{\text{sc}})|^2}{\int_{\Omega_{\text{in}}} |A(\hat{\mathbf{k}}_{\text{in}})|^2 d\hat{\mathbf{k}}_{\text{in}}}. \quad (5.21)$$

For the special case of the collimated electron beam of normal LEED, with unique incident direction \mathbf{k}_{in} , we obtain:

$$\frac{d\sigma}{d\Omega}(\Omega_{\text{sc}}) = (2\pi)^3 |f(\Omega_{\text{sc}})|^2, \quad (5.22)$$

with the changed definition

$$X_L^i(k, \mathbf{r}_i, \Omega_{\text{in}}) \rightarrow X_L^i(k, \mathbf{r}_i, \mathbf{k}_{\text{in}}) = \sum_{L'} e^{i\mathbf{k}_{\text{in}}\mathbf{r}_i} Y_{L'}^*(\hat{\mathbf{k}}_{\text{in}}) T_{LL'}^i.$$

5.2.4 Multiple Scattering in Nanoparticles: NanoLEED

Nanoparticles contain at least tens to thousands of atoms. Their finite structure prevents the computational efficiencies provided by the 2-D periodicity of surfaces.

Equation (5.16) solves self-consistently the multiple scattering in a cluster of N atoms through a matrix inversion (or a related method such as Gaussian elimination/back substitution). Due to its matrix dimension $D = N(l_{\text{max}} + 1)^2$, and the fact that the computational cost of matrix inversion scales with the cube (or the square for some iterative schemes) of the cluster size, the cost rapidly becomes unaffordable. A modest cluster of 10 atoms and an average value of $l_{\text{max}} = 6$ already gives a matrix dimension of $D = 490$. For nanoparticles of hundreds or thousands of atoms, this approach is prohibitive. Even the series expansion, as in Eqs. (5.10) and (5.11), quickly becomes very demanding.

For that reason, more efficient approximate methods have been adapted for larger clusters, under the common name NanoLEED [5.10–5.13], namely: the sparse matrix canonical grid (SMCG) method and the UV method, described in more detail in

Sections 5.2.4.1–5.2.4.4. Their common feature is to more efficiently calculate $\mathbf{x} = \mathbf{A}^{-1}\mathbf{b}$, as in Eq. (5.16), which is the solution of the matrix-vector equation $\mathbf{Ax} = \mathbf{b}$. These two methods scale computationally as $D\log D$, instead of the cube of the matrix dimension D . These methods have distinct capabilities and are best used in parallel with each other in a single code, to solve each part of the multiple-scattering problem with the most effective method.

The SMCG and UV methods are not limited to nanoparticles: they can be applied equally well in complex periodic surface layers, for example, for a surface with a large bulk unit cell or large surface-unit-cell reconstruction, or in an overlayer of complex molecules such as C_{60} . Disordered surfaces can also be handled by NanoLEED [5.10], since the method does not require periodicity. The NanoLEED approach can also be combined with tensor LEED (TLEED) and other approximations to enable automated structural optimisation, cf. Section 5.4 [5.13].

In addition, convergent beams (such as the incident convergent wave shown in Eq. (5.18)) can also be accommodated, in addition to the traditional collimated beams of LEED. This allows studying individual nanostructures or nanoscale areas of a surface, since a convergent electron beam can sample just the small structure of interest, as proposed under the name convergent-beam LEED [5.14]; it may even be possible to focus a beam down to the nanoscale [5.15]. This enables the use of highly focused low-energy electron microscopy (LEEM), for example [5.16; 5.17]. Another experimental method to expose a small surface area uses a nearby STM tip to create a narrow beam of electrons aimed at a surface [5.18]. Such a tip-emitted beam expands to some extent with an angular spread of perhaps 5° , so it is only approximately collimated. While probe diameters of the order of $40\text{ }\mu\text{m}$ have already been achieved experimentally by this method, the potential exists of exposing regions smaller than about 40 nm , close to the size of many nanostructures.

5.2.4.1 The Sparse-Matrix Canonical Grid Method

In the sparse-matrix canonical grid (SMCG) method [5.12; 5.19], the scaling of the computational cost is improved by the fast Fourier transform (FFT). This is made possible by changing matrix \mathbf{A} to be strictly periodic (as for a periodic structure), that is, $A_{n,m} = A_{n-m}$, even though the nanoparticle structure may not be periodic at all. (The matrix A is called a Toeplitz matrix, and contains only $2D - 1$ independent elements, instead of D^2). The major step of the inversion of such a matrix can be performed by fast Fourier transform (FFT), which scales as $D\log D$. However, the use of FFT imposes a constraint on D , which must be an integer power of 2.

For LEED, this method would require that the atoms occupy a periodic, rectangular spatial grid. However, with an arbitrary non-periodic structure, including any nanostructure, we can construct a regular grid of points and refer each atom to its nearest grid point, as illustrated in Figure 5.5; then the propagation of an electron from an atom i to an atom j proceeds via the grid points P and Q nearest to atoms i and j , respectively, that is, along the path $i \rightarrow P \rightarrow Q \rightarrow j$.

This SMCG method is exact if a sufficient number of partial waves $(l_{\text{max}} + 1)^2$ is used, so as to enable the accurate propagation of electrons between each atom and its

Sparse-Matrix Canonical Grid (SMCG) method

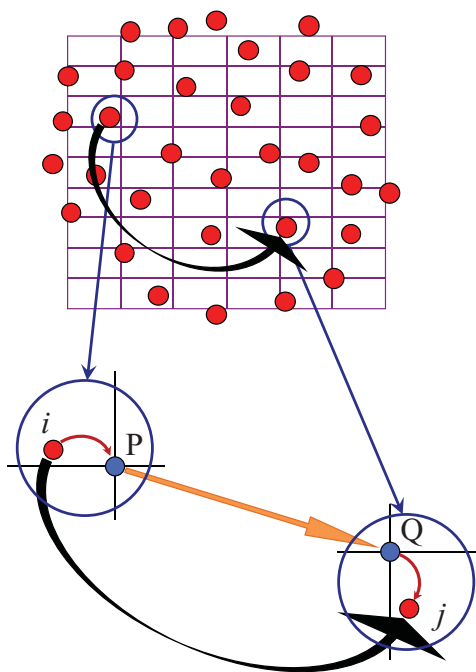


Figure 5.5 Principle of the sparse-matrix canonical grid (SMCG) method. The scattering path from any atom i to any atom j is made to pass through their nearest grid points P and Q , respectively, of a periodic grid overlain on the nanoparticle. The bottom panel zooms in on points i and j . Figure redrawn with permission from [5.12] G. M. Gavaza, Z. X. Yu, L. Tsang, C. H. Chan, S. Y. Tong and M. A. Van Hove, *Phys. Rev. B*, vol. 75, p. 014114, 2007. <http://dx.doi.org/10.1103/PhysRevB.75.014114>. © (2007) by the American Physical Society.

nearest grid point; this number of partial waves increases with the distance between atom and grid point (because l_{\max} should be roughly proportional to that distance) and is reduced by using a denser grid. The major part of the computation, however, turns out to be the scattering between the regular grid points, which is solved with FFT in times proportional to $N_g \log N_g$, where N_g is the number of grid points used (in each dimension, FFT requires a number of grid points that is a power of 2): the number N_g is approximately related to the number of atoms. Thus, a compromise is needed between grid density (which reduces the distance between atoms and grid points and thus l_{\max}) and the total number of grid points (which affects the cost of FFT).

5.2.4.2 The UV Method

An alternative method to SMCG uses singular value decomposition (SVD) [5.12; 5.20]. If the rank of matrix \mathbf{A} (i.e., the number of its non-zero eigenvalues) is $r < D$, where D

is the matrix dimension, \mathbf{A} can be factored into a product of three matrices, $\mathbf{A}_{D \times D} = \mathbf{U}_{D \times r} \mathbf{R}_{r \times r} \mathbf{V}_{r \times D}$ (the subscripts here indicate the matrix dimensions), where the smaller matrix \mathbf{R} is diagonal with dimension r and contains the r non-zero eigenvalues of \mathbf{A} , while \mathbf{U} and \mathbf{V} are rectangular. LEED does not produce vanishing eigenvalues, but this approach can still be used approximately by equating small eigenvalues to zero: we can then replace \mathbf{A} by \mathbf{URV} . Thereby, the smaller is the rank r , the faster is the computation. To efficiently find the rank and the singular values of a matrix, the so-called UV method can be used for the SVD decomposition. This approach also leads to computation times proportional to $D \log D$.

The UV method is an approximation exploiting prior knowledge of or prediction for the value of the rank r . If one can predict or estimate a certain value r_e for the rank of the matrix \mathbf{A} , then the decomposition can be performed using not the entire matrix \mathbf{A} , but only linearly independent rows and columns *sampled* from the matrix \mathbf{A} . This way, the decomposition complexity is lowered to Dr_e^2 and so its computational weight is drastically reduced, since the bulk of the calculation is spent on the matrix-vector multiplication.

‘Sampling’ is done with an algorithm that can select from the rows and columns of the matrix \mathbf{A} a set of r_e linearly independent rows and r_e linearly independent columns. To ensure the accuracy of the method, one must overestimate the rank r of \mathbf{A} when predicting the value of r_e ($r_e > r$) and, in order to ensure a high method efficiency, the difference between estimated and real rank should be as low as possible ($r_e \cong r$). This is achieved in practice by using empirical values obtained from prior studies on the system of interest. The resulting accuracy depends on the choice of the sampled rows and columns. In LEED practice a rank of ~ 15 is found to be adequate for neighbouring atoms, declining rapidly to ~ 3 for atoms distant by 1.5 nm (15 Å) or more.

Figure 5.6 illustrates the application of the SMCG and UV methods to an ordered (4×4) layer of C_{60} molecules on a Cu(111) surface [5.12]: they are visually almost indistinguishable from an exact calculation performed with the conjugate gradient (CG) method, which is an iterative method that scales as D^2 and converges to the result of exact matrix inversion. In the combined SMCG+UV+CG method, the relative compute times at 100 eV were in the proportions SMCG : UV : CG $\sim 100 : 16.1 : 4.4$, while the scaling was confirmed to be very close to $D \log D$.

5.2.4.3 NanoLEED for Nanoparticles

The SCMG and UV methods are most efficient in different circumstances. SMCG outperforms UV for large numbers of atoms and large inter-atomic distances. Also, the more conventional CG method is more efficient than either SMCG or UV for small numbers of atoms and small inter-atomic distances [5.12]. It is therefore useful to combine these three methods into a single ‘NanoLEED’ code which selects the most efficient approach at each stage: a single structure often includes near, intermediate and distant neighbours, so different methods are applied to different pairs of atoms in the same structure.

Figure 5.7 illustrates the application of NanoLEED to nanowires of different sizes. The LEED pattern becomes diffuse due to the finite size of the nanoparticles, such that

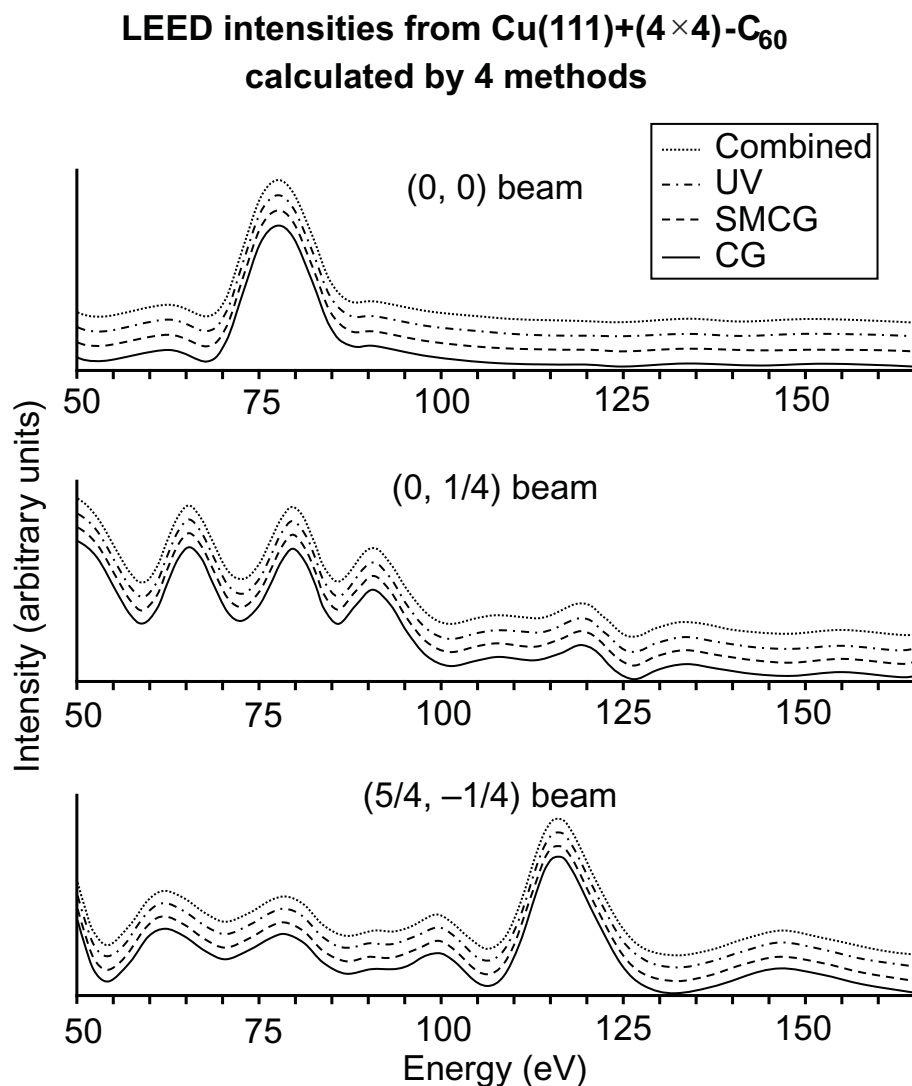
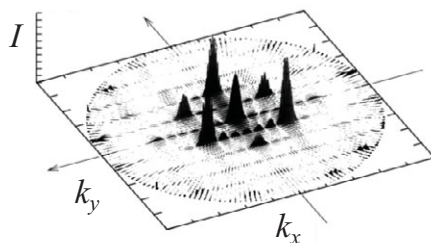
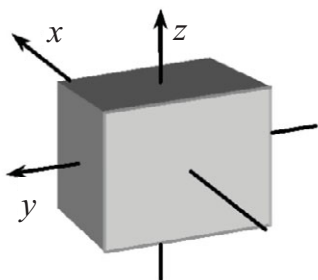


Figure 5.6 LEED intensities calculated for three beams diffracted from Cu(111)+(4×4)-C₆₀ by the conjugate gradient method (CG), the sparse-matrix canonical grid method (SMCG), the UV method and their combined use (the latter approach is described in Section 5.2.4.3). Figure redrawn with permission from [5.12] G. M. Gavaza, Z. X. Yu, L. Tsang, C. H. Chan, S. Y. Tong, and M. A. Van Hove, *Phys. Rev. B*, vol. 75, p. 014114, 2007. <http://dx.doi.org/10.1103/PhysRevB.75.014114>. © (2007) by the American Physical Society.

the inherent periodicity of the upper surface (exposed to a collimated LEED beam) produces a pattern of broadened spots that correspond directly to the conventional sharp LEED spot pattern of the infinite surface.

Figure 5.8 illustrates the structural sensitivity of LEED intensities from a single surface layer of nanowires. It was found that ‘circular’ detector scans around the

(a) Short & thick Si nanowire



(b) Long & thin Si nanowire

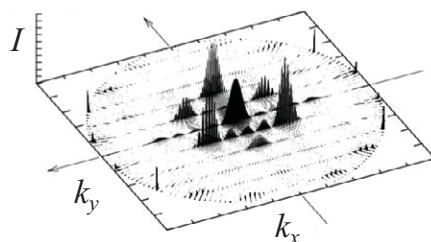
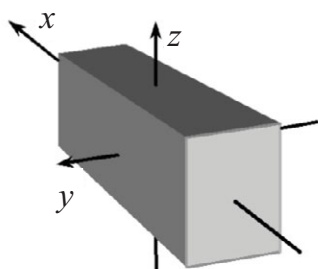


Figure 5.7 LEED patterns calculated by NanoLEED for Si nanowires of two different lateral sizes sketched on the left: (a) $(x, y, z) = (4.9, 1.2, 0.7)$ nm and (b) $(x, y, z) = (10.2, 0.8, 0.7)$ nm. The z -axis corresponds to the surface normal in usual LEED experiments from surfaces; the upper z -face exposes an ideal bulk-like Si(111) surface; normal incidence of a collimated LEED beam directed toward $-z$ is assumed. The $\langle 1, 1, -2 \rangle$ Si crystallographic direction points along x . The LEED patterns (on the right) show bulk-induced maxima in directions implied by the Si (111) surface structure; these maxima are broadened in inverse proportion to the different x - and y -dimensions of the nanoparticles. For clarity, the plots only show intensities along radial lines of the patterns, causing artificial fine structure. Figure redrawn with permission from [5.10] G. M. Gavaza, Z. X. Yu, L. Tsang, C. H. Chan, S. Y. Tong, and M. A. Van Hove, *Phys. Rev. B*, vol. 75, p. 235403, 2007. <http://dx.doi.org/10.1103/PhysRevB.75.235403>. © (2007) by the American Physical Society.

nanowire axis show sensitivity to even minor structural changes. In this example of a silicon nanowire, the upper Si surface monolayer (saturated with hydrogen which can produce an outward expansion of the outermost layer spacing) is allowed to ‘warp’, being more expanded near the centre than near the ends of the nanowire, by a difference of only 0.004 nm (0.04 Å). The effect on LEED intensities of such small structural changes can be appreciable under suitable diffraction geometries.

5.2.4.4 NanoLEED with Matrix Inversion in Subclusters

One finds that strong multiple scattering may occasionally cause poor convergence in NanoLEED (e.g., within a SiH_3 group, surprisingly, meaning that strong multiple

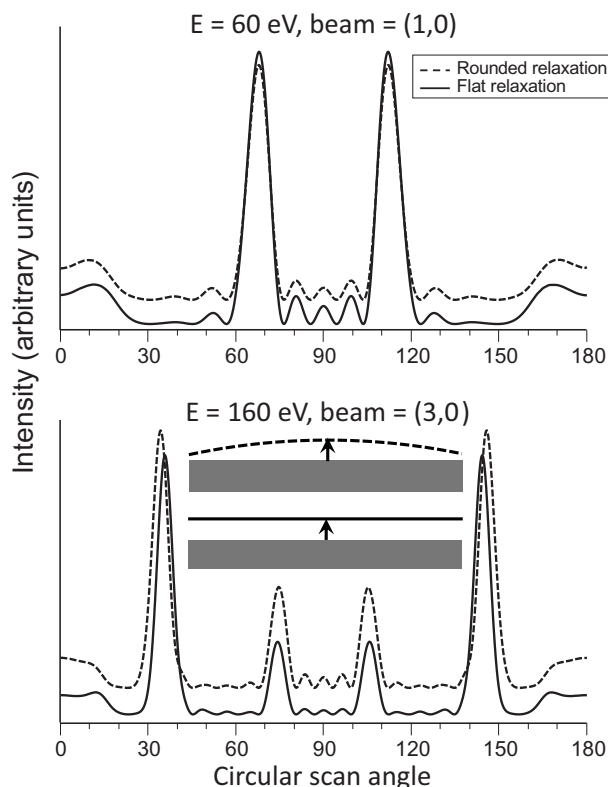


Figure 5.8 Effect on calculated LEED intensities of ‘rounding’ the relaxation of the topmost SiH_3 layer of a silicon nanowire of dimensions $10.2 \times 1.8 \times 0.7$ nm exposing a H-saturated Si (111) surface to the incident collimated beam: the nanowire is shown as two insets at the bottom, with length to left and right, and with height up and down; the lower inset shows a uniform outward relaxation of the outer monolayer (full line); the upper inset shows a rounded expansion. The rounding consists in expanding the outer Si monolayer (decorated with H_3) more at the centre and less at the ends of the nanowire (cf. lower nanowire with curved outer monolayer shown as dashed line): the centre of the monolayer is expanded outward from the bulk by 0.012 nm (0.12 Å), while the far ends of the monolayer are only expanded outward by 0.008 nm (0.08 Å): the difference of 0.004 nm (0.04 Å) induces noticeable changes of the relative peak heights or shifts of the major peaks in azimuthal direction. Shown are ‘circular’ scans halfway around the long axis of the nanowire, with 90° being along the vertical axis of the nanowires and marking specular reflection from the top (relaxed) facet of the nanowire. Figure redrawn with permission from [5.10] G. M. Gavaza, Z. X. Yu, L. Tsang, C. H. Chan, S. Y. Tong, and M. A. Van Hove, *Phys. Rev. B*, vol. 75, p. 235403, 2007. <http://dx.doi.org/10.1103/PhysRevB.75.235403>. © (2007) by the American Physical Society.

scattering can build up between the Si and H atoms). To overcome this limitation, such problematic small subclusters of atoms can be treated with complete matrix inversion to guarantee full and accurate inclusion of multiple scattering within them: the result is a (non-diagonal) scattering matrix describing the exact and complete scattering by that subcluster, which can then be included as a non-spherical

‘pseudo-atom’ in the NanoLEED method [5.13]. This approach uses the idea of one-centre expansion applied earlier by D. K. Saldin and J. B. Pendry to LEED [5.21] and follows the cluster approach to LEED developed in the 1980s [5.22].

5.2.5 Multiple Scattering in Atomic Layers

5.2.5.1 A Periodic Plane of Atoms

We here return to 2-D periodic arrays of atoms present in a surface. In Eq. (5.16), the dimension of the central matrix to be inverted is $N(l_{\max} + 1)^2$, which rapidly becomes prohibitive for clusters with many atoms N . For a periodic layer of atoms, however, as in a surface, we can exploit the periodicity very effectively. With a Bravais lattice (i.e., a single atom in each unit cell), all atoms are equivalent, so that the total wave leaving each atom is the same (apart from a simple phase factor as in Eq. (5.17) and further explained in Sections 5.2.5.2 and 5.2.5.4):

$$\mathbf{T}^1 = \mathbf{T}^2 = \dots = \mathbf{T}^N \equiv \boldsymbol{\tau}.$$

We shall henceforth reserve the symbol $\boldsymbol{\tau}$ for the scattering by a Bravais lattice plane of atoms. In analogy with Eqs. (5.13) and (5.14), we can now write:

$$\boldsymbol{\tau} = \mathbf{t} + \mathbf{t} \left(\sum_n' \overline{\mathbf{G}}^{in} \right) \boldsymbol{\tau}, \quad (5.23)$$

where n extends over all atoms other than the atom i under consideration (the exclusion of atom i is indicated by the prime on the summation symbol). The index i can be dropped from the result since the outcome is the same for all atoms i . We define the new ‘planar’ Green’s function

$$G_{LL'}^{ii} = \sum_n' \overline{G}_{LL'}^{in} = -4\pi i \frac{2m_e}{\hbar^2} k \sum_{L_1} \sum_{\mathbf{P}} t^{i1} a(L, L', L_1) h_{L_1}^{(1)}(k|\mathbf{P}|) Y_{L_1}(\mathbf{P}) e^{-i\mathbf{k}_{in}\mathbf{P}}, \quad (5.24)$$

which includes a sum over all atoms at positions \mathbf{P} , except at the origin $\mathbf{P} = \mathbf{0}$. (This exclusion is again denoted by the prime on the summation symbol.) The superscripts of $G_{LL'}^{ii}$ have become meaningless since the right-hand side of Eq. (5.24) no longer depends on the atom index i , but we shall retain them for later generalisation. Now, Eq. (5.24) implies that

$$\boldsymbol{\tau} = (1 - \mathbf{t}\mathbf{G}^{ii})^{-1} \mathbf{t} = \mathbf{t}(1 - \mathbf{G}^{ii}\mathbf{t})^{-1}. \quad (5.25)$$

Equation (5.25) essentially solves the multiple scattering in a Bravais-lattice plane. Although it contains an infinite number of atoms, the matrices have a relatively small dimension, namely $(l_{\max} + 1)^2$, and we have a self-consistent solution valid whatever the amount of multiple scattering may be. We are still employing the spherical-wave representation, and, consequently, $\boldsymbol{\tau}$ has matrix elements $\tau_{LL'}$. The quantity $\tau_{LL'}$ indicates that an incident spherical wave L' of amplitude 1 centred on any of the

atoms of the layer eventually produces an amplitude $\tau_{LL'}$ in a departing spherical wave L centred on the same atom.

The lattice sum in Eq. (5.24) is expected to converge only if sufficient damping is present in the form of the imaginary part of k in the Hankel function $h^{(1)}$. Thus, when inelastic effects are weak, such as at kinetic energies near or below the Fermi level, a different summation procedure is required. K. Kambe has formulated an alternative method based on an Ewald summation scheme [5.23–5.25]. Basically, it consists of a Fourier summation over the distant part of the atomic lattice and a direct summation over the near part of the atomic lattice. Even for normal LEED cases where the kinetic energy is far above the Fermi level, the Kambe approach is computationally slightly faster than the direct-space summation of Eq. (5.24), but at the expense of more complicated programming.

5.2.5.2 Several Periodic Planes of Atoms

Just as we assembled several atoms into clusters, we can stack several periodic layers into a thicker slab of atoms: this slab can represent a surface of finite thickness. If there is enough damping, this may even suffice to represent an infinitely thick surface: this case is often called the ‘giant-matrix method’. There are also more effective ways to create an infinitely thick surface by stacking individual layers and/or slabs, as we will discuss in Section 5.2.6.

Following a derivation that is parallel to the case of assembling individual atoms, we can stack N individual periodic atomic layers, each having the same Bravais lattice with an atom at location \mathbf{r}_i , $i = 1, \dots, N$. In very close analogy with Eq. (5.16) we obtain

$$\begin{pmatrix} \mathbf{T}^1 \\ \mathbf{T}^2 \\ \mathbf{T}^3 \\ \vdots \\ \mathbf{T}^N \end{pmatrix} = \begin{pmatrix} \mathbf{I} & -\boldsymbol{\tau}^1 \mathbf{G}^{12} & -\boldsymbol{\tau}^1 \mathbf{G}^{13} & \dots & -\boldsymbol{\tau}^1 \mathbf{G}^{1N} \\ -\boldsymbol{\tau}^2 \mathbf{G}^{21} & \mathbf{I} & -\boldsymbol{\tau}^2 \mathbf{G}^{23} & \dots & -\boldsymbol{\tau}^2 \mathbf{G}^{2N} \\ -\boldsymbol{\tau}^3 \mathbf{G}^{31} & -\boldsymbol{\tau}^3 \mathbf{G}^{32} & \mathbf{I} & \dots & -\boldsymbol{\tau}^3 \mathbf{G}^{3N} \\ \vdots & \vdots & \vdots & \ddots & \vdots \\ -\boldsymbol{\tau}^N \mathbf{G}^{N1} & -\boldsymbol{\tau}^N \mathbf{G}^{N2} & -\boldsymbol{\tau}^N \mathbf{G}^{N3} & \dots & \mathbf{I} \end{pmatrix}^{-1} \begin{pmatrix} \boldsymbol{\tau}^1 \\ \boldsymbol{\tau}^2 \\ \boldsymbol{\tau}^3 \\ \vdots \\ \boldsymbol{\tau}^N \end{pmatrix}. \quad (5.26)$$

Comparing Eq. (5.26) with Eq. (5.16), the single-atom matrix \mathbf{t} is replaced by the single-Bravais-plane matrix $\boldsymbol{\tau}$, while $\bar{\mathbf{G}}^{ij}$ is replaced by a similar \mathbf{G}^{ij} , where

$$G_{LL'}^{ij} = -4\pi i \frac{2m_e}{\hbar^2} k \sum_{L_1} \sum_{\mathbf{P}} i^{l_1} a(L, L', L_1) h_{l_1}^{(1)}(k|\mathbf{r}_j - \mathbf{r}_i + \mathbf{P}|) Y_{L_1}(\mathbf{r}_j - \mathbf{r}_i + \mathbf{P}) e^{-i\mathbf{k}_{\text{in}}(\mathbf{r}_j - \mathbf{r}_i + \mathbf{P})}. \quad (5.27)$$

Here, \mathbf{P} extends over the lattice points of any of the planes, except the point $\mathbf{r}_j - \mathbf{r}_i + \mathbf{P} = 0$. The amplitude of the total plane wave scattered from this stack of N layers can again be obtained from Eq. (5.17), by simply inserting there the result of Eq. (5.26).

5.2.5.3 Diffraction Matrices for a Bravais-Lattice Layer

A periodic surface scatters an incoming electron beam into a set of well-defined departing electron beams: to obtain the intensity of these outgoing beams, we first need a relation between an arbitrary general t -matrix $t_{LL'}$, giving the diffraction amplitude between two spherical waves L and L' , and a plane-wave diffraction amplitude $M_{\text{out},\text{in}}$ between two plane waves \mathbf{k}_{in} and \mathbf{k}_{out} . For a lattice with 2-D periodicity, such a relation is given by

$$M_{\text{out},\text{in}} = -\frac{8\pi^2 i}{A k_{\text{out}z}} \frac{2m_e}{\hbar^2} \sum_{LL'} Y_L(\mathbf{k}_{\text{out}}) t_{LL'} Y_{L'}^*(\mathbf{k}_{\text{in}}), \quad (5.28)$$

where A is the area of the 2-D unit cell ($1/A$ is the number density of atoms in each atomic plane). In particular, for the incident beam \mathbf{k}_0 and the outgoing beam \mathbf{k}_g^- , we obtain, by inserting Eq. (5.17) into Eq. (5.28), the reflected amplitude

$$M_{g,0}^- = -\frac{16\pi^2 i m_e}{A k_{gz}^- \hbar^2} \sum_{LL'} Y_L(\mathbf{k}_g^-) T_{LL'} Y_{L'}^*(\mathbf{k}_0), \quad (5.29)$$

where $T_{LL'}$ is calculated from the results of Eq. (5.26), via Eq. (5.17).

A surface will often be represented by a stack of layers (whether single Bravais-lattice planes or slabs of such planes). Each of these layers will diffract the plane waves according to the Laue conditions in 2-D. Therefore, starting with the incident beam \mathbf{k}_0 , all beams \mathbf{k}_g^\pm can be generated and each of these can be incident on another layer, from one side or the other (into the surface or outward from the surface). We therefore need the amplitude of any of the diffracted plane waves \mathbf{k}_g^\pm (where \mathbf{g}' is in general different from \mathbf{g}) due to such an incident wave.

For a layer containing only one atomic plane (we call it a Bravais-lattice layer), we get

$$M_{g'g}^{\pm\pm} = -\frac{16\pi^2 i m_e}{A k_{gz}^+ \hbar^2} \sum_{LL'} Y_L(\mathbf{k}_{g'}^\pm) \tau_{LL'} Y_{L'}^*(\mathbf{k}_g^\pm) + \delta_{g'g} \delta_{\pm\pm}. \quad (5.30)$$

The two Kronecker symbols (equal to unity when $\mathbf{g}' = \mathbf{g}$ and when the signs are the same, respectively) in this expression represent the unscattered plane wave of amplitude 1 which is transmitted without change of direction through the layer (the transmitted wave is modified by the wave which is scattered in the forward direction). Note the right-to-left logical order of the indices of $M_{g'g}^{\pm\pm}$.

The following form equivalent to Eq. (5.29) was derived by J. B. Pendry [5.1]:

$$M_{g'g}^{\pm\pm} = \frac{8\pi^2 i m_e}{A k_{gz}^+ \hbar^2} \sum_{lm'l'm'} \left[i^l (-1)^m Y_{l-m}(\mathbf{k}_g^\pm) \right] (1-X)^{-1}_{lm,l'm'} \left[i^{-l'} Y_{l'm'}(\mathbf{k}_{g'}^\pm) \right] \sin \delta_{l'} e^{i\delta_{l'}} + \delta_{g'g} \delta_{\pm\pm}, \quad (5.31)$$

with

$$X_{lm,l'm'} = \sum_{l'+m'=\text{even}} C^l(l'm', l'', m'') F_{l'm'} \sin \delta_{l'} e^{i\delta_{l'}}, \quad (5.32)$$

$$C^l(l'm', l'', m'') = 4\pi (-1)^{(l-l'-l'')/2} (-1)^{m'+m''} Y_{l'-m'}(\theta=\pi/2, \varphi=0) \int Y_{lm} Y_{l'm'} Y_{l''-m''} d\Omega, \quad (5.33)$$

$$F_{l'm'} = \sum_{\mathbf{P}} e^{i\mathbf{k}\mathbf{P}} h_l^{(1)}(k|\mathbf{P}|) (-1)^{m'} e^{-im'\varphi(\mathbf{P})}. \quad (5.34)$$

Here, $C^l(l'm', l'', m'')$ is a set of Clebsch–Gordan coefficients that is different from the set $a(lm, l'm', l_1 m_1)$ of Eq. (5.9). However, these two sets are equivalent under suitable permutations, apart from different prefactors. In Eq. (5.34), $\varphi(\mathbf{P})$ is the azimuth in the surface plane of the lattice vector $\mathbf{P} \neq \mathbf{0}$. (One minor discrepancy occasionally appears in some versions of these formulae: the complex wave number k in the denominator of Eq. (5.31) is sometimes replaced by its absolute value or by its real part.)

5.2.5.4 Diffraction Matrices for a Layer with N Periodic Atomic Planes

Equation (5.31) can be generalised to the case of a layer containing multiple periodic atomic planes, namely a composite layer, N :

$$M_{\mathbf{g}'\mathbf{g}}^{\pm\pm} = -\frac{16\pi^2 im_e}{Ak_{\mathbf{g}z}^+ \hbar^2} \sum_{LL'} Y_L(\mathbf{k}_{\mathbf{g}}^{\pm}) \sum_{i=1}^N \left\{ e^{i(\pm\mathbf{k}_{\mathbf{g}}^{\pm} \mp \mathbf{k}_{\mathbf{g}'}^{\pm})\mathbf{r}_i} T_{LL'}^i \right\} Y_{L'}^*(\mathbf{k}_{\mathbf{g}}^{\pm}) + \delta_{\mathbf{g}'\mathbf{g}} \delta_{\pm\pm}, \quad (5.35)$$

using $T_{LL'}^i$ from Eq. (5.26). One small modification is needed here in the Green's function of Eq. (5.27): the incident wave is now $\mathbf{k}_{\mathbf{g}}^{\pm}$ rather than \mathbf{k}_{in} . Simultaneously with the final form of $G_{LL'}^{ji}$, we now give an alternate form derived by S. Y. Tong [5.2], based on a reciprocal-lattice summation rather than a direct-lattice summation:

$$G_{LL'}^{ji} = e^{-i\mathbf{k}_{\mathbf{g}}^{\pm}(\mathbf{r}_j - \mathbf{r}_i)} \hat{G}_{LL'}^{ji}, \text{ with} \quad (5.36)$$

$$\hat{G}_{LL'}^{ji} = -\frac{8\pi i k m_e}{\hbar^2} \sum_{L_1} \sum_{\mathbf{P}} i^{L_1} a(L, L', L_1) h_{L_1}^{(1)}(k|\mathbf{r}_j - \mathbf{r}_i + \mathbf{P}|) Y_{L_1}(\mathbf{r}_j - \mathbf{r}_i + \mathbf{P}) e^{-i\mathbf{k}\mathbf{P}} \quad (5.37)$$

$$\text{or } \hat{G}_{LL'}^{ji} = -\frac{16\pi^2 im_e}{A\hbar^2} \sum_{\mathbf{g}_1} \frac{e^{i\mathbf{k}_{\mathbf{g}_1}^{\pm}(\mathbf{r}_j - \mathbf{r}_i)}}{k_{\mathbf{g}_1 z}^+} Y_L^*(\mathbf{k}_{\mathbf{g}_1}^{\pm}) Y_{L'}(\mathbf{k}_{\mathbf{g}_1}^{\pm}). \quad (5.38)$$

Equation (5.38) has computational advantages over Eq. (5.37) under certain circumstances, namely when the atomic planes of the layer are not spaced too closely: the sum over \mathbf{g}_1 in principle runs over the infinite 2-D reciprocal lattice, but is limited by the evanescent character of waves with large $|\mathbf{g}_1|$ for larger spacings between atomic planes.

We note that Eqs. (5.27) and (5.29) assume a reference point (origin of coordinates) at the centre of an atom in the layer under consideration: $M_{\mathbf{g}'\mathbf{g}}^{\pm\pm}$ is the ratio of outgoing

to incident plane-wave amplitudes measured in that atomic centre (or at least extrapolated to that atomic centre as if we had point scatterers). In Eq. (5.35) the corresponding reference point is the origin of the vectors \mathbf{r}_i and thus can be an arbitrary point. However, it is important to be consistent in the use of a particular reference point in each layer when carrying out a calculation, especially in connection with the utilisation of symmetries.

5.2.5.5 Layer Reflection and Transmission Matrices

We now introduce a notation that will be convenient when we treat the stacking of layers in a surface. We distinguish between reflection and transmission at a layer: transmission occurs when electrons emerge on the side of the layer opposite to that from which they impinge on it, while reflection occurs when they emerge on the same side, with an appropriate generalisation in the case of evanescent waves. This definition implies, for example, that grazing specular diffraction is treated as a reflection rather than as a transmission, even though the scattering angle may be close to 0° . Thus, we define reflection and transmission matrices

$$\mathbf{r}^{+-} = \mathbf{M}^{+-}, \quad \mathbf{r}^{++} = \mathbf{M}^{++}, \quad \mathbf{t}^{++} = \mathbf{M}^{++}, \quad \mathbf{t}^{--} = \mathbf{M}^{--}, \quad (5.39)$$

where \mathbf{M}^{++} comes from Eqs. (5.29), (5.30) or (5.35).

5.2.6 Layer Stacking

We have obtained the scattering properties of 2-D periodic atomic layers of finite thickness, whether of mono-atomic thickness or of multi-atomic thickness. These layers can next be stacked onto each other to form thicker slabs of layers, including a semi-infinite slab. We start with the latter, solving the complete semi-infinite surface in a closed and self-consistent form, using Bloch waves.

5.2.6.1 Bloch Wave and Transfer Matrix Methods

The Bloch wave method and its close relative, the transfer matrix method, together with the matrix-inversion method (Section 5.2.5), were the earliest solutions of the LEED problem. The Bloch wave and transfer matrix methods have the virtues of providing a connection with the familiar band structure theory of bulk materials and of giving a simple interpretation of the electron diffraction process at elementary surfaces. However, these advantages have not been particularly useful in treating more complex surfaces involving adsorbates or reconstructions.

In this approach, one applies the Bloch condition to the electronic wave functions in the direction perpendicular to the surface for the bulk layers that have a well-defined periodicity perpendicular to the surface. An eigenvalue problem then provides the Bloch functions, the relative amplitudes of which are determined by a matching across the surface to the plane waves in the vacuum.

At a point midway between layers i and $i + 1$ in the bulk (away from any structural and electronic deviations due to the surface), we decompose a Bloch wave into plane waves defined by the 2-D periodicity of the surface:

$$\varphi_i(\mathbf{r}) = \sum_{\mathbf{g}} \left(b_{i\mathbf{g}}^+ e^{i\mathbf{k}_{\mathbf{g}}^+ \cdot \mathbf{r}} + b_{i\mathbf{g}}^- e^{i\mathbf{k}_{\mathbf{g}}^- \cdot \mathbf{r}} \right). \quad (5.40)$$

We include both penetrating and emerging plane waves in this expansion: these plane waves are represented in Figure 5.9 as trios of arrows pointing to the right (into the surface) and to the left (toward the vacuum), respectively.

The Bloch condition, due to the periodicity perpendicular to the surface, implies that the relations

$$b_{i+1}^+ = b_i^+ e^{i\mathbf{k}_B \cdot \mathbf{a}} \quad (5.41)$$

and

$$b_{i+1}^- = b_i^- e^{i\mathbf{k}_B \cdot \mathbf{a}} \quad (5.42)$$

hold for each plane-wave amplitude of the Bloch wave of Eq. (5.40), if \mathbf{a} is the repeat vector that relates one layer to the next (\mathbf{a} need not be perpendicular to the surface). Here $e^{i\mathbf{k}_B \cdot \mathbf{a}}$ is an eigenvalue to be determined, which will then specify the value of the Bloch wave vector \mathbf{k}_B , familiar in band structures.

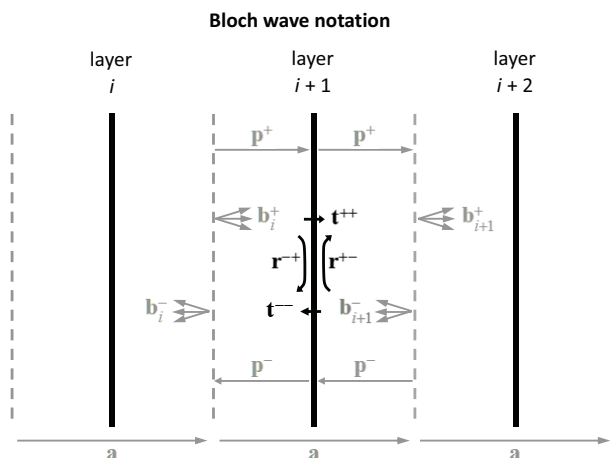


Figure 5.9 Bloch wave notation, where b_i^+ and b_i^- are plane-wave amplitudes of a Bloch wave travelling to the right between layers i and $i + 1$ of a periodic sequence of identical layers (see Eq. (5.40)). Three atomic layers are shown as thick black vertical lines. Each atomic plane has reflection and transmission matrices for plane waves given by \mathbf{r}^{+-} , \mathbf{r}^{-+} , \mathbf{t}^{++} , and \mathbf{t}^{--} , according to Eq. (5.39). Shown in grey are midway planes (dashed lines), the layer repetition vector \mathbf{a} and the plane-wave propagators \mathbf{p}^+ and \mathbf{p}^- for propagation by $+\mathbf{a}/2$ and $-\mathbf{a}/2$, respectively. Adapted with permission from Springer Nature Customer Service Centre GmbH: Springer, *Low-Energy Electron Diffraction: Experiment, Theory and Structural Determination*, by M. A. Van Hove, W. H. Weinberg and C.-M. Chan, © (1986) [5.3].

Unlike in bulk band structures, however, which normally assume no electron damping (no inelastic effects, especially below the Fermi level), in the LEED case we do have damping (given by an inelastic mean free path): as a result, the Bloch wave vector \mathbf{k}_B is always a complex quantity in LEED, representing the damping of waves from one layer to the next: one then speaks of a complex band structure.

In Eq. (5.40), the expansion coefficients depend on the index i because each layer intermixes the plane waves that are scattered by it. We shall need this mixing information and use it to relate the components of the Bloch waves φ_i , and φ_{i+1} , on either side of layer $i + 1$. This mixing is described by the layer-diffraction matrices $M_{\mathbf{g}'\mathbf{g}}^{\pm\pm}$ of Eqs. (5.16) and (5.21), which we shall write here in terms of reflection and transmission matrices similar to those given in Eq. (5.39),

$$\begin{aligned} R_{\mathbf{g}'\mathbf{g}}^{-+} &= p_{\mathbf{g}'}^{-} r_{\mathbf{g}'\mathbf{g}}^{-+} p_{\mathbf{g}}^{+} = p_{\mathbf{g}'}^{-} M_{\mathbf{g}'\mathbf{g}}^{-+} p_{\mathbf{g}}^{+}, \\ R_{\mathbf{g}'\mathbf{g}}^{+-} &= p_{\mathbf{g}'}^{+} r_{\mathbf{g}'\mathbf{g}}^{+-} p_{\mathbf{g}}^{-} = p_{\mathbf{g}'}^{+} M_{\mathbf{g}'\mathbf{g}}^{+-} p_{\mathbf{g}}^{-}, \\ T_{\mathbf{g}'\mathbf{g}}^{++} &= p_{\mathbf{g}'}^{+} t_{\mathbf{g}'\mathbf{g}}^{++} p_{\mathbf{g}}^{+} = p_{\mathbf{g}'}^{+} M_{\mathbf{g}'\mathbf{g}}^{++} p_{\mathbf{g}}^{+}, \\ T_{\mathbf{g}'\mathbf{g}}^{--} &= p_{\mathbf{g}'}^{-} t_{\mathbf{g}'\mathbf{g}}^{--} p_{\mathbf{g}}^{-} = p_{\mathbf{g}'}^{-} M_{\mathbf{g}'\mathbf{g}}^{--} p_{\mathbf{g}}^{-}, \end{aligned} \quad (5.43)$$

where

$$p_{\mathbf{g}}^{\pm} = e^{\pm i \mathbf{k}_{\mathbf{g}}^{\pm} \mathbf{a}/2}. \quad (5.44)$$

Many of these quantities are shown in Figure 5.9.

Now we can relate the components of the Bloch waves φ_i and φ_{i+1} :

$$\begin{aligned} \mathbf{b}_{i+1}^{+} &= \mathbf{T}^{++} \mathbf{b}_i^{+} + \mathbf{R}^{+-} \mathbf{b}_{i+1}^{-}, \\ \mathbf{b}_i^{-} &= \mathbf{T}^{--} \mathbf{b}_{i+1}^{-} + \mathbf{R}^{-+} \mathbf{b}_i^{+}, \end{aligned} \quad (5.45)$$

using matrix/vector notation. Equations (5.41), (5.42) and (5.45) can be combined, using double-length vectors, to yield the following eigenvalue equation:

$$\begin{pmatrix} \mathbf{T}^{++} & \mathbf{R}^{+-} \\ (\mathbf{T}^{--})^{-1} \mathbf{R}^{-+} \mathbf{T}^{++} & -(\mathbf{T}^{--})^{-1} \mathbf{R}^{-+} \mathbf{R}^{+-} + (\mathbf{T}^{--})^{-1} \end{pmatrix} \begin{pmatrix} \mathbf{b}_i^{+} \\ \mathbf{b}_{i+1}^{-} \end{pmatrix} = e^{i \mathbf{k}_B \mathbf{a}} \begin{pmatrix} \mathbf{b}_i^{+} \\ \mathbf{b}_{i+1}^{-} \end{pmatrix}. \quad (5.46)$$

Solving this equation yields eigenvectors which give the Bloch waves φ_i that we need, as well as the eigenvalues giving the Bloch wave vector \mathbf{k}_B for the electron energy and incidence direction under consideration. The double matrix dimension of Eq. (5.46) corresponds to the presence of Bloch waves that travel toward the bulk as well as Bloch waves that travel toward the vacuum: only the former are relevant for LEED, as those Bloch waves travelling toward the vacuum would require an electron source of the same energy E deep inside the surface.

The LEED wave functions in the bulk can also be obtained with an approach equivalent to the Bloch wave method, namely the transfer matrix method. The transfer matrix \mathbf{S} relates the plane waves from one layer to the next through

$$\begin{pmatrix} \mathbf{b}_{i+1}^+ \\ \mathbf{b}_{i+1}^- \end{pmatrix} = \mathbf{S} \begin{pmatrix} \mathbf{b}_i^+ \\ \mathbf{b}_i^- \end{pmatrix}, \quad \text{with } \mathbf{S} = \begin{pmatrix} \mathbf{T}^{++} - \mathbf{R}^{+-}(\mathbf{T}^{--})^{-1}\mathbf{R}^{-+} & \mathbf{R}^{+-}(\mathbf{T}^{--})^{-1} \\ -(\mathbf{T}^{--})^{-1}\mathbf{R}^{-+} & (\mathbf{T}^{--})^{-1} \end{pmatrix}, \quad (5.47)$$

which follows from our earlier relations. Diagonalising \mathbf{S} also yields the Bloch wave functions and eigenvalues.

We still need to match the Bloch waves to the plane waves in vacuum, which consist of one incident wave of given amplitude and a set of diffracted waves with unknown amplitudes: the matching will fix those unknown amplitudes. The simplest case is that of an abrupt termination of the bulk structure at the surface, such that the Bloch waves can be equated there to the vacuum waves: that equation solves the unknown amplitudes. However, in general, the surface structure deviates from the bulk structure, whether through different layer spacings, overlayers, 2-D superlattices, etc. In the general case, we have to match the plane waves between each pair of surface layers as well as between them and the vacuum waves, and between them and the bulk layers (where the Bloch waves exist): this provides enough conditions to solve the problem but is clearly more involved than for the case of an abrupt bulk termination.

The computational cost of the Bloch wave and transfer matrix approaches scales with the number of plane waves g used as $(2g)^3 + (2gs)^3$, if s is the number of surface matching planes. We shall describe more efficient schemes in Sections 5.2.6.2–5.2.6.5.

5.2.6.2 Layer-by-Layer Stacking

The multiple scattering by a pair of layers can be expressed as a series similar to that between two atoms (cf. Eqs. (5.10) and (5.11)) and can also be summed up exactly as in Eq. (5.46), using a closed matrix inversion. Referring to Figure 5.10, the reflection from the vacuum side of the double layer is the sum of reflection from layer A, reflection from layer B (involving transmission twice through layer A), double reflection from layer B, triple reflection from layer B, etc.:

$$\begin{aligned} \mathbf{R}^{-+} &= \mathbf{P}_1^- \mathbf{r}_A^- \mathbf{P}_1^+ \\ &\quad + \mathbf{P}_1^- \mathbf{t}_A^- \mathbf{P}^- \mathbf{r}_B^- \mathbf{P}^+ \mathbf{t}_A^{++} \mathbf{P}_1^+ \\ &\quad + \mathbf{P}_1^- \mathbf{t}_A^- \mathbf{P}^- \mathbf{r}_B^- \mathbf{P}^+ \mathbf{r}_A^+ \mathbf{P}^- \mathbf{r}_B^- \mathbf{P}^+ \mathbf{t}_A^{++} \mathbf{P}_1^+ + \dots \\ &= \mathbf{P}_1^- \left[\mathbf{r}_A^- + \mathbf{t}_A^- \mathbf{P}^- \mathbf{r}_B^- \mathbf{P}^+ (\mathbf{I} - \mathbf{r}_A^+ \mathbf{P}^- \mathbf{r}_B^- \mathbf{P}^+)^{-1} \mathbf{t}_A^{++} \right] \mathbf{P}_1^+. \end{aligned} \quad (5.48)$$

The various plane-wave propagators \mathbf{P} are similar to those of Eq. (5.44), with $\mathbf{a}/2$ replaced by the appropriate displacement vectors. Note that we here include transmission (\mathbf{t}_A^{++} and \mathbf{t}_A^{--}) through the intervening layer A: this transmission is a strong perturbation of the waves and cannot be treated as a weak effect.

Similarly, the reflection from the opposite side of the layer pair and the transmissions from both sides can be summed up to a closed form (for simplicity we now make planes 1 and A coincide, as well as planes 2 and B coincide):

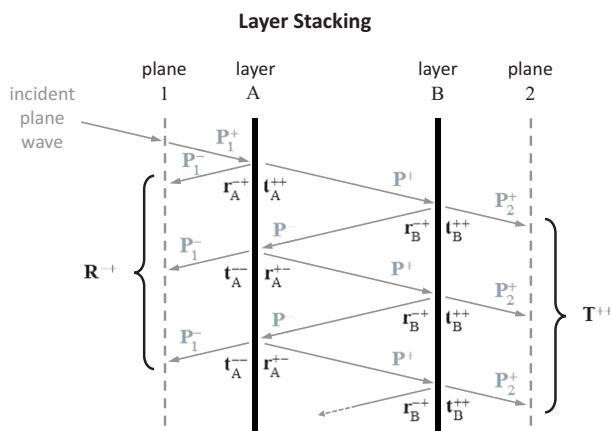


Figure 5.10 Layer stacking scheme for two layers. Two atomic layers A and B are shown as thick black vertical lines. Shown in grey are external reference planes 1 and 2 (dashed lines) and the plane-wave propagators \mathbf{P}^+ and \mathbf{P}^- (for propagation from one layer to the next) as well as the plane-wave propagators \mathbf{P}_1^+ , \mathbf{P}_1^- , \mathbf{P}_2^+ , \mathbf{P}_2^- (for propagation from plane 1 to layer A and back, and from layer B to plane 2 and back, respectively). The internal reflections between layers A and B can repeat as often as needed. Each arrow (except the incident plane wave) represents all possible diffracted waves \mathbf{g} . The exiting waves are summed to yield the converged reflection matrices \mathbf{R}^{+-} and transmission matrices \mathbf{T}^{++} for the pair of layers. The scheme is repeated for incidence from the right, unless left/right symmetry yields directly: $\mathbf{R}^{+-} = \mathbf{R}^{-+}$ and $\mathbf{T}^{--} = \mathbf{T}^{++}$. Adapted with permission from Springer Nature Customer Service Centre GmbH: Springer, *Low-Energy Electron Diffraction: Experiment, Theory and Structural Determination*, by M. A. Van Hove, W. H. Weinberg and C.-M. Chan, © (1986) [5.3].

$$\begin{aligned}
 \mathbf{R}^{-+} &= \mathbf{r}_A^{-+} + \mathbf{t}_A^{--} \mathbf{P}^- \mathbf{r}_B^{-+} \mathbf{P}^+ (\mathbf{I} - \mathbf{r}_A^{+-} \mathbf{P}^- \mathbf{r}_B^{-+} \mathbf{P}^+)^{-1} \mathbf{t}_A^{++}, \\
 \mathbf{R}^{+-} &= \mathbf{r}_B^{+-} + \mathbf{t}_B^{++} \mathbf{P}^+ \mathbf{r}_A^{+-} \mathbf{P}^- (\mathbf{I} - \mathbf{r}_B^{-+} \mathbf{P}^+ \mathbf{r}_A^{+-} \mathbf{P}^-)^{-1} \mathbf{t}_B^{--}, \\
 \mathbf{T}^{++} &= \mathbf{t}_B^{++} \mathbf{P}^+ (\mathbf{I} - \mathbf{r}_A^{+-} \mathbf{P}^- \mathbf{r}_B^{-+} \mathbf{P}^+)^{-1} \mathbf{t}_A^{++}, \\
 \mathbf{T}^{--} &= \mathbf{t}_A^{--} \mathbf{P}^- (\mathbf{I} - \mathbf{r}_B^{-+} \mathbf{P}^+ \mathbf{r}_A^{+-} \mathbf{P}^-)^{-1} \mathbf{t}_B^{--},
 \end{aligned} \tag{5.49}$$

with $P_{\mathbf{g}}^{\pm} = e^{\pm i \mathbf{k}_{\mathbf{g}}^{\perp} \cdot \mathbf{r}_{BA}}$, where \mathbf{r}_{BA} links a point in layer A with a point in layer B (specifically, these are the points with respect to which the layer reflection and transmission matrices are defined).

To stack more than two layers, we can add single atomic layers to a growing stack by repeating the steps of Eqs. (5.49), using reflection and transmission matrices calculated in the previous stacking step. This should be repeated until the stack thickness makes the reflection matrix elements $R_{\mathbf{g}0}^{+-}$ (giving the amplitudes of the diffracted plane waves) converge due to the inelastic mean free path, which typically happens after about 10 mono-atomic layers. The computational cost of layer stacking scales as $g^3 N$, for g plane waves and N layers.

5.2.6.3 Layer Doubling

In the bulk, layer stacking can be considerably accelerated by so-called layer doubling, illustrated in Figure 5.11. The bulk periodicity perpendicular to the surface (also used in the Bloch wave approach) allows doubling the layer thickness at each step: the first step combines two layers into one double layer, as discussed in Section 5.2.6.2. The second step would combine two such double layers into one quadruple layer. The third step would combine two quadruple layers into one octuple layer. A fourth step produces a stack of 16 layers, which is usually sufficient for convergence of the reflection by the stack.

The layer doubling method yields a full reflection matrix for the stack of equal layers. Other layers different from the bulk layers can then be added to the surface at will, using the individual layer stacking approach described in Section 5.2.6.2. For efficiency, the bulk reflection can be stored and used repeatedly for many different

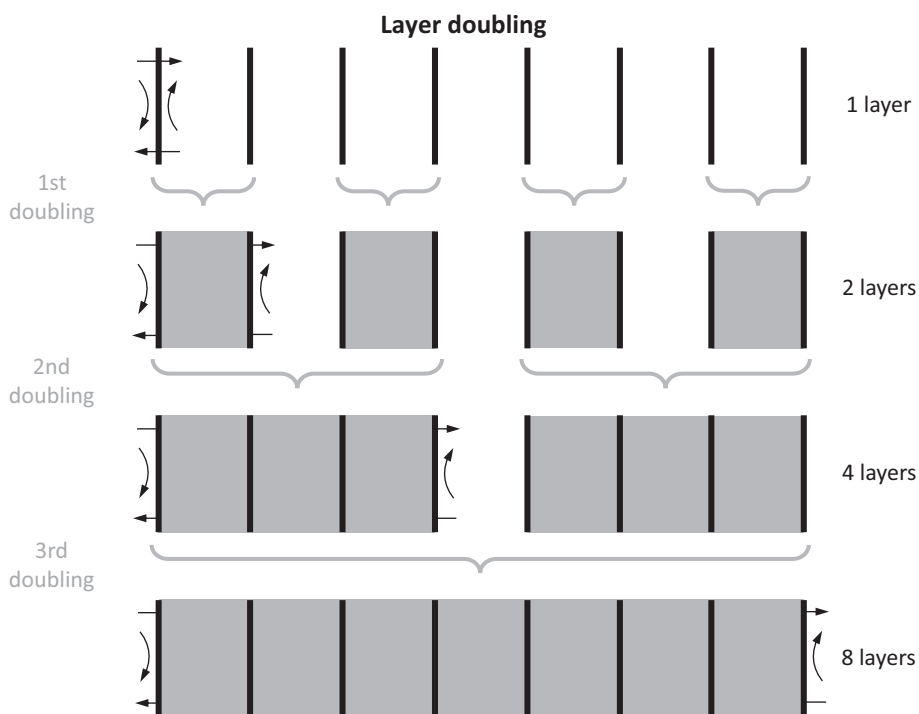


Figure 5.11 Layer doubling scheme, with surface at left, assuming identical atomic layers. First, the reflection and transmission matrices of a single layer (represented by arrows at top left) are used with the layer stacking scheme to pair up the left-most two layers, producing new reflection and transmission matrices for a pair of layers (arrows in second row). The process is repeated to grow the layer stack to 4, 8, 16, ... layers until convergence of the reflection matrices at the surface. Adapted with permission from Springer Nature Customer Service Centre GmbH: Springer, *Low-Energy Electron Diffraction: Experiment, Theory and Structural Determination*, by M. A. Van Hove, W. H. Weinberg and C.-M. Chan, © (1986) [5.3].

configurations of surface layers (such as different overlayer spacings and registries), a convenient feature in a surface structure search. The computational cost of layer doubling scales as $g^3 \ln N$, for g plane waves and N layers (N is now a power of 2).

5.2.6.4 Renormalised Forward Scattering (RFS)

An important aspect of the layer stacking described in Section 5.2.6.2 is the inclusion of transmission matrices in all the multiple scattering paths that are transmitted through layers. The reason is that forward transmission affects the waves strongly, both by redistributing amplitudes among plane waves and by modifying their phases significantly. By contrast, the backward reflection by an atomic layer can more justifiably be treated as a perturbation. That is the idea behind the renormalised forward scattering (RFS) method.

In RFS, the reflection by any layer is considered to be weak, and therefore the perturbation is based on an expansion of the total reflectivity of the surface in terms of the number of reflections. The first order contains all paths that have been reflected only once but transmitted any number of times; the second order contains only triple-reflection paths (an odd number of reflections is needed to bring electrons back out of the surface), and so on.

Figure 5.12 shows the time sequence of computations. The incident beam is weakly reflected (**r**) and also strongly transmitted (**t**) by the first layer; its

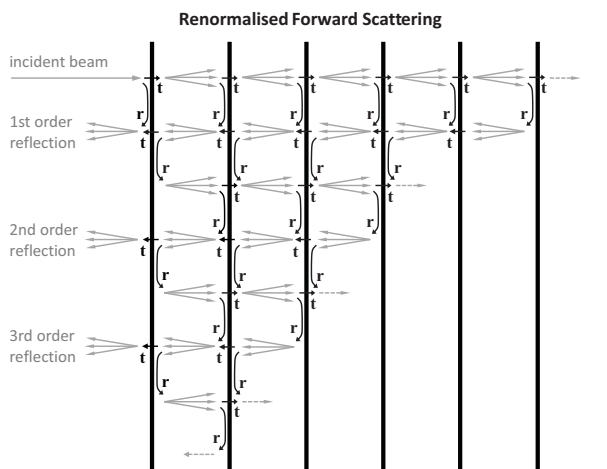


Figure 5.12 Renormalised forward scattering scheme. Each layer (thick black lines) may be different from the others, including different layer spacings and 2-D superlattices (which are normally assumed commensurate). Grey arrows indicate plane-wave propagation into and out of the surface, while black arrows indicate reflection (**r**) and transmission (**t**) at each layer (the matrices **r** and **t** may differ from layer to layer and may have left/right asymmetry). Each order of back scattering can penetrate to any depth required for convergence. Adapted with permission from Springer Nature Customer Service Centre GmbH: Springer, *Low-Energy Electron Diffraction: Experiment, Theory and Structural Determination*, by M. A. Van Hove, W. H. Weinberg and C.-M. Chan, © (1986) [5.3].

transmission causes a ‘shower’ of plane waves to hit the second layer, where they are reflected as well as transmitted; this transmission reaches the third layer and is then transmitted to the fourth layer, etc., until inelastic effects have weakened the penetrating waves sufficiently. Then the process is reversed: the reflected waves from the deepest layer are propagated outward, causing at each subsequent layer a weak reflection (into the surface) and a strong transmission (out of the surface); at each outward transmission, the waves reflected in the previous stage (during penetration of the incident waves) are picked up and added to the outward flux of waves; this results in the first-order exit from the surface. For the second order, the inward reflections from the first order process are propagated inward (again causing weak reflection and strong transmission at each layer) until they die out with depth, after which the new outward reflections are picked up and propagated outward into vacuum: there they are added to the previously obtained reflections from the first order. Additional orders are obtained by iteration of this scheme, until convergence of the total reflected amplitudes.

Typically, a dozen atomic layers and a few orders of reflection suffice for convergence. Occasionally, RFS does not converge well: then one may alternatively apply layer doubling or else combine layers into slabs within which strong multiple scattering can first be solved by matrix inversion (Eq. (5.16)) or by layer-by-layer stacking (Eqs. (5.49)) before handling by RFS. The computational effort of RFS scales as g^2N , for g plane waves and N layers, making it the most efficient method available for LEED. It is also very flexible in terms of surface deviations from the bulk (overlayers, reconstructions, superlattices, etc.).

5.2.6.5 The Case of Stepped Surfaces

Stepped and kinked surfaces (characterised by high Miller indices, i.e., vicinal orientations) present a special challenge to the multiple scattering theory of LEED. These surfaces have a relatively large area A of their 2-D unit cell (which stretches from one step edge to the next), a relatively small interlayer spacing d (measured perpendicular to the macroscopic surface) and relatively low symmetry (at most a mirror plane), at all depths below the surface. The number of plane waves (including evanescent waves) needed in LEED theory scales roughly as A/d , which rapidly becomes prohibitively large for stepped surfaces with wider terraces. Worse, in the plane wave representation, layer stacking fails to converge for interlayer spacings d below approximately 0.1 nm (1 Å), thus preventing structure determination for most stepped surfaces.

The giant-matrix method (cf. Section 5.2.5.2) is more effective. It uses spherical waves within a composite layer that should include enough atomic layers to match the penetration depth of electrons into the substrate; there is one layer for each periodically inequivalent atom in a terrace as well as in the buried continuation of the terrace down to the electron penetration depth. This approach requires matrix dimensions that increase in proportion to the number of included atoms (i.e., layers), which grows roughly as $1/d$ instead of A/d . Other advantages of using the giant-matrix method include: the calculation of matrix elements is quite fast and the solution of the system

of linear equations is only required for the measured beams (not for the full beam set required by plane-wave methods) and only for one incident beam.

Several other schemes have been proposed to deal with stepped surfaces. One approach is the use bundles of chains of atoms parallel to the steps, using cylindrical waves within chains [5.26]; it allows disordered arrays of steps and thus diffuse LEED, but it does not benefit from the periodicity of ordered steps. Two other approaches combine the plane-wave and spherical-wave expansions in such a way as to generate effectively larger interlayer spacings between groups of layers, bundled together to form a step: a variation of the transfer-matrix method [5.27] and a scheme based on a three-centre layer doubling algorithm [5.28]; these roughly halve the lower limit on d to about 0.05 nm (0.5 Å), but do not solve the problem in general.

We next briefly describe a method that applies to any stepped or kinked surface, at the cost of requiring higher accuracy in some parts of the calculation. It was first developed by X.-G. Zhang and A. Gonis [5.29; 5.30] for electronic band-structure problems. This real-space multiple-scattering theory (RS-MST) [5.31; 5.32] uses the spherical wave representation, like the giant-matrix method, but adds two further techniques: Fourier transformation to convert the surface problem into a one-dimensional problem; and the concept of 'removal invariance'. The latter technique states that removing one layer from a semi-infinite periodic stack of layers does not change the surface properties, such as the surface reflectivity: this leads to a self-consistent equation for the scattering matrix from that semi-infinite stack. To allow surface relaxations, namely changes in interlayer spacings and layer registries parallel to the surface, tensor LEED (cf. Section 5.4.1) is applied very effectively. Adsorbates, reconstructions, etc., could also be treated explicitly by adding atomic layers on top of the semi-infinite substrate, for example in a way similar to the calculation of multiple scattering in a cluster of atoms (cf. Section 5.2.3).

The RS-MST method was tested against layer doubling for Cu(311) with a bulk interlayer spacing d of 0.109 nm (1.09 Å) and Cu(331) with a bulk interlayer spacing d of 0.083 nm (0.83 Å) [5.32]: the agreement was very good wherever layer doubling itself converged and for energies below about 130 eV, above which some numerical instabilities occurred in RS-MST; these instabilities should be eliminated by increased accuracy in calculating interplanar propagators and in performing matrix inversion. The method was also applied to determine, from experiment, surface relaxations down to the fourth layer in Pt(210) [5.31], which has a bulk interlayer spacing d of 0.08765 nm (0.8765 Å): in particular, an outermost inward relaxation by $23 \pm 4\%$ was found, giving an interlayer spacing of 0.06749 ± 0.00351 nm (0.6749 ± 0.0351 Å), in qualitative agreement with other results.

5.2.6.6 Beam Subsets Independent in the Bulk

Usually the surface layers exhibit a superlattice in comparison with the 2-D lattice of the substrate layers and not all beams are generated by the substrate layers; that is, if the beam indices (hk) are related to the substrate lattice, then only the beams with integer (hk) are generated by the substrate and all beams with fractional indices have their origin in the surface layers. The total beam set generated by the superlattice can

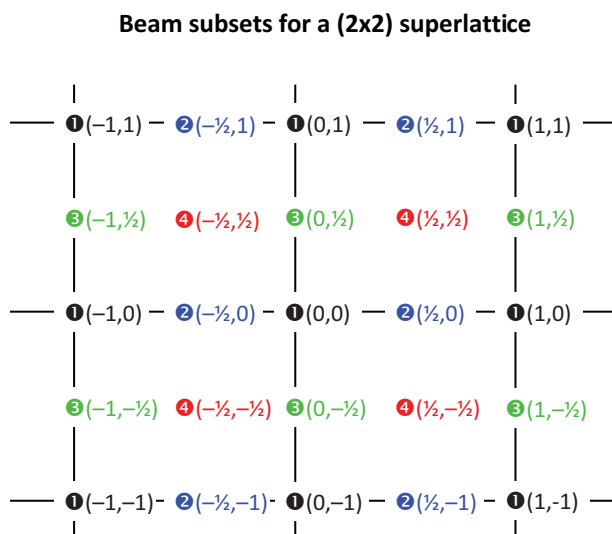


Figure 5.13 Beam subsets for a (2×2) superlattice on a rectangular substrate lattice. The 2-D reciprocal lattice of the substrate is drawn black with symbols ❶ and integer beam labels (h, k). The half-order beam ($\frac{1}{2}, 0$) gives rise to a shifted subset of beams ($\frac{1}{2} + h, k$) marked in blue as ❷. The half-order beam ($0, \frac{1}{2}$) likewise gives rise to beam subset ($h, \frac{1}{2} + k$) marked in green as ❸, while ($\frac{1}{2}, \frac{1}{2}$) generates the beam subset ($\frac{1}{2} + h, \frac{1}{2} + k$) marked in red as ❹. Adapted with permission from Springer Nature Customer Service Centre GmbH: Springer, *Low-Energy Electron Diffraction: Experiment, Theory and Structural Determination*, by M. A. Van Hove, W. H. Weinberg and C.-M. Chan, © (1986) [5.3].

be divided into subsets, as illustrated in Figure 5.13. One of the beams of each subset acts as a primary beam in the substrate layers exciting only beams belonging to this subset. The layer scattering matrices of substrate layers can therefore be block-diagonalised for subsets of beams, as illustrated in Figure 5.14. This block-diagonalisation can be used to save considerable computing effort in the various layer stacking schemes. For example, with layer doubling, the calculation time is substantially reduced if the backscattering matrices from the substrate are calculated separately for each subset.

5.3 Symmetry in Calculations

The time required for the calculation of the layer scattering matrices $M_{g'g}^{\pm\pm}$ (Eq. (5.35)) increases rapidly with the size of the surface unit cell and the number of atoms in it. The size of the matrices to be inverted can be reduced considerably by making use of symmetry relations. Symmetries are nearly always present when adsorbate structures are investigated on low-index surfaces of highly symmetric crystals like metals or semiconductors. The adsorbate structure itself may have a lower symmetry than the

**Block diagonalisation of a
substrate-layer diffraction matrix
with beam subsets for a (2x2) superlattice**

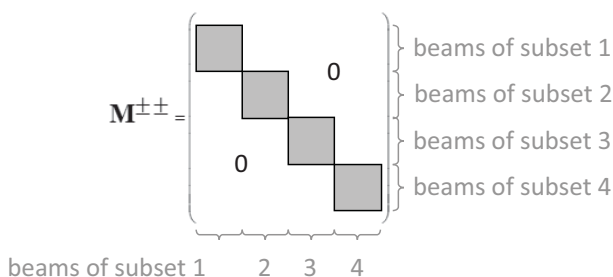


Figure 5.14 Block diagonalisation of a substrate-layer diffraction matrix with beam subsets for a (2×2) superlattice. The superlattice may be caused by an overlayer (e.g., ¼-monolayer adsorption) or by a reconstruction (e.g., missing atoms or commensurate modulation). Adapted with permission from Springer Nature Customer Service Centre GmbH: Springer, *Low-Energy Electron Diffraction: Experiment, Theory and Structural Determination*, by M. A. Van Hove, W. H. Weinberg and C.-M. Chan, © (1986) [5.3].

clean surface but usually at least some of the symmetry elements of the bulk structure are retained. As mentioned in Section 2.1.6, the existence of the surface reduces the 3-D space group of the substrate crystal to one of the 17 2-D space groups where only rotational axes normal to the surface and mirror planes with their normal parallel to the surface remain. Of the glide planes, only those with the normal in the surface plane and an in-plane glide vector remain. The symmetry of the LEED pattern, including its spot intensities, is that of the point symmetry of the structure combined with the incident beam. The incident beam must be invariant with respect to all symmetry operations. This is a result of multiple scattering and would not be the case for X-ray diffraction where the structure factor depends on the diffraction vector $\mathbf{q} = \mathbf{k}' - \mathbf{k}$ and not on the individual vectors \mathbf{k}' and \mathbf{k} . As a result, the full 2-D symmetry can only be used at normal incidence, while at oblique incidence only a mirror or glide plane can be used, assuming that the incident beam lies in that plane.

Most frequently, experiments are performed at normal incidence and at incidence within a mirror plane, since the orientation of the probe is then easily controlled by the symmetry of the diffraction spot intensities. The calculation of LEED intensities is usually divided into two parts. One part solves the multiple-scattering problem within a single atomic layer, mostly a composite layer with several atoms per unit cell. The second part uses a plane-wave expansion and combines the layer scattering matrices by using layer doubling, the RFS scheme or other equivalent schemes as described in Section 5.2. Symmetry operations can be used in both steps. We first describe the use of symmetry operations in the calculation of layer scattering matrices. There are

several ways to solve the multiple scattering equations (Eqs. (5.16) and (5.29)). The most general is the self-consistent solution by matrix inversion which will be considered in Sections 5.3.1 and 5.3.2; symmetry can be used similarly within other methods.

5.3.1 Symmetry in Reciprocal Space

We start with Eq. (5.35) for the reflection and transmission matrices for a multi-atomic layer where we explicitly write here the indices (l, m) instead of the abbreviation $L \equiv (l, m)$, because we need the single indices when describing the symmetry operators in angular momentum space.

$$M_{\mathbf{g}'\mathbf{g}}^{\pm\pm} = -\frac{16\pi^2 i m_e}{A k_{\mathbf{g}}^+ \hbar^2} \sum_{lm, l'm'} Y_{lm}(\mathbf{k}_{\mathbf{g}}^{\pm}) \sum_{i=1}^N \left\{ e^{i(\pm \mathbf{k}_{\mathbf{g}}^{\pm} \mp \mathbf{k}_{\mathbf{g}}^{\pm}) \cdot \mathbf{r}_i} T_{lm, l'm'}^i \right\} (-1)^{m'} Y_{l'-m'}(\mathbf{k}_{\mathbf{g}}^{\pm}) + \delta_{\mathbf{g}'\mathbf{g}} \delta_{\pm\pm}. \quad (5.50)$$

Here we have used $(-1)^m Y_{l,-m} = Y_L^*$. The sum over j runs over all atoms in the unit cell, which means over all subplanes of the layer. The vector \mathbf{r}_j gives the position of the atom j with respect to the origin of the unit cell. It is not required that an atom sits in the origin of the unit cell. The directions of the incoming and outgoing waves are indicated by the superscript \pm of the wave vectors and define whether reflection or transmission matrices are calculated. With the $+$ sign indicating the incidence from the vacuum side, we have $\mathbf{T}^{++} = \mathbf{M}^{++}$, $\mathbf{R}^{+-} = \mathbf{M}^{+-}$ and the transmission and reflection from the crystal side are given by $\mathbf{T}^{--} = \mathbf{M}^{--}$ and $\mathbf{R}^{-+} = \mathbf{M}^{-+}$. The indices \pm are left out for convenience in the following equations, keeping in mind that the matrices for incidence from the crystal side must be calculated with the beam set $\mathbf{k}_{\mathbf{g}}^-$.

The matrices \mathbf{T}^j describe the scattered wave around the j -th atom. They are the solution of a set of linear equations:

$$T_{lm, l'm'}^j(\mathbf{k}_{\mathbf{g}}) = \mathbf{t}^j(E) + \mathbf{t}^j(E) \sum_{l''m''} \sum_{\mu=1}^N G_{lm, l''m''}^{\mu}(\mathbf{k}_0) \cdot e^{i\mathbf{k}_{\mathbf{g}}(\mathbf{r}_j - \mathbf{r}_{\mu})} \cdot T_{l''m'', l'm'}^{\mu}(\mathbf{k}_{\mathbf{g}}), \quad (5.51)$$

$$G_{lm, l'm'}^{\mu}(\mathbf{k}_0) = -4\pi i \frac{2m_e}{\hbar^2} k \sum_{l_1 m_1} \sum_{\mathbf{P}} i^{l_1} a(L, L', L_1) h_{l_1}^{(1)}(k|\mathbf{r}_j - \mathbf{r}_{\mu} + \mathbf{P}|) Y_{l_1 m_1}(\mathbf{r}_j - \mathbf{r}_{\mu} + \mathbf{P}) e^{-i\mathbf{k}_0 \cdot \mathbf{P}}. \quad (5.52)$$

The propagator matrices $\mathbf{G}^{\mu}(\mathbf{k}_0)$ describe the transport of a spherical wave from point μ to point j , and are here defined without the phase factors $\exp[i\mathbf{k}_{\mathbf{g}}(\mathbf{r}_j - \mathbf{r}_{\mu})]$ which have been shifted into Eq. (5.51); they depend therefore on the incoming wave \mathbf{k}_0 only. The sum over \mathbf{P} runs over all lattice points within a limiting radius determined by the energy and the damping parameter. The quantities $\mathbf{t}^j(E)$ are diagonal matrices describing a single scattering event at atom j . The dimension of the matrix which must be

inverted to solve Eq. (5.51) is $N(l_{\max} + 1)^2$, where N is the number of atoms in the unit cell and $l_{\max} + 1$ is the number of angular momentum components used. The matrix $\mathbf{M}_{\mathbf{g}'\mathbf{g}}$ must be invariant under any symmetry operation that leaves unchanged both the crystal and the incident beam. Unfortunately, this symmetry property cannot be used in the present form of Eqs. (5.50) and (5.51), as the distance vector $\mathbf{r}_j - \mathbf{r}_\mu$ is in general not invariant under a symmetry operation. When there is only a single atom in the unit cell the origin can be chosen such that the phase factors $\exp[i(\mathbf{k}_\mathbf{g} - \mathbf{k}_{\mathbf{g}'})\mathbf{r}_j]$ in Eq. (5.51) vanish. It then becomes immediately clear that symmetry-adapted functions can be used. This is still possible when the origin of the layer is chosen to be at special points in the unit cell that have the full symmetry. A symmetry operation transforms point j into point j' , which must also be a lattice point in that case. The phase factors then remain unchanged:

$$e^{i\mathbf{k}_\mathbf{g}\mathbf{r}_j} = e^{i\mathbf{k}_\mathbf{g}\mathbf{r}_{j'}} \text{ when } \mathbf{r}_j - \mathbf{r}_{j'} = \mathbf{r}_n,$$

where \mathbf{r}_n is a translation vector and $\mathbf{k}_\mathbf{g}$ is a vector of the reciprocal net. In the following it is assumed that all the vectors $\mathbf{k}_\mathbf{g}$ and $\mathbf{k}_{\mathbf{g}'}$ belong to the reciprocal net of the surface lattice.

When there are atoms at general positions in the unit cell the phase factors are no longer invariant under a symmetry operation and the matrices \mathbf{T} no longer contain symmetries. Also, the propagator matrices $\mathbf{G}^{j\mu}(\mathbf{k}_0)$ are in general not invariant under a symmetry operation. This means that for an atom in a general position no symmetries can be used. The local point symmetry of that atom is 1 and the wave field around this atom also has no symmetry. Nevertheless, each general point in the unit cell is associated with one or more symmetrically equivalent points, the number of which depends on the position of that point and the space group. The matrices $\mathbf{T}^j(\mathbf{k}_\mathbf{g})$ can be transformed into each other by simple symmetry operators.

It is important to note that the sum over equivalent positions can be done prior to inversion of the matrix. To do that it is necessary to first perform the sum over equivalent beams in Eq. (5.50). There are n_g equivalent beams $\mathbf{k}_\mathbf{g}$ generated by all symmetry operations acting on $\mathbf{k}_\mathbf{g}$: this is usually called the beam star of $\mathbf{k}_\mathbf{g}$. Here and in the remainder of this section, $\mathbf{k}_\mathbf{g}$ denotes this beam star, that is, the set of symmetrically equivalent beams, saving a further subscript. Only for one beam of the star are the reflection and transmission matrix elements needed: by symmetry, the other corresponding matrix elements are equal. It is convenient to define the following quantities in angular momentum space [5.33]:

$$a_{lm}^j(\mathbf{k}_{\mathbf{g}'}) = (n_{\mathbf{g}'})^{1/2} \sum_{s=1}^{n_{\mathbf{g}'}} e^{(-i\mathbf{k}_{\mathbf{g}'}\mathbf{r}_j)} Y_{lm}(\mathbf{k}_{\mathbf{g}'}), \quad (5.53)$$

$$b_{lm}^j(\mathbf{k}_\mathbf{g}) = (n_g)^{1/2} t_l^j(E) \sum_{s=1}^{n_g} e^{(i\mathbf{k}_{\mathbf{g}s}\mathbf{r}_j)} (-1)^m Y_{l-m}(\mathbf{k}_{\mathbf{g}s}). \quad (5.54)$$

The matrices $\mathbf{T}^j(\mathbf{k}_\mathbf{g})$ are not explicitly needed to calculate $\mathbf{M}_{\mathbf{g}\mathbf{g}'}$ and Eq. (5.51) is solved directly for the vectors $\mathbf{Z}^j(\mathbf{k}_\mathbf{g})$:

$$\begin{aligned}
Z^j(\mathbf{k}_g) &= \mathbf{b}^j(\mathbf{k}_g) + \mathbf{t}^j(E) \sum_{\mu} \mathbf{G}^{j\mu}(\mathbf{k}_0) Z^{\mu}(\mathbf{k}_g), \text{ where} \\
Z_{lm}^j(\mathbf{k}_g) &= b_{lm}^j(\mathbf{k}_g) + t_{lm}^j(E) \sum_{l'm'} \sum_{\mu=1}^N G_{lm, l'm'}^{j\mu}(\mathbf{k}_0) Z_{l'm'}^{\mu}(\mathbf{k}_g) \\
&= \sum_{l'm'} (1 - \mathbf{X})_{vlm, \mu l'm'}^{-1} b_{l'm'}^{\mu}(\mathbf{k}_g).
\end{aligned} \tag{5.55}$$

The quantities $\mathbf{a}^j(\mathbf{k}_g)$ and $\mathbf{b}^j(\mathbf{k}_g)$ are vectors in angular momentum space and \mathbf{X} is a short notation for a large matrix with the propagator matrices $\mathbf{G}^{j\mu}$ as submatrices. They are not invariant under a symmetry operation but simple transformation rules exist. A symmetry operation of a space group may be denoted by (\mathbf{W}, \mathbf{w}) , see Section 2.1.8. \mathbf{W} is a point group operation and \mathbf{w} is a glide vector in a 2-D group. The operation acting on a vector \mathbf{r}^j transforms it into $\mathbf{r}^{j'}$. This is equivalent to a symmetry operation of the wave field incident on atom j , which is kept fixed. When a symmetry operation is applied to the beam star the vectors $\mathbf{a}^j(\mathbf{k}_g)$ and $\mathbf{b}^j(\mathbf{k}_g)$, Eqs. (5.53) and (5.54), remain invariant. The symmetry operation here acts only on the wave field and since $\mathbf{a}^j(\mathbf{k}_g)$ depends on the beam star \mathbf{k}_g it is invariant under a symmetry operation:

$$(\mathbf{W}, \mathbf{w}) \cdot \mathbf{a}^j(\mathbf{k}_g) = \mathbf{a}^{j'}(\mathbf{k}_g). \tag{5.56}$$

We use the notation $\mathbf{D}_{jj'}$ for the matrix transforming a vector \mathbf{r}^j to a vector $\mathbf{r}^{j'}$ or transforming the whole wave field. From the definitions given in Eqs. (5.53) and (5.54) and the properties of the spherical harmonics, it follows directly that a rotation about an n -fold axis with rotation angle $\varphi_n = 2\pi/n$ implies:

$$a_{lm}^{j'}(\mathbf{k}_g) = a_{lm}^j(\mathbf{k}_g) e^{im\varphi_n}. \tag{5.57}$$

The rotation of a position vector is equivalent to a rotation of the beam star in the opposite direction. A mirror plane at an angle γ to the x -axis leads to:

$$a_{lm}^{j'}(\mathbf{k}_g) = a_{l-m}^j(\mathbf{k}_g) (-1)^m e^{im2\gamma}. \tag{5.58}$$

A glide plane is connected with a phase factor in the reflected amplitude due to the glide vector \mathbf{w} and therefore

$$a_{lm}^{j'}(\mathbf{k}_g) = a_{l-m}^j(\mathbf{k}_g) (-1)^m e^{im2\gamma} e^{i\mathbf{k}_g \mathbf{w}}. \tag{5.59}$$

The transformation properties can be formally written as:

$$\mathbf{a}^{j'}(\mathbf{k}_g) = \mathbf{a}^j(\mathbf{k}_g) \mathbf{D}^{jj'}. \tag{5.60}$$

For the vectors $\mathbf{b}^j(\mathbf{k}_g)$ the same relations apply for the inverse matrices:

$$\mathbf{b}^{j'}(\mathbf{k}_g) = (\mathbf{D}^{jj'})^{-1} \mathbf{b}^j(\mathbf{k}_g). \tag{5.61}$$

The matrices $\mathbf{D}^{jj'}$ are unitary matrices in angular momentum space. They are diagonal for a rotation and change the sign of the m indices for a mirror or glide

plane. For the point groups they are independent of the wave vectors \mathbf{k}_g or $\mathbf{k}_{g'}$, while for groups with a glide plane they contain a phase factor $u_g = \exp(i\mathbf{k}_g \mathbf{w})$. In the 2-D symmetry groups only values $u_g = \pm 1$ occur. In Appendix G the index selection rules for all special positions in the 2-D symmetry groups are listed. The possible symmetry operations and glide vectors for all 17 2-D space groups are listed in Table 2.4.

The reflection and transmission matrices must remain unchanged under a symmetry operation of the crystal, and this leads to equivalent relations for the vectors $\mathbf{Z}^j(\mathbf{k}_g)$:

$$\mathbf{Z}^{j'}(\mathbf{k}_g) = (\mathbf{D}^{jj'})^{-1} \mathbf{Z}^j(\mathbf{k}_g). \quad (5.62)$$

These relations enable us to perform the sum over equivalent positions \mathbf{r}_i in Eq. (5.50). For this purpose, it is necessary to split the sum over subplanes or over all atoms in the unit cell into two parts. Summation indices (j, μ) refer to all atoms in the unit cell, where (j_0, μ_0) designate only symmetrically independent positions. Finally (j', μ') designate the set of equivalent positions generated by the symmetry operations. A summation index j' includes the position j_0 unless it is explicitly indicated otherwise under the summation sign. It should be kept in mind that at oblique incidence all rotation axes are lost and only mirror or glide planes coinciding with the plane of incidence are retained. The symmetry of the unit cell which can be used in the multiple scattering calculation is then only one of the groups pm, cm and pg. With these definitions one obtains from Eq. (5.55):

$$Z_{lm}^{j_0}(\mathbf{k}_g) = b_{lm}^{j_0}(\mathbf{k}_g) + t_l^{j_0}(E) \sum_{\mu_0} \sum_{\mu' \neq \mu_0} \sum_{l'm'} G_{lm, l'm'}^{j_0 \mu'}(\mathbf{k}_0) \sum_{l''m''} (\mathbf{D}^{\mu_0 \mu'})_{l'm', l''m''}^{-1} Z_{l''m''}^{\mu_0}(\mathbf{k}_g), \quad (5.63)$$

where use has been made of Eq. (5.62). We define new symmetrised interlayer propagators \mathbf{G}^S

$$\mathbf{G}^{S, j_0 \mu_0}(\mathbf{k}_0) = \sum_{\mu'} \mathbf{G}^{j_0 \mu'}(\mathbf{k}_0) (\mathbf{D}^{\mu_0 \mu'})^{-1}, \quad (5.64)$$

and Eq. (5.63) can then be written as

$$\mathbf{Z}^{j_0}(\mathbf{k}_g) = \mathbf{b}^{j_0}(\mathbf{k}_g) + \mathbf{t}^{j_0}(E) \sum_{\mu_0} \mathbf{G}^{S, j_0 \mu_0}(\mathbf{k}_0) \mathbf{Z}^{\mu_0}(\mathbf{k}_g). \quad (5.65)$$

This equation is completely equivalent to Eq. (5.55); the only difference is that the interlayer propagators \mathbf{G}^S describe the propagation of a spherical wave from a subplane j_0 to a subplane μ_0 , where the latter contains all symmetrically equivalent positions and is no longer a subplane within the former definition. The index j_0 in Eq. (5.65) now runs over all points in the asymmetric unit of the surface unit cell, that is, the scattering matrices \mathbf{T}^j or the vectors \mathbf{Z}^j must be calculated only for these points. Now the reflection and transmission matrices are simply given by

$$M_{\mathbf{g}\mathbf{g}'}^{\pm\pm} = \sum_j \mathbf{a}^j(\mathbf{k}_g^{\pm}) \mathbf{Z}^j(\mathbf{k}_g^{\pm}) = \sum_{j_0} n^{j_0} \mathbf{a}^{j_0}(\mathbf{k}_g^{\pm}) \mathbf{Z}^{j_0}(\mathbf{k}_g^{\pm}) + \delta_{\mathbf{g}\mathbf{g}'} \delta_{\pm\pm}, \quad (5.66)$$

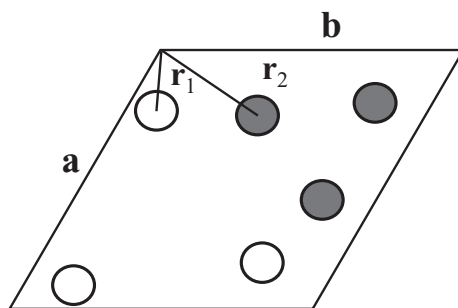


Figure 5.15 Example of a unit cell with symmetry p3 and two symmetrically inequivalent atoms in the unit cell with the local symmetry p1. Using the symmetry in Eqs. (5.51) and (5.52), the symmetrised subplane j_0 in Eq. (5.55) now contains all three symmetrically equivalent atoms (open circles) and subplane μ_0 contains the other three symmetrically atoms (shaded circles). Only two propagator matrices $\mathbf{G}^{S,j_0\mu_0}(\mathbf{k}_0)$ are needed with $j_0 = 1, 2$ and $\mu_0 = 1, 2$.

where n^{j_0} is the multiplicity of point j_0 . This is illustrated in Figure 5.15, where a hexagonal cell is shown with six atoms in the unit cell, two of which are independent with local symmetry p1. Without symmetry the whole plane is subdivided into six subplanes; if the symmetry p3 is used, we have two subplanes and the matrix to be inverted has dimension $2(l_{\max} + 1)^2$. In the calculation of the symmetrised propagator matrices $\mathbf{G}^{S,j_0\mu_0}(\mathbf{k}_0)$, Eq. (5.64), we must of course include all single propagator matrices according to all interatomic vectors within the unit cell.

So far, the size of the matrix to be inverted has been reduced because only symmetrically independent atoms need to be explicitly included. But this is not the only consequence of symmetry that can be used. Equation (5.50) has now been brought into a form suited for the introduction of symmetry-adapted functions. The symmetrisation in angular momentum space is coupled to that in \mathbf{k} -space in the sense that symmetries in angular momentum space can only be used when the corresponding sum over equivalent beams and the sum over equivalent atomic positions are also performed. That means that Eq. (5.65) must be solved instead of Eq. (5.55); otherwise the symmetry in angular momentum space is destroyed.

5.3.2 Symmetry in Angular Momentum Space

The appropriate way to take into account symmetries in connection with spherical harmonics is to use symmetry-adapted functions. These are linear combinations of spherical harmonics that are either invariant or have the required transformation properties under symmetry operations. The scattered wave from each atom can be expanded in terms of symmetry-adapted functions where the local point symmetry of the atom applies. It is necessary to introduce symmetries into the lattice sum given in Eq. (5.27) or (5.52). The first step is to perform the sum over equivalent atomic sites as well as the sum over equivalent beams in the system of equations defining the matrices \mathbf{T} and the reflection and transmission matrices.

Symmetry-adapted functions for all crystallographic point groups have been tabulated [5.34]; the irreducible representations for the point symmetries and the character tables can be found there. However, only the 17 2-D space groups are needed here and we shall summarise the index selection rules in the following. The 10 2-D point groups are considered first, since for these groups the transformation matrices do not depend on the wave vector \mathbf{k}_g or $\mathbf{k}_{g'}$. Consequently, only the unit representation is needed, provided that the wave vectors \mathbf{k}_g belong to the reciprocal net of the unit cell. When the point j is on an n -fold axis, Eq. (5.57) implies that

$$a_{lm}^{j'}(\mathbf{k}_g) = a_{lm}^j(\mathbf{k}_g) e^{im2\pi/n}, \quad (5.67)$$

and m should satisfy the condition $m = 0 \pmod{n}$. It is unimportant whether point j is at the origin or not, provided that the origin is chosen properly at the principal axis as usual; then the condition for m holds true for all other axes. It should be noted that this is only true for point groups and symmorphic groups (cm and c2mm): a glide operation can add a phase factor and m can take other values.

When point j lies on a mirror plane, Eq. (5.58) must be applied, where γ is the angle between the x -axis and the mirror plane. For all atoms on a mirror plane the spherical harmonics involving the vectors \mathbf{a}^j , \mathbf{b}^ν and \mathbf{Z}^ν can be replaced by the symmetry-adapted function

$$Y_{lm}^S = \frac{1}{\sqrt{2}} \{Y_{lm} + (-1)^m e^{im2\gamma} Y_{l-m}\}, \quad (5.68)$$

and only positive values of m are needed. These selection rules remain unaltered for the vectors \mathbf{Z}^ν and consequently also for the propagator matrices $\mathbf{G}^{S,j\mu}$. From the properties of the transformation matrices it follows that for an atom j_0 on an n -fold axis

$$G_{lm,l'm'}^{S,j_0,\mu_0}(\mathbf{k}_0) = 0, \quad \text{unless } m = 0 \pmod{n}. \quad (5.69)$$

This is a consequence of the fact that \mathbf{G}^S is a propagator from a subplane containing all symmetrically equivalent atoms. It is easy to show that for the indices $l'm'$ on the left-hand side of Eq. (5.69) the local point symmetry of atom μ_0 has to be taken. For an atom in a general non-symmetrical position, all spherical waves are needed and no reduction is possible. Here the reduction results from the fact that the sum over equivalent positions can be performed before inverting the matrix. For each atom, a different set of indices lm must be defined, according to its local symmetry, in such a way that the matrix to be inverted is reduced to its minimum size. The interlayer propagator matrices $G_{lm,l'm'}^{S,\nu_0\mu_0}$ are now rectangular matrices, where the indices lm take values belonging to the local symmetry of point ν_0 and the indices $l'm'$ refer to the local symmetry of point μ_0 . A scheme of the symmetrised matrix \mathbf{G}^S is shown in Figure 5.16.

The index selection rules are described in detail in Appendix G, see Table G.1. They apply for the point groups and symmorphic groups, which are here the groups cm and cmm: the propagators for the centred lattices can be calculated by choosing the primitive unit cell and retaining the mirror plane. For the other groups with glide

$$\mathbf{G}^S = \left(\begin{array}{cc|cc} \mathbf{G}^{S,11} & \mathbf{G}^{S,12} & & \\ \mathbf{G}^{S,21} & \mathbf{G}^{S,22} & & \\ \hline & & \mathbf{G}^{S,33} & \\ \hline & & & \end{array} \right) \left. \begin{array}{l} lm \text{ sequence} \\ \text{atom 1} \\ \text{atom 2} \end{array} \right\}$$

Figure 5.16 Scheme of the symmetrised propagator matrix \mathbf{G}^S . The submatrices are rectangular because some angular momentum components can be omitted as described by Eqs. (5.67–5.69).

planes (pg, p2gg, p2mg and p4gm) the calculation becomes more complicated. As mentioned in Appendix G, a glide operation changes the sign of the reflected amplitudes for those beams having an odd-order index parallel to the glide plane. The consequence is that different representations are required for different beams. A glide plane parallel to the x -axis with a glide vector of half of the translation vector implies that

$$a_{v,lm}(\mathbf{k}_g) = a_{v,l-m}(\mathbf{k}_g) \cdot (-1)^m e^{i\pi h}, \quad (5.70)$$

where $\mathbf{k}_g = \mathbf{k}_0 + h\mathbf{a}^* + k\mathbf{b}^*$ and h, k are indices of the beam \mathbf{k}_g , while \mathbf{a}^* and \mathbf{b}^* are the basis vectors of the 2-D reciprocal net. The superlattice translation vectors \mathbf{a} and \mathbf{b} must be used with integer indices h and k . Due to the shift of the atom a phase factor occurs in the symmetry operator and the propagator matrices have to be calculated twice for the two beam sets (i.e., the set with even index h and the set with odd index h), each having a different set of symmetry-adapted functions. This could be applied only to atoms placed directly on a glide plane. This position, however, is not a special position, that is, it has the local point symmetry 1 and a shift of the atom off the glide plane does not produce split positions, unlike positions on mirror planes. We therefore do not recommend using this possibility to reduce the size of the matrices. A detailed description of the index selection rules for the special positions in all 2-D point groups is given in Appendix G.

The full use of symmetries still allows optimising atomic positions, as long as those positions respect the overall symmetry as well as the local symmetry of each atom. The local symmetry of an atom cannot be changed in the optimisation procedure. For instance, if an atom is located on a mirror plane, it can be moved only within that mirror plane; that atom cannot be allowed to move out of the mirror plane, because the single atom would become two atoms on either side of that mirror plane, thus changing the number of atoms, changing the stoichiometry and potentially placing atoms too close together.

If it is desired to let atoms break the initial symmetry by moving away from a mirror or glide plane or from a rotational axis, then a new symmetry (or no symmetry) should be chosen for the optimised structure. Before starting the calculation of

interlayer propagators, the local symmetry of each atom needs to be labelled and the allowed shifts of the atomic positions have to be determined. Which coordinates are free is given by the Wyckoff positions.

The local symmetry fixes the lm sequence of the spherical harmonics for all atoms and the sequence can be stored in an index array. The sequence of atoms does not change during optimisation of the atomic parameters. All further referencing to the indices l and m is done via this index image. The subsequent calculation is then independent of the actual coordinates of each atom as long as its local symmetry and multiplicity are not changed. The ten point groups and the groups cm and cmm can be handled that way. For the remaining four groups containing glide planes the procedure requires more effort since an additional loop must be incorporated. The set of beams must be decomposed into two or more groups for which different symmetry-adapted functions are required. The propagator matrices must be calculated again, but the sum over lattice points need not be repeated, since it can be stored and used again. There is still an important gain in computing time and memory space compared with the calculation made without using symmetries. All 17 2-D space groups can be handled with the same program. Details of the calculation of interlayer propagator matrices and the lattice sum are given in Appendix G.

5.4 Approximations

The computational effort increases drastically with the number of symmetrically independent atoms in the unit cell. A number of approximations have been proposed to treat structures with large unit cells. Some of the methods turned out to be insufficiently precise for general applications and are not used any more. We consider here only three methods: tensor LEED, frozen LEED and diffuse LEED. Tensor LEED is widely used in connection with optimisation methods and reduces the computation time substantially, especially in its symmetrised version. Frozen LEED is less used but should provide similar improvement as tensor LEED. Diffuse LEED applies to crystalline surfaces with some disorder that produces diffuse LEED patterns.

Methods applied to nanostructures with a very large number of atoms and without requiring translation symmetry have been described in Section 5.2.4. NanoLEED is not considered to be an approximation because the numerical precision can be chosen, for example by the grid size in the sparse-matrix canonical grid (SMCG) method (see Section 5.2.4.1) and leads to a correct solution within numerical errors. Approximation methods, on the other hand, contain systematic errors as some parts of the multiple scattering equations are omitted. The errors, nevertheless, are small and tolerable if the limits for parameter variation are set sufficiently small.

5.4.1 Tensor LEED Approximation

Tensor LEED (TLEED) is an efficient method for calculating the change in the scattering amplitude as a function of the shift of an atom. It is used in combination

with optimisation procedures where many $I(V)$ calculations are required for the variation of atomic parameters. A full dynamical calculation is performed for a reference structure and the change in diffraction intensities is approximately calculated from the shift of atomic parameters, most often shifted atomic positions. It is valid in a limited range of about 0.04 nm (0.4 Å) for coordinate shifts [5.35]. Variations of chemical element, Debye–Waller factors and site occupation factors are possible as well. The approximate part of the tensor LEED calculation is relatively very fast, enabling extensive exploration of many structures deviating from a single reference structure. This exploration is particularly useful for steepest descent schemes to optimise atomic positions and other parameters (steepest descent leads to a new reference structure, but this iterative step is usually not necessary, due to the good quality of the tensor LEED approximation).

The theory and applications of tensor LEED are described in a number of publications by P. J. Rous and J. B. Pendry, in particular [5.36; 5.37]. The formalism described there refers to the application in the RFS scheme, see Section 5.2.6.4. We describe here the tensor LEED formalism for use with the layer doubling method. That means we need to calculate the change of all matrix elements of the reflection and transmission matrices for all composite layers in which atom parameters are optimised (composite layers contain more than one atom per 2-D unit cell). Then those layers must be combined with the other layers by the layer doubling scheme. This is the most general application. Tensor LEED requires much storage space in this case. Alternatively, all atoms in the surface slab can be put in a single layer of sufficient thickness so that backscattering from deeper layers can be ignored: this approach is often called the giant-matrix method, cf. Section 5.2.5.2. Although the dimension of the matrix to be inverted becomes very large, the method is quite efficient as only one vector of the reflection matrix $\mathbf{R}_{\mathbf{g}\mathbf{g}}$ need be calculated, for $\mathbf{g} = 0$, that is, the incident beam. There is only one incident beam \mathbf{k}_0 and only the reflection amplitudes for those beams which are measured need to be calculated. It should be checked before starting an analysis whether the giant-matrix method or the layer doubling method is more efficient or whether the RFS scheme is applicable when small layer distances occur. If layer distances are large enough, larger than about 0.1 nm, the RFS scheme is certainly the most efficient for stacking layers.

We start again with Eq. (5.35), slightly adapted, which describes the scattering amplitude for an incoming wave $\mathbf{k}_{\mathbf{g}}$ into the direction $\mathbf{k}_{\mathbf{g}'}$:

$$M_{\mathbf{g}\mathbf{g}}^{\pm\pm} = -\frac{16\pi^2 m_e}{Ak_{\mathbf{g}}^+ h^2} \sum_{LL'} Y_L(\mathbf{k}_{\mathbf{g}}^{\pm}) \sum_{i=1}^N \left\{ e^{i(\pm\mathbf{k}_{\mathbf{g}}^{\pm} \mp \mathbf{k}_{\mathbf{g}}^{\pm}) \cdot \mathbf{r}_i} T_{LL'}^i \right\} Y_{L'}^*(\mathbf{k}_{\mathbf{g}}^{\pm}) + \delta_{\mathbf{g}'\mathbf{g}} \delta_{\pm\pm}, \quad (5.72)$$

where N is the number of atoms in the unit cell. The directions of incoming and outgoing waves are omitted in the following equations for convenience and will be inserted in the final equations to distinguish reflection and transmission matrices, as in Section 5.2.5. Here, $\mathbf{k}_{\mathbf{g}}^+$ is the incoming wave from the vacuum side and $\mathbf{k}_{\mathbf{g}}^- = -\mathbf{k}_{\mathbf{g}}^+$ is

the incoming wave from the crystal side. The signs of the wave vectors must be chosen according to the matrices that are calculated. The vectors \mathbf{r}_j are the position vectors of all atoms in the unit cell with respect to the origin of the composite layer. The use of symmetries and the reduction to symmetrically independent atoms in the unit cell are described in Appendix H.

The scattering matrices \mathbf{T}^j describe the wave leaving the atom at point \mathbf{r}_j without further scattering. \mathbf{T}^j is calculated in the angular momentum expansion:

$$T_{lm, l'm'}^j(\mathbf{k}_g) = t_l^j(E) + t_l^j(E) \sum_{\mu=1}^N \sum_{l''m''} G_{lm, l''m''}^{j\mu}(\mathbf{k}_0) e^{i\mathbf{k}_g(\mathbf{r}_j - \mathbf{r}_{\mu})} T_{l''m'', l'm'}^{\mu}(\mathbf{k}_g). \quad (5.73)$$

One can define the following vectors in angular momentum space:

$$a_{lm}^j(\mathbf{k}_g) = e^{-i\mathbf{k}_g \mathbf{r}_j} Y_{lm}(\mathbf{k}_g), \quad (5.74)$$

$$b_{lm}^j(\mathbf{k}_g) = e^{i\mathbf{k}_g \mathbf{r}_j} (-1)^m Y_{l-m}(\mathbf{k}_g), \quad (5.75)$$

and

$$\begin{aligned} Z_{lm}^j(\mathbf{k}_g) &= t_l^j(E) b_{lm}^j(\mathbf{k}_g) + t_l^j(E) \sum_{l'm'} \sum_{\mu=1}^N G_{lm, l'm'}^{j\mu}(\mathbf{k}_0) Z_{l'm'}^{\mu}(\mathbf{k}_g) \\ &= t_l^j(E) \sum_{l'm'} \sum_{\mu=1}^N [(1 - X^{-1})]_{lm, l'm'}^{j\mu} b_{l'm'}^{\mu}(\mathbf{k}_g). \end{aligned} \quad (5.76)$$

With these vectors, Eq. (5.72) can be written as

$$M_{\mathbf{g}'\mathbf{g}}^{\pm\pm} = -\frac{16\pi^2 i m_e}{A k_{\mathbf{g}'}^+ \hbar^2} \sum_{lm} \sum_{j=1}^N a_{lm}^j(\mathbf{k}_{\mathbf{g}'}^{\pm}) t_l^j Z_{lm}^j(\mathbf{k}_{\mathbf{g}}^{\pm}) + \delta_{\mathbf{g}'\mathbf{g}} \delta_{\pm\pm}. \quad (5.77)$$

Here $\mathbf{Z}^j(\mathbf{k}_g)$ represents the incoming spherical waves from all surrounding atoms, and $\mathbf{a}^j(\mathbf{k}_{g'})$ is the diffracted wave, leaving atom j without further scattering. In Eq. (5.77) the single scattering matrix \mathbf{t}^j occurs now between the vectors $\mathbf{a}^j(\mathbf{k}_{g'})$ and $\mathbf{Z}^j(\mathbf{k}_g)$. This allows us to modify \mathbf{t}^j and leave the incoming waves from the surroundings unchanged. In the tensor LEED approximation the atom at point \mathbf{r}^j is shifted from the position in the reference structure, while the incoming wave field is transported to the new position, as is the outgoing wave field, but the propagator matrices $\mathbf{G}^{j\mu}(\mathbf{k}_0)$ in the \mathbf{X} matrix (Eq. (5.76)) remain unchanged. An illustration of the method is shown in Figure 5.17. The tensor LEED approximation can be described as a ‘frozen \mathbf{X} matrix’ approximation.

A shift of atom j by $\delta\mathbf{r}^j$ changes the diffracted amplitude, that is, the matrix element $M_{\mathbf{g}'\mathbf{g}}$ of the reference structure, to $M'_{\mathbf{g}'\mathbf{g}}$:

$$M'_{\mathbf{g}'\mathbf{g}} = M_{\mathbf{g}'\mathbf{g}} + \delta M_{\mathbf{g}'\mathbf{g}}. \quad (5.78)$$

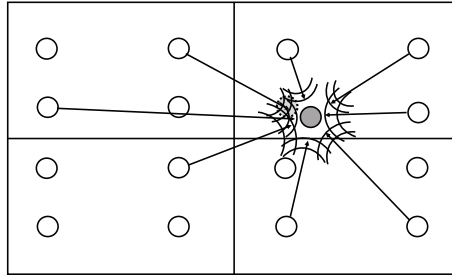


Figure 5.17 Illustration of the tensor LEED approximation. The shaded atom is shifted from its original position and the field of spherical waves coming from the surrounding atoms remains unchanged but is propagated to the new position.

We approximate $\delta M_{\mathbf{g}'\mathbf{g}}$ by shifting only the atomic t-matrix $t^j(E)$ in Eq. (5.77) and leaving the propagator matrices occurring in Eq. (5.76) unchanged. We thus replace $t_l^j(E)$ by:

$$t_{lm,l'm'}^j = t_{lm,l'm'}^j \delta_{ll'} \delta_{mm'} + \delta t_{lm,l'm'}^j, \quad (5.79)$$

which becomes a non-diagonal matrix. To obtain the angular momentum expansion from the phase factors in real space we can make use of the spherical wave expansion of a plane wave:

$$e^{i\mathbf{k}\mathbf{r}} = \sum_{lm} 4\pi i^l j_l(kr) Y_{lm}(\Omega_r) (-1)^m Y_{l-m}(\Omega_k). \quad (5.80)$$

With

$$\mathbf{t}^j(\mathbf{k}'_g, \mathbf{k}_g) = e^{i\mathbf{k}'_g \delta \mathbf{r}^j} \mathbf{t}^j(\mathbf{k}'_g, \mathbf{k}_g) e^{-i\mathbf{k}_g \delta \mathbf{r}^j}, \quad (5.81)$$

we obtain

$$\delta \mathbf{t}^j(\mathbf{k}'_g, \mathbf{k}_g) = e^{-i\mathbf{k}'_g \delta \mathbf{r}^j} \mathbf{t}^j(\mathbf{k}'_g, \mathbf{k}_g) e^{i\mathbf{k}_g \delta \mathbf{r}^j} - \mathbf{t}^j(\mathbf{k}'_g, \mathbf{k}_g). \quad (5.82)$$

In Eq. (5.82) the change of the t-matrix is defined as a function of the wave vectors; however, we need the expansion in spherical harmonics. The transformation of a t-matrix from spherical waves to a function of wave vectors is given by

$$t(-\mathbf{k}', \mathbf{k}) = 8\pi^2 \sum_{lm} \sum_{l'm'} (-1)^l Y_{lm}(\mathbf{k}') t_{lm,l'm'} (-1)^{m'} Y_{l'-m'}(\mathbf{k}), \quad (5.83)$$

and the reciprocal transformation gives

$$t_{lm,l'm'} = \frac{1}{8\pi^2} \iint (-1)^{l+m} Y_{l-m}(\mathbf{k}') t(\mathbf{k}', \mathbf{k}) Y_{l'm'}(\mathbf{k}) d\Omega_k d\Omega_{k'}. \quad (5.84)$$

Inserting Eq. (5.82) into Eq. (5.84) we obtain

$$\begin{aligned} \delta t_{lm, l'm'}^j = & \sum_{l_2=0, m_2}^{l_s} 4\pi i^{l_2} j_{l_2}(k\delta r^j) Y_{l_2 m_2}(\delta \mathbf{r}^j) \\ & \cdot \sum_{l_3=0, m_3}^{l_{\max}} \sum_{l_5=0, m_5}^{l_s} (-1)^{m_2+m} a(l_2 - m_2, l_3 m_3, l - m) t_{l_3}^j (-1)^{m_3+m_5} \\ & \cdot a(l_3 - m_3, l_5 - m_5, l' m') 4\pi i^{l_5} j_{l_5}(k\delta r^j) Y_{l_5 m_5}(\delta \mathbf{r}^j) - t_{lm}^j \delta_{ll'} \delta_{mm'}, \end{aligned} \quad (5.85)$$

where summation over m_2 is implied from $-l_2$ to $+l_2$, and similarly for m_3 and m_5 . The upper limit l_s for l_2 and l_5 is set by the value where the spherical Bessel function $j_l(k\delta r^j)$ becomes negligibly small, usually $l_s \leq 3$ or 4. The quantities $a(LM, L'M', lm)$ are Clebsch–Gordan-like coefficients or Gaunt coefficients (Eq. (5.9)):

$$a(LM, L'M', lm) = \int (-1)^M Y_{L-M}(\Omega) Y_{L'M'}(\Omega) (-1)^m Y_{l-m}(\Omega) d\Omega, \quad (5.86)$$

with the conditions

$$M - M' + m = 0, |L' - l| \leq L \leq |L' + l|, L + L' + l = \text{even}. \quad (5.87)$$

We obtain, finally, for the change in the diffraction amplitudes:

$$\begin{aligned} \delta M_{\mathbf{g}'\mathbf{g}} = & -\frac{16\pi^2 i m_e}{A k_{\mathbf{g}z}^+ \hbar^2} \sum_j \sum_{l_2 m_2} 4\pi i^{l_2} j_{l_2}(k\delta r^j) Y_{l_2 m_2}(\delta \mathbf{r}^j) \\ & \cdot \sum_{lm} \sum_{l'm'} \sum_{l_3 m_3} \sum_{l_5 m_5} a_{lm}^j(\mathbf{k}'_{\mathbf{g}}) \left\{ (-1)^{m_2+m} a(l_2 - m_2, l_3 m_3, l - m) t_{l_3}^j \right. \\ & \cdot (-1)^{m_3+m_5} a(l_3 - m_3, l_5 - m_5, l' m') 4\pi i^{l_5} j_{l_5}(k\delta r^j) Y_{l_5 m_5}(\delta \mathbf{r}^j) - t_l^j \left. \right\} Z_{l'm'}^j(\mathbf{k}_{\mathbf{g}}). \end{aligned} \quad (5.88)$$

It is convenient to define the vectors

$$\begin{aligned} S_{l_2 m_2}^{a,j} &= 4\pi i^{l_2} j_{l_2}(k\delta r^j) Y_{l_2 m_2}(\delta \mathbf{r}^j) \\ S_{l_5 m_5}^{b,j} &= 4\pi i^{l_5} j_{l_5}(k\delta r^j) Y_{l_5 m_5}(\delta \mathbf{r}^j) \end{aligned} \quad (5.89)$$

and a tensor:

$$\begin{aligned} F_{l_2 m_2, l_5 m_5}^j(\mathbf{k}_{\mathbf{g}'}, \mathbf{k}_{\mathbf{g}}) = & \sum_{lm} \sum_{l'm'} \sum_{l_3 m_3} a_{lm}^j(\mathbf{k}'_{\mathbf{g}}) \left[(-1)^{m_2+m} a(l_2 - m_2, l_3 m_3, l - m) t_{l_3}^j \right. \\ & \cdot (-1)^{m_3+m_5} a(l_3 - m_3, l_5 - m_5, l' m') - t_l^j \left. \right] Z_{l'm'}^j(\mathbf{k}_{\mathbf{g}}). \end{aligned} \quad (5.90)$$

The change of the scattering amplitude is then obtained as:

$$\delta M_{\mathbf{g}'\mathbf{g}} = -\frac{16\pi^2 i m_e}{A k_{\mathbf{g}z}^+ \hbar^2} \sum_{l_2 m_2} \sum_{l_5 m_5} \sum_{j=1}^N S_{l_2 m_2}^{a,j} F_{l_2 m_2, l_5 m_5}^j S_{l_5 m_5}^{b,j}. \quad (5.91)$$

The tensor $F_{l_2 m_2, l_5 m_5}^j(\mathbf{k}_g', \mathbf{k}_g)$ can be split into two independent parts, one for the incident beam set \mathbf{k}_g and a second part for the diffracted beam set \mathbf{k}_g' , which allows the computational storage space to be reduced. We now include the direction of the wave vectors, which is needed to differentiate the reflection and transmission matrices:

$$\begin{aligned} f_{l_2 m_2, l_3 m_3}^{a, j, \pm} &= \sum_{lm} a_{lm}^j(\mathbf{k}_g^{\pm}) \left[(-1)^{m_2+m} a(l_2 - m_2, l_3 m_3, l - m) t_{l_3}^j - t_l^j \right], \\ f_{l_3 m_3, l_5 m_5}^{b, j, \pm} &= \sum_{l'm'} (-1)^{m_3+m_5} a(l_3 - m_3, l_5 - m_5, l' m') Z_{l'm'}^j(\mathbf{k}_g^{\pm}). \end{aligned} \quad (5.92)$$

Now the scattering matrix is obtained as the product of two independent parts:

$$\delta M_{\mathbf{g} \mathbf{g}'}^{\pm \pm} = -\frac{16\pi^2 i m_e}{A k_{\mathbf{g} \mathbf{g}'}^+ \hbar^2} \sum_{j=1}^N \sum_{l_2 m_2} \sum_{l_3 m_3} S_{l_2 m_2}^{a, j} f_{l_2 m_2, l_3 m_3}^{a, j, \pm} \sum_{l_5 m_5} f_{l_3 m_3, l_5 m_5}^{b, j, \pm} S_{l_5 m_5}^{b, j}. \quad (5.93)$$

Equation (5.93) is the final solution. The tensor $F_{l_2 m_2, l_5 m_5}^j(\mathbf{k}_g', \mathbf{k}_g)$ and its two parts defined in Eq. (5.92) depend only on the reference structure and need to be calculated only once, while the shift of atom j only affects the vectors \mathbf{S}^a and \mathbf{S}^b . The change in scattering amplitude is thus obtained by a multiplication of a vector with a matrix instead of a new matrix inversion, saving considerable computing time. The Bessel functions j_l occurring in the shift vectors also need to be calculated only once for a grid of shifts and can be interpolated to intermediate values.

The tensor LEED approximation allows a very fast calculation of $I(V)$ curves for structures in the vicinity of a reference structure. It does require a large amount of storage space depending on the size of the unit cell and the number of phase shifts used. The tensor $F_{l_2 m_2, l_5 m_5}^j(\mathbf{k}_g', \mathbf{k}_g)$ depends on the wave vectors of the incoming beams \mathbf{k}_g and the diffracted beams \mathbf{k}_g' , while the two parts f^a and f^b have to be stored for all beams and all energies. As mentioned at the beginning of this section, the tensor LEED approximation is particularly useful in cases where the RFS scheme can be used or all atoms are combined in a single layer, that is, where the giant-matrix method is used. Then only one incoming wave exists and the second part of the tensor only needs to be stored for the measured beams, not for the whole beam set required in the coupling of layers. The coupling of layers with the layer doubling method is then avoided as well. In many cases this largely overcomes the larger computational effort needed in the multiple scattering calculation for the reference structure.

Tensor LEED can be symmetrised in the same way as a full dynamical calculation. When the structure exhibits a symmetry, this must not be changed in the optimisation process, as mentioned in Section 5.3. The use of symmetries reduces the size of the tensor substantially, as only selected indices are required in the (l, m) sequence of the spherical harmonics. The symmetrisation of the tensor is described in Appendix H.

5.4.2 Frozen LEED Approximation

A further approximation, frozen LEED, has been proposed by Z. X. Yu and S. Y. Tong [5.38]. Frozen LEED has close conceptual similarities to tensor LEED,

including the use of a reference structure for which a full dynamical calculation is performed. However, frozen LEED exhibits a larger radius of convergence of about 0.08 nm (0.8 Å): this larger radius allows exploring other nearby minima in a structural search, rather than only the nearest minimum, without needing a new full dynamical calculation for a new reference structure, for example, by use of simulated annealing.

Instead of calculating the change of the diffraction amplitude as a function of a shift of a single atom, as is done in tensor LEED, frozen LEED considers a shift of a whole subplane. For that purpose, we must slightly rewrite Eq. (5.73), which defines the matrices \mathbf{T} for all atoms in the unit cell while the propagator matrices contain the sum over all inter-atomic distances including the translation vectors, by adding a sum over translationally equivalent atoms \mathbf{P} :

$$T_{LL'}^j(\mathbf{k}_g) = t_l^j(E) + t_l^j(E) \sum_{\mathbf{P}} \sum_{\mu=1}^N \sum_{L''} G_{LL''}^{j\mu}(\mathbf{k}_0) e^{i\mathbf{g}(\mathbf{r}_\mu - \mathbf{r}_j + \mathbf{P})} T_{L''L'}^\mu(\mathbf{k}_g), \quad (5.94)$$

where the sum over inter-atomic distances has been extracted from the propagator matrices $\mathbf{G}^{j\mu}$ which are now defined as

$$G_{LL'}^{j\mu}(\mathbf{k}_0) = -4\pi i \frac{2m_e}{\hbar^2} k \sum_{\mathbf{P}} \sum_{L_1} i^{l_1} a(L, L', L_1) h_{l_1}^{(1)}(k|\mathbf{P} + \mathbf{r}_j - \mathbf{r}_\mu|) Y_{L_1}(\mathbf{P} + \mathbf{r}_j - \mathbf{r}_\mu) e^{-i\mathbf{k}_0 \mathbf{P}}. \quad (5.95)$$

For the case $j = \mu$ (i.e., for one subplane) the sum over lattice points reduces to the sum over lattice vectors. This is the same for all subplanes:

$$G_{LL'}^P(\mathbf{k}_g) = -4\pi i \frac{2m_e}{\hbar^2} k \sum_{\mathbf{P} \neq \mathbf{0}} \sum_{l_1 m_1} i^{l_1} a(L, L', L_1) h_{l_1}^{(1)}(k|\mathbf{P}|) Y_{L_1}(\mathbf{P}) e^{i\mathbf{k}_g \mathbf{P}}. \quad (5.96)$$

Equation (5.94) becomes:

$$T_{LL'}^j(\mathbf{k}_g) = t_l^j(E) + t_l^j(E) G_{LL'}^P(\mathbf{k}_g) + t_l^j(E) \sum_{\mathbf{P}, \mu \neq j} \sum_{L''} G_{LL''}^{j\mu}(\mathbf{k}_0) \cdot e^{i\mathbf{k}_g(\mathbf{r}_j - \mathbf{r}_\mu + \mathbf{P})} T_{L''L'}^\mu(\mathbf{k}_g). \quad (5.97)$$

We can define subplane t-matrices τ^j (as already defined in Eq. (5.23)) which are calculated from a much smaller set of linear equations:

$$\tau_{LL'}^j(\mathbf{k}_g) = t_l^j(E) + t_l^j(E) \sum_{L''} G_{LL''}^P(\mathbf{k}_g) \tau_{L''L'}^j(\mathbf{k}_g). \quad (5.98)$$

We insert these into Eq. (5.97). After some rearrangement of the matrix multiplications and making use of the matrix equation $(\mathbf{A} + \mathbf{B})^{-1} = (\mathbf{1} + \mathbf{A}^{-1}\mathbf{B})^{-1}\mathbf{A}^{-1}$ we obtain (analogously to Eq. (5.26)):

$$T_{LL'}^j(\mathbf{k}_g) = \tau_{LL'}^j(\mathbf{k}_g) + \tau_{LL'}^j(\mathbf{k}_g) \sum_{\mathbf{P}, \mu \neq j} \sum_{L''} G_{LL''}^{j\mu}(\mathbf{k}_0) e^{i\mathbf{k}_g(\mathbf{r}_\mu - \mathbf{r}_j)} T_{L''L'}^\mu(\mathbf{k}_g). \quad (5.99)$$

We use the vectors \mathbf{a}^j and \mathbf{b}^j in angular momentum space, defined previously in Eqs. (5.73) and (5.74), and an additional vector \mathbf{c}^j :

$$a_L^j(\mathbf{k}_{\mathbf{g}}') = e^{-i\mathbf{k}_{\mathbf{g}}' \cdot \mathbf{r}_j} Y_L(\mathbf{k}_{\mathbf{g}}'), \quad (5.100)$$

$$b_L^j(\mathbf{k}_{\mathbf{g}}) = e^{i\mathbf{k}_{\mathbf{g}} \cdot \mathbf{r}_j} (-1)^m Y_{l-m}(\mathbf{k}_{\mathbf{g}}), \quad (5.101)$$

$$c_L^j(\mathbf{k}_{\mathbf{g}}) = \sum_{L'} \tau_{LL'}^j(\mathbf{k}_{\mathbf{g}}) b_{L'}^j(\mathbf{k}_{\mathbf{g}}). \quad (5.102)$$

The matrices $\mathbf{T}^j(\mathbf{k}_{\mathbf{g}})$ need not be calculated explicitly; similar to Eq. (5.76), we solve the matrix equation of Eq. (5.99) for vectors $\mathbf{Z}^j(\mathbf{k}_{\mathbf{g}})$:

$$\begin{aligned} Z_{lm}^j(\mathbf{k}_{\mathbf{g}}) &= \sum_{l'm'} \tau_{lm,l'm'}^j(\mathbf{k}_{\mathbf{g}}) b_{l'm'}^j(\mathbf{k}_{\mathbf{g}}) + \sum_{l''m''} \tau_{lm,l''m''}^j(\mathbf{k}_{\mathbf{g}}) \sum_{l'm'} \sum_{\mu=1, \mu \neq j}^N G_{l''m'',l'm'}^{j\mu}(\mathbf{k}_0) Z_{l'm'}^\mu(\mathbf{k}_{\mathbf{g}}) \\ &= c_L^j(\mathbf{k}_{\mathbf{g}}) + \sum_{L''} \tau_{LL''}^j(\mathbf{k}_{\mathbf{g}}) \sum_{L'} \sum_{\mu=1, \mu \neq j}^N G_{L''L'}^{j\mu}(\mathbf{k}_0) Z_{L'}^\mu(\mathbf{k}_{\mathbf{g}}) \\ &= \sum_{L''} \tau_{LL''}^j(\mathbf{k}_{\mathbf{g}}) \sum_{L'} \sum_{\mu=1, \mu \neq j}^N \left[(1-X)^{-1} \right]_{L''L'}^{j\mu} b_{L'}^\mu(\mathbf{k}_{\mathbf{g}}). \end{aligned} \quad (5.103)$$

The vectors $\mathbf{Z}^j(\mathbf{k}_{\mathbf{g}})$ are now defined in terms of the subplane scattering matrices τ instead of atomic \mathbf{t}^j matrices, as in Eq. (5.76). The solution vectors $\mathbf{Z}^j(\mathbf{k}_{\mathbf{g}})$ can be written as:

$$Z_L^j(\mathbf{k}_{\mathbf{g}}) = \sum_{L'} T_{LL'}^j(\mathbf{k}_{\mathbf{g}}) b_{L'}^j(\mathbf{k}_{\mathbf{g}}). \quad (5.104)$$

The scattering amplitudes are then obtained as:

$$M_{\mathbf{g}'\mathbf{g}}^{\pm\pm} = -\frac{16\pi^2 i m_e}{A k_z^+ \hbar^2} \sum_L \sum_j a_L^j(\mathbf{k}_{\mathbf{g}}^\pm) Z_L^j(\mathbf{k}_{\mathbf{g}}^\pm) + \delta_{\mathbf{g}'\mathbf{g}} \delta_{\pm\pm}. \quad (5.105)$$

We can now shift the whole subplane by $\delta\mathbf{r}$ and calculate the change in $M_{\mathbf{g}'\mathbf{g}}$:

$$\delta M_{\mathbf{g}'\mathbf{g}}^{\pm\pm} = -\frac{16\pi^2 i m_e}{A k_z^+ \hbar^2} \sum_L \sum_j a_L^j(\mathbf{k}_{\mathbf{g}}^\pm) Z_L^j(\mathbf{k}_{\mathbf{g}}^\pm) - M_{\mathbf{g}'\mathbf{g}}^{\pm\pm}. \quad (5.106)$$

In Eq. (5.106) $\mathbf{a}^j(\mathbf{k}_{\mathbf{g}})$ and $\mathbf{Z}^j(\mathbf{k}_{\mathbf{g}})$ are vectors for the shifted structure, while in Eq. (5.105) $\mathbf{a}^j(\mathbf{k}_{\mathbf{g}})$ and $\mathbf{Z}^j(\mathbf{k}_{\mathbf{g}})$ are for the reference structure. With layer doubling or the RFS scheme we have only one incident beam \mathbf{k}_0 . At normal incidence the new vector \mathbf{Z}^j is then calculated from:

$$Z_L^j(\mathbf{k}_0) = c_L^j(\mathbf{k}_0) + \left[Z_L^{0j}(\mathbf{k}_0) - c_L^{0j}(\mathbf{k}_0) \right] e^{i\mathbf{k}_{0z} \delta \mathbf{r}_z}. \quad (5.107)$$

The quantities $\mathbf{a}^j(\mathbf{k}_{\mathbf{g}})$, $\mathbf{c}^j(\mathbf{k}_0)$ and $\mathbf{Z}^j(\mathbf{k}_{\mathbf{g}})$ must be recalculated for each new structure. The method is illustrated in Figure 5.18.

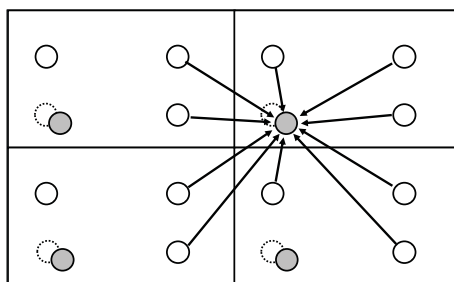


Figure 5.18 Illustration of the frozen LEED approximation. Shown is a section of the plane with four unit cells. One of the four atoms in the unit cell is shifted together with the translationally equivalent ones, that is, the whole periodic subplane is shifted. The wave field from the surrounding atoms remains unchanged but is transported to the shifted subplane positions. This is possible because the subplane has been extracted from the matrix to be inverted, see Eq. (5.99). For the wave field the plane wave expansion is used, in contrast to tensor LEED where the spherical wave expansion is used.

When the method is applied to one composite layer which must be combined with other layers using layer doubling or related methods, then all beams of the whole set of diffracted beams appear as incident beams and $\mathbf{Z}'^j(\mathbf{k}_g)$ must be calculated and stored for all beams. The calculation of new \mathbf{a}^{ij} , \mathbf{c}^{ij} and \mathbf{Z}^{ij} does not cause any problems.

Symmetries can be used by summation over symmetry equivalent beams in Eqs. (5.100–5.102). Symmetry in angular momentum components can be used as outlined in Section 5.3. The method is very fast and does not require much storage space when the whole surface slab is treated as a single layer. In the case of layer stacking, the required space is multiplied by the number of beams; therefore, the required space for storage can become very large.

5.4.3 Diffuse LEED for Disordered Surfaces

Disorder causes diffuse diffraction into all directions. In general, this applies to structures without long-range order, such as crystalline surfaces with randomly positioned defects (e.g., atomic vacancies or substitutions) or with irregularly placed adatoms or admolecules, which will be discussed in this section. Other candidates are randomly oriented or spinning molecules and disordered steps on a crystalline surface, as well as amorphous materials: such cases have not been addressed so far with diffuse LEED. The special case of finite particles is treated in Section 5.2.4. On the other hand, ideal quasicrystals (see Section 6.2) and modulated structures (see Section 6.3) have sufficient long-range order to prevent diffuse diffraction.

We here discuss the case of lattice gas disorder of adsorbates on crystalline surfaces, first proposed by J. B. Pendry and D. K. Saldin [5.39]. In this situation, adsorbates randomly occupy identical sites on the periodic substrate surface, while themselves lacking 2-D periodicity. Because the local electron scattering is very similar to the periodic case, the diffuse LEED (DLEED) intensity contains the same

local structural information as conventional LEED for ordered overlayers, namely adsorption site, bond lengths, etc. It must be noted that the diffuse intensity also contains contributions from any other defects, such as scattering from vacancies, disordered steps, impurities and phonons: extracting adsorbate structure therefore requires good sample preparation and low temperatures.

We shall in this section briefly review the experimental and theoretical approaches to extract the local structural information of disordered adsorbates. Reviews were published by M. A. Van Hove [5.40] and U. Starke et al. [5.41]. DLEED for other forms of disorder, such as vacancies and impurities, has not yet been fully developed, but may use similar methods, as supported by a study of disordered Pd substitution in the outermost layer of Cu(100) [5.42].

In the presence of an overlayer with lattice gas disorder, the substrate continues to produce a (1×1) diffraction pattern. In fact, the integer-order (1×1) spots also contain useful structural information about the adsorbate, as has been shown for methanol on Pd(111) [5.43].

DLEED intensities between (1×1) spots provide additional data but are inherently weak compared to the spot intensities [5.44]. A high-sensitivity 'digital LEED' detector using a wedge-and-strip anode was specifically developed to measure weak DLEED intensities [5.45]. Furthermore, disorder is not the only cause of diffuse diffraction. Another source is thermal diffuse scattering due to phonons, including molecular vibrations. Disorder and phonons may contribute similar amounts; the thermal diffuse scattering can easily exceed the scattering due to disorder, especially if the adsorbate density is low. Since thermal diffuse scattering is mostly caused by the substrate in the case of adsorbates on solid surfaces [5.46], it is customary to subtract the diffuse scattering due to the clean surface from that due to the adsorbate-covered surface. Such subtraction can also help reduce the effect of impurities and defects such as steps and vacancies, assuming that their presence and structure are not much modified by adsorption.

Diffuse LEED intensities were initially measured as angular maps at a few fixed energies. However, the polar and azimuthal angular dependence of DLEED intensities also depends on any 2-D correlation within the disordered adsorbate layer through an autocorrelation function; some correlation must be expected, as a sufficient density of adsorbates is needed for the DLEED measurement and mutual repulsion between adsorbates then causes a degree of local ordering. To remove such correlation effects, one can measure DLEED intensities $I(E)$ at pairs of nearby energies E (e.g., 4 eV apart) and take the logarithmic derivative with respect to energy: $L = (\partial I / \partial E) / I$. In practice, one normally uses the function $Y = L / (1 + V_{0i}^2 L^2)$ to avoid singularities in L (here V_{0i} is the imaginary part of the inner potential; a corresponding R-factor was devised for angular Y maps [5.39]; the same function Y is also used in defining the Pendry R-factor for $I(V)$ curves, see Section 6.1.2) [5.47].

More recently, diffuse LEED intensities have been measured as a function of energy in a way similar to $I(V)$ curves for spots [5.41; 5.43]: then the abovementioned autocorrelation function is independent of energy and can be ignored. This requires tracking diffuse intensity at constant parallel momentum transfer, as if tracking spots

(such tracking can be done by pre-recording spot movements for an ordered structure, or by interpolation between the positions of substrate-induced integer-order spots which are always present).

The theory of diffuse LEED was developed based on the concept that the electronic inelastic mean free path limits the distance that electrons travel within the surface. In the case of disordered adsorbate layers, individual electrons are not likely to scatter from a second adsorbate after scattering from a first adsorbate; this is especially true near normal incidence, where scattering by 90° from the incident direction toward a second adsorbate is unlikely, due to the angular dependence of typical atomic scattering factors. Therefore, in DLEED theory one may assume the limit of large inter-adsorbate distances, that is, low adsorbate density: the problem is thereby reduced to that of a single adsorbate on a crystalline substrate. This assumption is supported by experimental and theoretical LEED results for O adsorbates on Ni(100) [5.41] and Pd substitutions in Cu(100) [5.42], which show that the structure of diffuse or fractional-order $I(V)$ curves depends little on adatom density (apart from an overall intensity increase with density).

With a single adsorbate, the electron scattering can be subdivided into three steps, as shown in Figure 5.19(a) [5.39; 5.41; 5.47]. Step 1 follows the incident beam \mathbf{k}_{in} and its diffraction by the substrate until the electrons reach the adsorbate. In this process, the electrons can follow any possible path, including a direct approach to the adsorbate and all paths diffracted by the (1×1) substrate lattice, that is, all integer-order beams $\mathbf{k}_{\text{in}} + \mathbf{g}_{1 \times 1}$. Step 2 follows the electrons as they *first* scatter from the adsorbate until they *last* scatter from the adsorbate: this includes direct scattering by the adsorbate and all possible paths from the adsorbate to the substrate and back to the same adsorbate; this also includes all multiple scattering within the adsorbate alone and within the substrate alone, as well as single and multiple scattering by the substrate back to the adsorbate. Step 3 takes the electrons that leave the adsorbate for the last time and follows them to the detector. For step 3, we must realise that the outgoing electrons will be detected in one specific direction \mathbf{k}_{out} determined by the detector location. If we then backtrack from the detector to the adsorbate, we have a set of possible paths that are directly analogous to those in step 1, but with reversed direction. This implies, in the forward direction, following the direct path from adsorbate to detector and all integer-order beams $\mathbf{k}_{\text{out}} + \mathbf{g}_{1 \times 1}$ within the (1×1) substrate.

In this scheme, steps 1 and 3 are familiar multiple scattering processes in LEED from ordered surfaces, efficiently done with plane waves, as described in Section 5.2.6. Step 2 is better handled as a cluster problem with spherical waves, as described in Section 5.2.3.

The preceding theoretical model of DLEED is exact in the limit of a low adsorbate density. Its most time-consuming part is step 2, which is best calculated with spherical waves. Fortunately, most of the scattering in step 2 is relatively weak. The strongest scattering in step 2 is normally the direct scattering of the incident beam by the adsorbate to the detector: this cannot be neglected and may include strong intramolecular multiple scattering. All other scattering paths in step 2 involving the substrate are of third or higher order in terms of multiple scattering: for instance, an

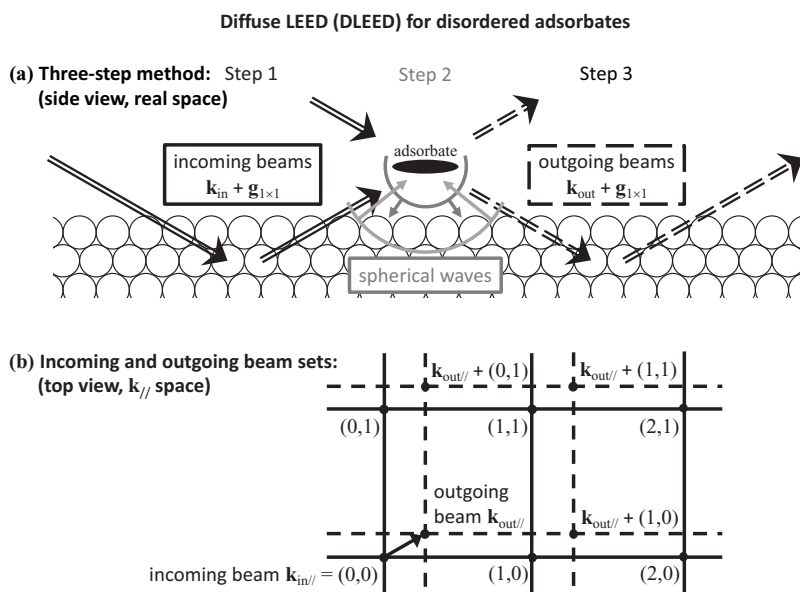


Figure 5.19 Multiple scattering model for diffuse LEED from a disordered adsorbate layer on a crystalline substrate: (a) three-step model; (b) relevant beam sets

electron could follow the third order path from adsorbate to substrate to adsorbate, or more complex paths. This suggests neglecting in step 2 all but the direct scattering by the adsorbate (which is very simple for an atomic adsorbate, and still allows including multiple scattering within the adsorbate if it is multi-atomic like a molecule, for example as a composite layer, cf. Section 5.2.5.4): calculations show this to be a very good approximation [5.40; 5.41]. This approximation is also computationally very beneficial: the single adsorbate can now be treated as a conventional layer with scattering matrices between the two beam sets $\mathbf{k}_{\text{in}} + \mathbf{g}_{1 \times 1}$ and $\mathbf{k}_{\text{out}} + \mathbf{g}_{1 \times 1}$. (As seen in Eqs. (5.28) and (5.35), such scattering matrices contain a pre-factor $1/A$ that specifies the density of scatterers in the layer; for DLEED that factor can be selected to match the actual density of the disordered layer.) These two beam sets are shown in 2-D reciprocal space in Figure 5.19(b): the outgoing set $\mathbf{k}_{\text{out}} + \mathbf{g}_{1 \times 1}$ is simply a shifted copy of the incoming set $\mathbf{k}_{\text{in}} + \mathbf{g}_{1 \times 1}$.

The above argument leads to a simple model: perform a conventional LEED calculation based on plane waves, using just the two plane-wave sets $\mathbf{k}_{\text{in}} + \mathbf{g}_{1 \times 1}$ and $\mathbf{k}_{\text{out}} + \mathbf{g}_{1 \times 1}$, with a conventional layer (of appropriate density) for the adsorbate. (This is an example of the application of the beam set neglect method of calculating LEED intensities [5.40; 5.48].)

A further simplification is possible: if \mathbf{k}_{out} is a fractional-order beam of the substrate, then standard LEED codes can be used virtually unchanged for DLEED by assuming a fictitious superlattice [5.40; 5.47]. For example, if \mathbf{k}_{out} corresponds to a (0.5, 0.5) or (0.25, 0.25) beam relative to the substrate's (1×1) pattern, then a standard LEED code can be applied by using a fictitious $c(2 \times 2)$ or $p(2 \times 2)$ superlattice. This

approach was used, for example, to successfully study the disordered substitutional adsorption of Pd in the outermost layer of Cu(100) [5.42].

DLEED can also be viewed as an electron hologram, and this technique is described in Section 6.1.1.2 (see also [5.49–5.54], and for positrons instead of electrons see [5.55]).

DLEED was first used to determine the structure of disordered O on W(100) [5.56]: O was found to adsorb in hollow sites; a later refinement (using tensor LEED combined with DLEED) found lateral W relaxations towards the O position [5.57]. DLEED was subsequently applied to study the initial stages of adsorption and the changes in adsorption site or bond lengths with increasing coverage for O and S on Ni(100) [5.58], Cl on Ti(0001) [5.59; 5.60], K on Co(10-10) [5.61] and K on Ni(100) [5.62]. Partial occupation of hcp and fcc sites of NO was found on Ni(111) [5.63], and for I on Rh(111) (also using tensor LEED) [5.64]. The early stages of surface alloy formation have been studied for Pd/Cu(100) [5.42]. A detailed analysis of the short-range order with mixed adsorption sites and comparison with full dynamic LEED calculations was performed for O on Ni(111) [5.65]. The DLEED calculation has been extended to spin dependent scattering and applied to CO on Pt(111) [5.66; 5.67], where the incoherent magnetic asymmetry parameters proved to be very sensitive to the adsorbate-substrate distance [5.68]. Molecular adsorption has been studied with DLEED in cases where no ordered structures could be obtained: Pt(111) + C₆H₆ [5.69], Pt(111) + C₂H₄ [5.70], Pt(111) + H₂O [5.71; 5.72], and methanol on Pd(111) [5.43].

5.5 Thermal Effects

Vibration amplitudes at surfaces are usually assumed to be larger than in the bulk [5.73]. There is also evidence that the vibration of surface atoms exhibits enhanced anisotropic and anharmonic effects. A detailed knowledge of the anisotropy and anharmonicity of thermal vibrations at surfaces would allow a better understanding of numerous surface properties like phase transitions, surface reconstructions, adsorption and desorption phenomena and growth processes. LEED studies of thermal vibrations on surfaces are rare, even though the surface sensitivity should make LEED an appropriate tool to study these effects. The reasons are experimental errors due to the influence of defects and the difficult analysis due to the multiple scattering. Both difficulties could be overcome in principle. The experimental control afforded by STM, AFM or SPA-LEED allows in many cases the preparation of very well ordered surfaces with low defect density; also the LEED programs could be developed further, such that a non-expert could analyse the data, as is the case, for example, with X-ray diffraction.

In the X-ray diffraction literature, the expression ‘thermal vibration’ is normally not used in connection with the analysis of diffraction data because the effects of static displacements (defects) and dynamic displacements (vibrations) cannot be distinguished experimentally. It has therefore been proposed to use the term ‘atomic displacement parameter’ (ADP) [5.74] and that has become the common terminology. The term ‘Debye–Waller factor’ is also commonly used. The determination of the

thermal contribution to the displacement parameter usually requires temperature-dependent measurements. Neutron diffraction measurements, where energy resolution allows the measurement of phonons, are in general more reliable than X-ray data. Electron diffraction has the same drawback as X-ray diffraction: static and dynamic displacements cannot be distinguished.

In most LEED surface structure analyses a Debye temperature is used which assumes isotropic displacements. The fitting of Debye temperatures to experimental $I(V)$ curves cannot be considered adequate for determining vibration amplitudes, unless careful temperature dependent measurements are made and the static contribution can be separated. The expression 'atomic displacement parameter' or ADP is therefore used in the following and includes both static and dynamic contributions. The more common expression 'thermal vibration' is nevertheless also used in connection with temperature-dependent measurements.

The main experimental method to investigate thermal vibration at surfaces is high-resolution electron energy loss spectroscopy (HREELS) [5.75], which allows measuring the frequencies of surface vibrations. In structure analyses with diffraction techniques it is the amplitudes of the vibrational displacements that are measured. Vibrational frequencies and amplitudes are related and it would be useful to combine and compare results from LEED and HREELS, but this is rarely done. The vibration amplitudes play an important role in structure determination. With both LEED and X-ray diffraction, a high accuracy of the structural parameters can only be reached by including atomic displacement parameters in the structure refinement procedure. For example, LEED $I(V)$ analyses of coadsorbed CO and oxygen on Ru(0001) led to a substantial improvement of the fit of the experimental data when anisotropic vibrations were included [5.76]. A further reason to study vibration amplitudes with diffraction methods is the access it provides to understanding molecular motion and diffusion paths at surfaces. With X-ray diffraction, an anharmonic motion of Cs adsorbed on Cu(100) has been determined [5.77]. Although this has not yet been done with LEED, the method is certainly capable of studying anharmonic motion: it is a promising future application for LEED.

LEED is sensitive enough to determine anisotropic displacement parameters even at clean metal surfaces; an example for Cu(110) is shown in Section 5.5.8. This should also be possible in adsorbate layers. The point of interest is the thermally induced change of bond lengths in the adsorbed state and the interaction with the substrate. Here the temperature dependence and the anisotropy of the thermal parameters play an important role. In many cases details should become observable by LEED studies which would be difficult to detect with other methods. Nevertheless, a combination of two or more methods is in any case advantageous to reach a conclusive interpretation of the results.

5.5.1 Thermal Vibration in the Kinematic Theory of Diffraction

We here briefly reiterate the treatment of thermal vibrations in the kinematic theory in order to elucidate the approximations made in the case of multiple scattering.

A detailed description of the kinematic theory can be found in B. T. M. Willis and A. W. Pryor [5.78], while a review of theoretical and experimental methods to analyse atomic displacements has been given by F. W. Kuhs [5.74]. The commonly used atomic displacement parameters have been described by K. N. Trueblood et al. [5.79]. In the kinematic theory the diffracted intensity is given by

$$I(\mathbf{q}) = \sum_{i,j} f_i(\mathbf{q}) \cdot f_j^*(\mathbf{q}) \cdot e^{i\mathbf{q}(\mathbf{r}_i - \mathbf{r}_j)} \langle e^{i\mathbf{q}(\mathbf{u}_i - \mathbf{u}_j)} \rangle, \quad (5.108)$$

where \mathbf{r}_i , \mathbf{r}_j are the equilibrium positions of atoms i and j , the sum is taken over all atoms of the crystal, \mathbf{u}_i and \mathbf{u}_j are the corresponding displacements at a given time, $\mathbf{q} = \mathbf{k}' - \mathbf{k}$ is the scattering vector and $f_i(\mathbf{q})$ are the atomic scattering factors. The pointed brackets denote the average over time. In this description the displacements include static displacements due to defects like vacancies, interstitial atoms, etc., as well as thermal vibrations. Assuming a Gaussian distribution of displacements \mathbf{u}_i and \mathbf{u}_j , the average is given by:

$$\begin{aligned} \langle \exp [i\mathbf{q} \cdot (\mathbf{u}_i - \mathbf{u}_j)] \rangle &= \exp \left\{ -\frac{1}{2} \langle [\mathbf{q} \cdot (\mathbf{u}_i - \mathbf{u}_j)]^2 \rangle \right\} \\ &= \exp \left\{ -\frac{1}{2} \left[\langle (\mathbf{q} \cdot \mathbf{u}_i)^2 \rangle + \langle (\mathbf{q} \cdot \mathbf{u}_j)^2 \rangle + \langle (\mathbf{q} \cdot \mathbf{u}_i)(\mathbf{q} \cdot \mathbf{u}_j) \rangle \right] \right\}. \end{aligned} \quad (5.109)$$

It should be pointed out here that the assumption of a Gaussian distribution is an approximation, which is not justified in all cases, certainly not for static displacements around defects where the displacement depends on the distance from the defect [5.80]. A better description of the distribution may be even more important for LEED because, due to multiple scattering, resonances may occur along the scattering paths between nearest neighbours. For the same reason, a more detailed description of correlated motion should be included. Nevertheless, we here use this approximation of a Gaussian distribution to derive the expression for the kinematic Debye–Waller factor. In the following, we may assume for simplicity that all atoms are equal and then obtain for the average:

$$\langle (\mathbf{q} \cdot \mathbf{u}_i)^2 \rangle = \langle (\mathbf{q} \cdot \mathbf{u}_j)^2 \rangle = \langle (\mathbf{q} \cdot \mathbf{u})^2 \rangle. \quad (5.110)$$

The intensity can be written in a form that yields a first-order term and higher-order terms:

$$I(\mathbf{q}) \propto |f(\mathbf{q})|^2 \sum_{ij} e^{i\mathbf{q}(\mathbf{r}_i - \mathbf{r}_j)} e^{-\langle (\mathbf{q} \cdot \mathbf{u})^2 \rangle} \cdot \{1 + \langle (\mathbf{q} \cdot \mathbf{u}_i)(\mathbf{q} \cdot \mathbf{u}_j) \rangle + \dots\}. \quad (5.111)$$

The first term in Eq. (5.111) is a sharp but weakened reflection I_{Bragg} , while the second and higher order terms constitute the thermal diffuse scattering (TDS) I_{TDS} :

$$I = I_{\text{Bragg}} + I_{\text{TDS}}.$$

The atomic displacements result in a reduction of the elastically scattered Bragg intensity by a factor $\exp(-2M)$:

$$\begin{aligned} I_{\text{Bragg}} &= |F(\mathbf{q})|^2 |T(\mathbf{q})|^2 \delta(\mathbf{q} - \mathbf{g}) \\ &= |F(\mathbf{q})|^2 \exp(-2M) \delta(\mathbf{q} - \mathbf{g}). \end{aligned} \quad (5.112)$$

Here \mathbf{g} is a vector of the 2-D reciprocal net and

$$M = \frac{1}{2} \langle (\mathbf{q} \cdot \mathbf{u})^2 \rangle. \quad (5.113)$$

The intensity that is missing from the Bragg peak is the thermal diffuse scattering. Correlated displacements occurring in the term $\langle (\mathbf{q} \cdot \mathbf{u}_i) (\mathbf{q} \cdot \mathbf{u}_j) \rangle$ in Eq. (5.111) cause the one-phonon peak at the Bragg energies, while uncorrelated displacements lead to a constant background distributed over all directions. Although the TDS cannot be neglected in LEED experiments, its treatment in the multiple scattering theory has not been solved. Experimentally it has been found that the one-phonon part is distributed as $1/q$ away from the Bragg peaks, while the multiphonon part is more equally distributed in reciprocal space, corresponding to the result of the kinematic theory. Experimental studies of the TDS in LEED are rare. The first measurements were made in the early days of LEED by M. B. Webb and coworkers [5.81]. In later investigations by M. Henzler and coworkers using a SPA-LEED system with high energy and angle resolution, the single- and multi-phonon parts could be separated [5.82]. It was found that kinematic description of the one-phonon peak which causes a Lorentzian foot of the Bragg peak is also valid for LEED. No indication of multiple scattering effects in the beam profile were found. In LEED systems with lower resolution the one-phonon peak is usually included in beam profile and $I(V)$ measurements. As the intensity of the TDS follows the Bragg intensity, only small influences on the analysis of the beam profiles or $I(V)$ curves can be expected. Also, in X-ray diffraction the TDS is usually neglected; the multiple scattering theory described in Section 5.5.3 neglects the TDS as well.

In the following, only the Bragg intensity is described. We first mention that the conventional derivation of the Debye–Waller factor is obtained when the average of the left-hand side of Eq. (5.109) is calculated from the distribution of atomic displacements, namely the probability density function (PDF) $p(\mathbf{u})$. The Debye–Waller factor $T(\mathbf{q})$ is given as the Fourier transform of the PDF:

$$T(\mathbf{q}) = \int p(\mathbf{u}) \exp(i\mathbf{q} \cdot \mathbf{u}) d\mathbf{u}, \quad (5.114)$$

which is equivalent to

$$T(\mathbf{q}) = \exp\left(-\frac{1}{2} q^2 \langle u^2 \rangle\right), \quad (5.115)$$

if the PDF is a Gaussian distribution; the PDF in general can be different from a Gaussian distribution. When the Debye–Waller factor is experimentally determined,

the corresponding PDF is obtained by the reverse Fourier transform of the Debye–Waller factor:

$$p(\mathbf{u}) = (2\pi)^{-3} \int T(\mathbf{q}) \exp(-i\mathbf{q} \cdot \mathbf{u}) d\mathbf{q}. \quad (5.116)$$

5.5.2 Thermal Parameters

The atomic displacement parameter (ADP) enters the intensity calculations in one of several possible forms. In X-ray structure analysis for *isotropic* displacements, usually the so-called B-factor is used, which is defined as $B = 8\pi^2 \langle u^2 \rangle$. B is frequently called the temperature factor, although it is well known that the displacements include defects and lattice distortions around defects; u is the mean square displacement from the equilibrium position, given in nm or Å when q is given in nm⁻¹ or Å⁻¹, respectively. In the case of isotropic displacements, u is the radius of the spherically symmetric PDF. It is usually defined as the radius where the integral of the probability density reaches ½. The Debye–Waller factor is a function of the mean square of the scalar product $\mathbf{q} \cdot \mathbf{u}$:

$$\langle (\mathbf{q} \cdot \mathbf{u})^2 \rangle = \langle (q_x u_x)^2 \rangle + \langle (q_y u_y)^2 \rangle + \langle (q_z u_z)^2 \rangle = \frac{3}{2} |q|^2 |u|^2, \quad (5.117)$$

where u is the radius of the probability density sphere; the B-factor uses the mean square value $\langle u^2 \rangle = 3/2 |u|^2$, independent of lattice and orientation of the diffraction vector.

For *anisotropic* atomic displacement parameters (ADPs), the average of the mean square of $\mathbf{q} \cdot \mathbf{u}$ depends on the diffraction vector. Six independent parameters are used to describe the ellipsoid of the probability density assuming a Gaussian distribution of the displacements. Frequently used are β_{kl} with $k, l = 1, 2, 3$. The quantities β_{kl} represent a symmetric quadratic form with six parameters $\beta_{11}, \beta_{22}, \beta_{33}$ and $2\beta_{12}, 2\beta_{13}, 2\beta_{23}$, which can be used to describe an ellipsoid. The lengths of the semi-axes of the ellipsoid cannot be directly determined from the parameters β_{11}, β_{22} and β_{33} ; the determination of the size and orientation of the thermal ellipsoid from the β_{kl} is described in Appendix I. In X-ray diffraction the parameters are usually related to the lattice vectors, which in general form a non-orthonormal coordinate system. The parameters β_{kl} are dimensionless and are related to the lengths of the lattice vectors. To compare the values to the isotropic case a transformation to absolute values in nm² or Å² is required. There are symmetry restrictions on the parameters, for special positions in the unit cell; the orientation of the ellipsoid and their semi-axes have to be consistent with the site symmetry.

Another set of six parameters, usually called U_{kl} , is also frequently used. They are also related to the translation lattice but are not dimensionless. The use of U_{kl} instead of β_{kl} has the advantage that U_{11}, U_{22} and U_{33} give directly the semi-axis sizes of the ellipsoid in nm² or Å² and can be compared with the values obtained with the assumption of isotropic displacements. For the definition of U_{kl} , see Appendix I.

By contrast, in LEED calculations it is common to use not the displacement parameter u but the Debye temperature Θ_D . In the high temperature limit the relation to the displacement parameter is given by:

$$\langle u^2 \rangle = \frac{3\hbar^2 T}{2m_a k_B \Theta_D^2}, \quad (5.118)$$

with m_a the mass of the atom and k_B the Boltzmann constant. Through this relation, the Debye temperature gives the mean square displacement as a function of temperature: it has the advantage that only one parameter is needed in temperature dependent measurements. The Debye temperature has been derived theoretically in the Debye model mainly for mono-atomic structures: in practice, the Debye model is not used for compounds. In LEED studies of compounds (including adsorption of foreign elements, for example), one may optimise Debye temperatures for different constituent elements or atoms in inequivalent positions, for example, in different layers, at a fixed temperature: this then corresponds to the determination of separate isotropic mean square displacement parameters for the different elements or inequivalent atoms and is not related to the Debye model.

In analogy to X-ray diffraction, there have been early attempts in LEED studies to derive an average temperature factor from the decrease of the intensity with increasing energy. However, this approach has not been successful in LEED and leads to different factors depending on which diffracted beam was used. It is not possible in general to derive an overall temperature factor from LEED I(V) curves, due to multiple scattering effects. In X-ray diffraction an overall temperature factor is used for the normalisation of structure factors in direct methods, but not in structure refinement.

5.5.3 Harmonic Vibrations

The distribution of atomic displacements is described by the probability density function (PDF), $p(u)$. For harmonic vibrations in the high temperature limit it can be assumed to be a Gaussian distribution. First, we consider isotropic displacements. The distribution is then defined by a single parameter, the mean square displacement $\langle u^2 \rangle$:

$$p(u) = \frac{1}{(2\pi)^{3/2} \langle u^2 \rangle^{1/2}} \exp\left(-\frac{u^2}{2\langle u^2 \rangle}\right). \quad (5.119)$$

The atomic Debye–Waller factor is given by the Fourier transform of the PDF,

$$T(q) = \exp\left(-\frac{1}{2} q^2 \cdot \langle u^2 \rangle\right), \quad (5.120)$$

and is independent of the crystal system and of the direction of the scattering vector \mathbf{q} , but strongly dependent on the scattering angle.

In the case of anisotropic vibrations, assuming mean square displacements $\langle u_x^2 \rangle, \langle u_y^2 \rangle, \langle u_z^2 \rangle$ in three orthogonal directions, the atomic Debye–Waller factor is given by

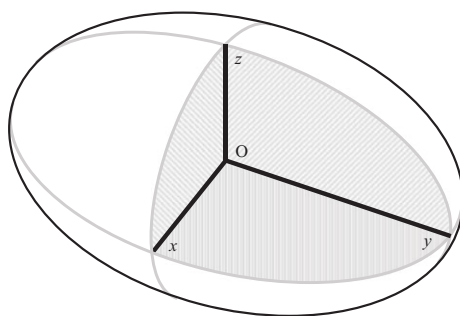


Figure 5.20 Ellipsoid of the probability density. The semi-axis lengths Ox , Oy and Oz are usually chosen such that the atom has 50% probability of being inside the ellipsoid; the semi-axis lengths are proportional to the respective mean square displacements.

$$T(\mathbf{q}) = \exp\left(-\frac{1}{2} \cdot \mathbf{q}^T \langle \mathbf{u}^T \mathbf{u} \rangle \mathbf{q}\right), \quad (5.121)$$

using the conventional crystallographic formulation, where \mathbf{u}^T denotes the transpose of vector \mathbf{u} . The probability density function is then given by

$$p(\mathbf{u}) = \left(\frac{\det \mathbf{B}^{-1}}{8\pi^3}\right)^{1/2} \exp\left(-\frac{1}{2} \mathbf{u}^T \mathbf{B}^{-1} \mathbf{u}\right), \quad (5.122)$$

with a symmetric matrix

$$\mathbf{B} = \begin{pmatrix} \langle u_x^2 \rangle & \langle u_x u_y \rangle & \langle u_x u_z \rangle \\ \langle u_x u_y \rangle & \langle u_y^2 \rangle & \langle u_y u_z \rangle \\ \langle u_x u_z \rangle & \langle u_y u_z \rangle & \langle u_z^2 \rangle \end{pmatrix}. \quad (5.123)$$

The exponent $\mathbf{u}^T \mathbf{B}^{-1} \mathbf{u}$ is a quadratic function of the atomic displacements, so that $\mathbf{u}^T \mathbf{B}^{-1} \mathbf{u} = \text{const.}$ defines an ellipsoid, cf. Figure 5.20. Conventionally the size of the ellipsoid is chosen such that the integral over its volume is 0.5. The six independent matrix elements describe the lengths of the semi-axes and the orientation of the ellipsoid. The mean square displacements u_x , u_y and u_z refer to an orthonormal coordinate system. The description in general oblique coordinate systems and the relation to the parameters β_{kl} mentioned in Section 5.5.2 are given in Appendix I.

5.5.4 Anharmonic Vibrations

In surface structure determinations by LEED, anharmonic thermal vibrations have received little attention. On the other hand, physical properties like thermal expansion, temperature dependence of elastic constants or adsorption and desorption kinetics can be explained only by anharmonic effects [5.83]. The influence of anharmonic corrections on the inter-atomic force constants on the adsorption kinetics has been

theoretically investigated [5.83]; experimental results, however, are rare [5.84]. It is therefore desirable to include anharmonic effects in the multiple scattering theory in addition to anisotropy, in the hope of gaining more insight into the anharmonicity of the inter-atomic forces from diffraction experiments. To that end, this section gives a brief overview of anharmonicity in materials, followed by a description of how anharmonic effects can be included in the multiple scattering LEED theory in Section 5.5.5.

We need to first discuss how anharmonicity can be handled within a single scattering theory of diffraction. There exist various possibilities to include anharmonic terms in the generalised Debye–Waller factor, both in the static contribution and in the dynamic contribution. In the single-scattering context of X-ray diffraction, methods have been reviewed by F. W. Kuhs [5.74] and a detailed description is given by B. T. M. Willis and A. W. Pryor [5.78]. One approach is the expansion of the Debye–Waller factor in moments:

$$\langle \exp(i \mathbf{q} \cdot \mathbf{u}) \rangle = \sum_{N=0}^{\infty} (1/N!) \langle (\mathbf{q} \cdot \mathbf{u})^N \rangle. \quad (5.124)$$

Another option is through cumulants where the series expansion appears in the exponent:

$$\langle \exp(i \mathbf{q} \cdot \mathbf{u}) \rangle = \exp \left(\sum_{N=0}^{\infty} (1/N!) \langle (\mathbf{q} \cdot \mathbf{u})^N \rangle_{cum} \right). \quad (5.125)$$

The cumulant expansion has the advantage that in the harmonic case all cumulants of order higher than 2 vanish, which enables identifying and separating anharmonic effects. Experiments on surfaces are rare; one example is the motion of Cs on Cu(001) determined by X-ray diffraction where the cumulant expansion was used [5.85].

The atomic displacements consist of two contributions: the static part arising from defects and the dynamic (thermal) part, both governed by the inter-atomic forces. The static part depends strongly on the defect concentration and the nature of the defects; there is no reason for the static displacements at defect sites to exhibit a Gaussian distribution, as has been pointed out by M. A. Krivoglaz [5.80]. The dynamic part is also affected by the static displacements near a defect site but the vibration amplitude is governed by the inter-atomic force constants which are usually calculated assuming a harmonic crystal potential. Calculations using a full crystal potential including all atomic interactions would be extremely complicated. As an approximation, anharmonic terms in the crystal potential mostly assume a one-particle potential $V(\mathbf{u})$, in which one particle is assumed to move in the fixed potential caused by the rigid lattice of surrounding atoms.

For a theoretical calculation of anharmonic lattice vibrations, the partition function of an atom in a one-particle potential $V(\mathbf{u})$ is required. The dynamic part of the Debye–Waller factor then becomes, at temperature T :

$$\langle \exp(i \mathbf{q} \cdot \mathbf{u}) \rangle = \frac{\int \exp(i \mathbf{q} \cdot \mathbf{u}) \exp(-V(\mathbf{u})/k_B T) d\mathbf{u}}{\int \exp(-V(\mathbf{u})/k_B T) d\mathbf{u}}. \quad (5.126)$$

The one particle potential is expanded in a Taylor series by atomic displacements:

$$\begin{aligned} V(\mathbf{u}) &= V_0 + V_1 + V_2 + V_3 + V_4 \dots \\ &= \text{const} + \sum_{\alpha, l} \left(\frac{dV}{d\mathbf{u}_{\alpha, l}} \right) \mathbf{u}_{\alpha, l} + \frac{1}{2!} \sum_{\alpha, l} \sum_{\alpha', l'} \left(\frac{dV}{d\mathbf{u}_{\alpha, l}} \right) \left(\frac{dV}{d\mathbf{u}_{\alpha', l'}} \right) \mathbf{u}_{\alpha, l} \mathbf{u}_{\alpha', l'} \\ &\quad + \frac{1}{3!} \sum_{\alpha, l} \sum_{\alpha', l'} \sum_{\alpha'', l''} \dots \end{aligned} \quad (5.127)$$

where $\alpha, \alpha', \alpha''$, etc. label the atoms and l, l', l'' , etc. label the unit cells. The derivatives are taken at the equilibrium position so that V_1 vanishes. $V(\mathbf{u}) = V_0 + V_2$ represents the harmonic approximation. The third and fourth order terms in the anharmonic expansion, Eq. (5.127), are usually considered to be sufficient for cases where a perturbation treatment is adequate. Higher order terms, of course, become important for larger displacements. The anharmonic terms are mainly dominated by the short-range repulsion between nearest neighbours.

The explicit calculation of the dynamic part of the Debye–Waller factor using the expansion in Eq. (5.127) is complicated and has been done only for simple crystal structures. Most evaluations of experimental results use an expansion of the displacements. This includes then also the static part of the Debye–Waller factor, but is of course not suited to draw a precise conclusion on the form of the inter-atomic pair potentials. The most convenient approach is the expansion of $\mathbf{q} \cdot \mathbf{u}$ by moments or cumulants, as described in Eqs. (5.124) and (5.125). The cumulant expansion is preferred as the harmonic and anharmonic terms can be separated [5.74]. Because effects are small, usually only the third and fourth order terms are included: the result then shows the difference from the harmonic approximation.

Anharmonicity also occurs in such special cases as libration and free rotation of molecules. Libration occurs when a cluster of atoms vibrates relatively rigidly against its surroundings, for example, when the internal displacements within a molecule or a part of a molecule are much smaller than the displacements of that atom cluster as a whole. The atomic displacements are then calculated as a function of the movement of a rigid body. For example, C_{60} molecules in some circumstances can rotate around an axis normal to a substrate surface. Such a movement cannot be treated as independent thermal motions of individual atoms. In X-ray diffraction, such cases can be handled with the kinematic theory, see for example [5.86].

In the case of LEED, the full multiple scattering theory for libration modes has not been worked out, while an approximation has been used to study the bending mode of CO on Ru(0001) [5.87]. In this study the bending mode of the CO molecule was simulated by coherent superposition of scattered waves from different inclined positions of the molecule, as illustrated in Figure 5.21.

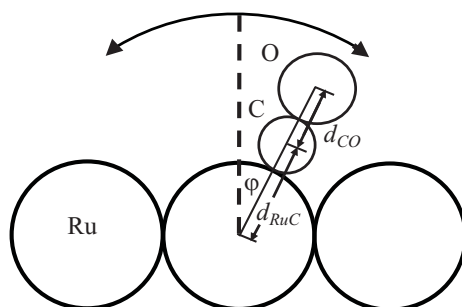


Figure 5.21 Example of a libration mode: the bending mode vibration of a CO molecule which is assumed to be internally rigid. Redrawn from [5.87] M. Gierer, H. Bludau, H. Over, and G. Ertl, *Surf. Sci.*, vol. 346, pp. 64–72, 1996, with permission from Elsevier.

5.5.5 Multiple Scattering Theory of Thermal Effects

In the multiple scattering theory, the diffracted intensity is formally described in the same way as in the kinematic theory by summing the scattering amplitudes of all atoms in the unit cell (see introductory remarks in Section 2.2.1 and Eq. (2.49)):

$$I(\mathbf{k}, \mathbf{k}') = \left| \sum_{\nu} F_{\nu}(\mathbf{k}, \mathbf{k}') e^{i(\mathbf{k}' - \mathbf{k}) \cdot \mathbf{d}_{\nu}} \right|^2. \quad (5.128)$$

The only difference is that atomic scattering factors $F_{\nu}(\mathbf{k}, \mathbf{k}')$ are now generalised scattering factors which represent all multiple scattering paths ending in atom ν (this form can also be seen in Eq. (5.17), where \mathbf{T}^i represents all multiple scattering paths ending in atom i); these scattering factors depend explicitly on the wave vectors \mathbf{k} and \mathbf{k}' , that is, on both the incoming and the diffracted beams. The generalised scattering factor depends also on the crystal structure surrounding that atom, in contrast to the kinematic theory where the atomic scattering factors are assumed to depend only on the scattering vector $\mathbf{q} = \mathbf{k}' - \mathbf{k}$ and are independent of the crystal structure. The generalised scattering factors are usually calculated in a spherical wave expansion as matrices \mathbf{T} and are given by Eq. (5.29), which is written here in slightly different form and without pre-factors:

$$F_{\nu}(\mathbf{k}, \mathbf{k}') = \sum_{lm, l'm'} (-1)^m Y_{l-m}(\vartheta_k, \varphi_k) T_{\nu, lm, l'm'}(\mathbf{k}) Y_{l'm'}(\vartheta_{k'}, \varphi_{k'}). \quad (5.129)$$

The matrices \mathbf{T} result from the solution of self-consistent equations which take into account the multiple scattering processes (see Eq. (5.29) and its derivation).

Introducing the atomic displacement \mathbf{u}_{ν} of atom ν , the average diffracted intensity is now given by:

$$I(\mathbf{k}, \mathbf{k}') = \left\langle \left| \sum_{\nu} F_{\nu}(\mathbf{k}, \mathbf{k}', \mathbf{u}_{\nu}) e^{i(\mathbf{k}' - \mathbf{k}) \cdot (\mathbf{d}_{\nu} + \mathbf{u}_{\nu})} \right|^2 \right\rangle_T. \quad (5.130)$$

Because of the multiple scattering, the generalised scattering factors themselves now depend on the displacements and therefore the average cannot be restricted to the phase factors. We neglect correlations and the thermal diffuse scattering and average the scattering amplitudes. This corresponds to the approximation made in the kinematic theory when only the first term of Eq. (5.111) is included. We obtain for the intensity of the Bragg scattering:

$$\begin{aligned} I(\mathbf{k}, \mathbf{k}') &= \left| \sum_{\nu} \langle F_{\nu}(\mathbf{k}, \mathbf{k}', \mathbf{u}_{\nu}) e^{i(\mathbf{k}' - \mathbf{k})(\mathbf{d}_{\nu} + \mathbf{u}_{\nu})} \rangle_T \right|^2 \\ &= \left| \sum_{\nu} \langle F_{\nu}(\mathbf{k}, \mathbf{k}') \rangle_T e^{i(\mathbf{k}' - \mathbf{k})\mathbf{d}_{\nu}} \right|^2, \end{aligned} \quad (5.131)$$

with thermally averaged scattering factors:

$$\langle F_{\nu}(\mathbf{k}, \mathbf{k}') \rangle_T = \sum_{lm, l'm'} (-1)^m Y_{l-m}(\Omega_k) \left\langle \sum_{\nu} T_{\nu}(\mathbf{k}, \mathbf{u}_{\nu}) e^{i(\mathbf{k}' - \mathbf{k})\mathbf{u}_{\nu}} \right\rangle_T Y_{l'm'}(\Omega_{k'}). \quad (5.132)$$

The average on the right-hand side of Eq. (5.132) can be defined as an averaged matrix \mathbf{T} . It was shown in [5.1; 5.88] that, in the harmonic approximation, the thermally averaged matrices \mathbf{T} are given by solving the multiple scattering equations using the thermally averaged single scattering matrices \mathbf{t} . Correlations between atomic displacements as well as correlations in the multiple scattering series are neglected here:

$$T_{\nu}(\mathbf{k}, \langle \mathbf{u}_{\nu} \rangle_T) = t_{\nu}(E, \langle \mathbf{u}_{\nu} \rangle_T) + t_{\nu}(E, \langle \mathbf{u}_{\nu} \rangle_T) \sum_{\mu \neq \nu} G_{\nu\mu}(\mathbf{k}, \mathbf{d}_{\mu} - \mathbf{d}_{\nu}) T_{\mu}(\mathbf{k}, \langle \mathbf{u}_{\mu} \rangle_T), \quad (5.133)$$

with

$$t_{\nu}(E, \langle \mathbf{u}_{\nu} \rangle_T) = t_{\nu}(E) \langle e^{i(\mathbf{k}' - \mathbf{k})\mathbf{u}_{\nu}} \rangle_T. \quad (5.134)$$

Equation (5.133) means that the multiple scattering equations are solved with the averaged atoms which are held immobile in a rigid but distorted lattice, thus excluding correlations in the thermal motion; in other words, the electron is scattered by spherically symmetric atomic potentials which are displaced by variable vectors \mathbf{u}_{ν} , causing a fluctuating phase factor that is averaged in Eq. (5.134). Deformation of the electron density or the potential is not considered. In the harmonic approximation and assuming a Gaussian PDF, the average in Eq. (5.134) can be replaced by

$$\langle e^{i(\mathbf{k}' - \mathbf{k})\mathbf{u}_{\nu}} \rangle_T = e^{-\frac{1}{2} \langle [(\mathbf{k}' - \mathbf{k})\mathbf{u}_{\nu}]^2 \rangle_T}. \quad (5.135)$$

This expression can be expanded in spherical harmonics, yielding diagonal matrices \mathbf{t} , the diagonal elements of which lead to complex temperature dependent phase shifts, resulting in Eq. (5.154) further below. This formulation makes the calculation of thermal effects especially easy.

If we want to introduce anisotropic and anharmonic vibrations, we can start from the PDF $p(\mathbf{u})$:

$$\langle e^{i(\mathbf{k}'-\mathbf{k})\cdot\mathbf{u}} \rangle_T = \int p(\mathbf{u}) \cdot e^{i(\mathbf{k}'-\mathbf{k})\cdot\mathbf{u}} d\mathbf{u}. \quad (5.136)$$

We can use a multipole expansion of the PDF:

$$p(\mathbf{u}) = \sum_{n=1}^{\infty} \sum_{l_c=0, m_c}^{l_c, \max} R_n(u) c_{n, l_c m_c} Y_{l_c m_c}(\vartheta_u, \varphi_u), \quad (5.137)$$

where $c_{n, l_c m_c}$ are appropriate multipole expansion coefficients and $R_n(u)$ radial functions of $u = |\mathbf{u}|$. In principle the sum over n is unlimited, but in practice only one or two radial functions are needed. Gaussian functions are used here to match the Gaussian shape of the thermal ellipsoid. It is necessary in practice to derive the expansion coefficients and radial functions from the mean square displacements in different directions assuming Gaussian distributions; otherwise an intractable number of fit parameters would remain in structure refinement [5.89–5.91]. The calculation procedure is described in Section 5.5.6, see also the detailed description in [5.92].

The multipole expansion of the PDF is not restricted to harmonic vibrations and allows the inclusion of anharmonic terms as well. This case requires special care to select the appropriate parameters; an example will be discussed in Section 5.5.7. The thermally averaged atomic scattering factor for single scattering is now given by:

$$t(T, \mathbf{k}, \mathbf{k}') = t(0, \mathbf{k}, \mathbf{k}') \int p(\mathbf{u}) e^{i(\mathbf{k}-\mathbf{k}')\cdot\mathbf{u}} d\mathbf{u}, \quad (5.138)$$

where the atomic scattering factor at temperature $T = 0$ is

$$t(0, \mathbf{k}, \mathbf{k}') = \frac{-2\pi i}{k} \sum_l (2l+1) e^{i\delta_l} \sin(\delta_l) P_l(\cos \vartheta_{kk'}), \quad (5.139)$$

and δ_l are the phase shifts. The scattering factors can be written as

$$t(0, \mathbf{k}, \mathbf{k}') = \frac{-8\pi^2}{k} \sum_{lm, l'm'} e^{i\delta_l} \sin(\delta_l) \delta_{ll'} \delta_{mm'} Y_{lm}(\vartheta_{k'}, \varphi_{k'}) Y_{l-m}(\vartheta_k, \varphi_k) (-1)^m, \quad (5.140)$$

and a spherical wave expansion can be used for the phase factors:

$$e^{i\mathbf{k}\cdot\mathbf{r}} = \sum_{lm} 4\pi i^l j_l(kr) Y_{lm}(\Omega_r) (-1)^m Y_{l-m}(\Omega_k). \quad (5.141)$$

Following the calculation for the isotropic case as given by J. B. Pendry [5.1] and using the same notation, we define expansion coefficients for the Fourier transform of the probability density function:

$$\int p(\mathbf{u}) e^{i(\mathbf{k}'-\mathbf{k})\cdot\mathbf{u}} d\mathbf{u} = \sum_{l_1, m_1} \sum_{l_2, m_2} W_{l_1 m_1, l_2 m_2} Y_{l_1 m_1}(\vartheta_k, \varphi_k) Y_{l_2 - m_2}(\vartheta_{k'}, \varphi_{k'}) (-1)^{m_2}. \quad (5.142)$$

After multiplying both sides with the spherical harmonics and integrating over the angles we obtain:

$$W_{LM,L'M'} = 16\pi^2 \sum_{n=1}^{\infty} \sum_{l_c m_c} B_{l_1 m_1, l_2 m_2, l_c m_c} C_{n, l_c m_c} \cdot \int R_n(u) (-1)^{l_1+l_2} j_{l_1}(ku) j_{l_2}(k'u) u^2 du. \quad (5.143)$$

We can now define temperature dependent expansion coefficients of the scattering factors:

$$t(T, \mathbf{k}, \mathbf{k}') = 8\pi^2 \sum_{lm} \sum_{l'm'} t_{lm,l'm'}(T) Y_{lm}(\Omega_k) (-1)^m Y_{l'-m'}(\Omega_{k'}), \quad (5.144)$$

with the coefficients of the angular momentum expansion

$$t_{lm,l'm'}(T) = \frac{1}{8\pi^2} \iint t(T, \mathbf{k}, \mathbf{k}') (-1)^m Y_{l-m}(\vartheta_k, \varphi_k) Y_{l'-m'}(\vartheta_{k'}, \varphi_{k'}) d\Omega_k d\Omega_{k'}, \quad (5.145)$$

where $d\Omega_k = \sin^2 \vartheta_k d\vartheta_k d\phi_k$ and similarly for $d\Omega_{k'}$. Inserting Eq. (5.142) into Eq. (5.138) and using the expansions in Eqs. (5.141) and (5.144), we obtain

$$t_{lm,l'm'}(T) = \sum_{l_1 m_1} \sum_{l_2 m_2} W_{l_1 m_1, l_2 m_2} D_{l_1 m_1, l_2 m_2, lm, l'm'}, \quad (5.146)$$

where

$$D_{l_1 m_1, l_2 m_2, lm, l'm'} = \frac{2\pi}{k} \sum_{l'' m''} e^{i\delta_{l''}} \sin \delta_{l''} B_{l_1 m_1, lm, l'' m''} B_{l_2 m_2, l'm', l'' m''} \quad (5.147)$$

are temperature independent factors and

$$B_{l_1 m_1, l_2 m_2, lm} = \int Y_{l_1 m_1}(\Omega) Y_{l_2 - m_2}(\Omega) Y_{lm}(\Omega) d\Omega, \quad (5.148)$$

with the conditions

$$\begin{aligned} m_1 - m_2 + m &= 0, \\ |l_2 - l| &\leq l_1 \leq |l_2 + l|, \\ l_1 + l_2 + l &= \text{even} \end{aligned} \quad (5.149)$$

for non-vanishing coefficients. Equations (5.149) and (5.150) define a temperature-dependent atomic scattering matrix which now contains non-zero off-diagonal terms, instead of the diagonal matrix for the case of isotropic displacements. These matrices can be inserted in conventional LEED programs requiring only slight changes to take care of the non-diagonal form.

The maximum number of phase shifts used is $l_{\max} + 1$. This sets the upper limit for the indices lm , $l'm'$ and $l''m''$, that is, $l'' \leq l_{\max}$ in Eq. (5.147). The limits set in Eq. (5.149) lead to

$$l_1 \leq 2l_{\max} \text{ and } l_2 \leq 2l_{\max}. \quad (5.150)$$

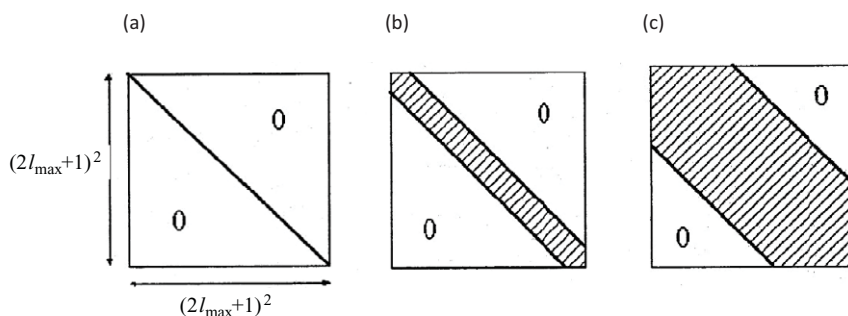


Figure 5.22 Off-diagonal terms in the matrix of the expansion coefficients $W_{l_1 m_1, l_2 m_2}$, which describe the thermal ellipsoid in angular momentum space (Eq. (5.142)); ‘0’ indicates vanishing matrix elements. (a) isotropic case, (b) small anisotropy with $u_x/u_y \leq 1.5$ and (c) larger anisotropy. Adapted from [5.91] W. Moritz and J. Landskron, “Thermal Vibrations at Surfaces Analysed with LEED”, in *Solid-State Photoemission and Related Methods*, W. Schattke and M. A. Van Hove, eds., Wiley-VCH, pp. 433–459, 2003, with permission from Wiley.

Thus, in the calculation of the expansion coefficients $W_{l_1 m_1, l_2 m_2}$ twice the number of angular momentum components are required compared to the partial wave expansion of the scattering amplitude, in which $l_{\max} + 1$ phase shifts are used. Asymmetry of the thermal ellipsoid produces non-zero off-diagonal terms in \mathbf{W} . Care must be taken to include a sufficient number of phase shifts if large anisotropies occur. In Figure 5.22 the off-diagonal terms in the matrix \mathbf{W} are schematically shown for three cases. A diagonal matrix occurs for the isotropic case, a narrow band of off-diagonal terms occurs for small anisotropy on the order of $u_x/u_y \leq 1.5$ and a broad band occurs for large anisotropy. If l_{\max} is chosen too small, the width of the band of off-diagonal terms exceeds $2l_{\max}$ and the thermal ellipsoid cannot be adequately described.

In the case of isotropic and harmonic vibrations, the result must be consistent with the conventional derivation leading to a diagonal matrix. For spherically symmetric vibrations all coefficients c_{n, l, m_c} vanish unless $(l_c, m_c) = (0, 0)$ which leads to $l_1 = l_2$ and $m_1 = m_2$ in Eq. (5.146) and thus to a diagonal form of the matrix of expansion coefficients (see Figure 5.22).

With

$$p(u) = (2\pi)^{-3/2} \langle u^2 \rangle^{-1/2} \exp\left(-\frac{u^2}{2\langle u^2 \rangle}\right), \quad (5.151)$$

$W_{l_1 m_1, l_2 m_2}$ becomes

$$W_{l_1 m_1, l_2 m_2} = 16\pi^2 \delta_{l_1 l_2} \delta_{m_1 m_2} \int R_n(\langle u^2 \rangle) (-1)^{l_1 + l_2} j_{l_1}(k \cdot \langle u^2 \rangle) j_{l_2}(k' \cdot \langle u^2 \rangle) u^2 du \quad (5.152)$$

and

$$D_{l_1 m_1, l_2 m_2, l m, l' m'} = \frac{2\pi}{k} \sum_{l'' m''} e^{i\delta_{l''}} \exp(i\delta_{l''}) \sin(\delta_{l''}) \delta_{l_1 m_1, l m} \delta_{l_2 m_2, l' m'}. \quad (5.153)$$

This leads to complex temperature-dependent phase shifts $\delta_l(T)$:

$$t_{lm,l'm'}(T) = -\frac{1}{k} \sum_{l_1 l''} i^{l_1} \exp(-2\langle u^2 \rangle k^2) j_{l_1}(-2i\langle u^2 \rangle k^2) \exp(i\delta_{l''}(T)) \sin(\delta_{l''}(T)) \\ \cdot \left(\frac{4\pi(2l_1+1)(2l''+1)}{(2l+1)} \right)^{1/2} B(l'', l_1, l), \quad (5.154)$$

which is the result derived by J. B. Pendry [5.1]; the imaginary part of $\delta_l(T)$ corresponds to the loss of coherent electron scattering due to the thermal disorder. The derivation is more convenient when the Fourier transform of the PDF is performed prior to the expansion in spherical harmonics, which immediately leads to the same result.

5.5.6 Multipole Expansion Coefficients for Harmonic Vibrations

It is neither convenient nor possible in practice to optimise the expansion coefficients $c_{n,lm}$ in Eq. (5.137) directly by fitting them to the experimental data. The appropriate approach is to use the conventional parameters of the thermal ellipsoid as free parameters in the analysis. This requires calculating the expansion coefficients as a function of the vibration amplitudes, which reduces the number of free parameters as well. For anisotropic harmonic vibrations there is a maximum number of six independent parameters which define the mean square displacements in three directions and give the orientation of the ellipsoid. The multipole expansion in Eq. (5.137), on the other hand, requires the radial functions and a large number of expansion coefficients; their number depends on the ratio of the displacement parameters.

We start from the isotropic case where only one parameter exists, the mean square displacement, while the distribution function is Gaussian. In this case,

$$p(\mathbf{u}) \propto \exp\left(-\frac{u^2}{\langle u^2 \rangle}\right), \quad (5.155)$$

and all the expansion coefficients but $c_{0,00}$ in Eq. (5.137) vanish. If we now assume anisotropy with

$$p(\mathbf{u}) \propto \exp\left\{-\left(\frac{u_x^2}{\langle u_x^2 \rangle} + \frac{u_y^2}{\langle u_y^2 \rangle} + \frac{u_z^2}{\langle u_z^2 \rangle}\right)\right\}, \quad (5.156)$$

the expansion of the ellipsoid in general requires higher order coefficients. In the expansion

$$p(\mathbf{u}) = \sum_{n,lm} c_{n,lm} R_n(u) Y_{lm}(\Omega_u) \quad (5.157)$$

all odd-order terms in l vanish because of the centrosymmetry. As the probability distribution is a real quantity, there are some restrictions for the complex coefficients $c_{n,lm}$:

$$c_{n,l_0} = \text{real},$$

$$c_{n,l-|m|} = \begin{cases} c_{n,l|m|}^* & \text{if } m = \text{even} \\ -c_{n,l|m|}^* & \text{if } m = \text{odd}. \end{cases} \quad (5.158)$$

To derive the expansion coefficients from the given parameters of the ellipsoid, we use the deviation from the isotropic average (neglecting prefactors):

$$p'(\mathbf{u}) = p(\mathbf{u}) - \exp\left(-\frac{u^2}{\langle u^2 \rangle}\right), \quad (5.159)$$

and calculate

$$c_{n,lm} R_{n,lm}(\langle u \rangle) = \int p'(\mathbf{u}) Y_{lm}(\Omega_u) d\mathbf{u}. \quad (5.160)$$

The probability density function $P(\mathbf{u})$ for harmonic vibrations is given by [5.78]:

$$P(\mathbf{u}) = \frac{1}{\sqrt{8\pi^3 \langle u_x \rangle^2 \langle u_y \rangle^2 \langle u_z \rangle^2}} \exp\left(-\frac{1}{2} \left[\frac{u_x^2}{\langle u_x^2 \rangle} + \frac{u_y^2}{\langle u_y^2 \rangle} + \frac{u_z^2}{\langle u_z^2 \rangle} \right]\right), \quad (5.161)$$

where $\langle u_x \rangle^2$, $\langle u_y \rangle^2$ and $\langle u_z \rangle^2$ are the mean square displacements in the x -, y - and z -directions. If the atoms sit in surface sites with 3-, 4- or 6-fold symmetry, only two parameters remain, frequently denoted by u_{\parallel} and u_{\perp} .

The appropriate radial functions for a Gaussian distribution are

$$R_0(u) = \frac{1}{(2\pi\sigma_0^2)^{3/2}} \exp\left(-\frac{u^2}{2\sigma_0^2}\right), \quad (5.162)$$

$$R_n(u) = \frac{u^2}{(2\pi\sigma_n^2)^{3/2}} \exp\left(-\frac{u^2}{2\sigma_n^2}\right), n \geq 1. \quad (5.163)$$

The expansion coefficients $c_{n,lm}$ and the widths of the radial functions σ_n can be determined from the inverse relation

$$\sum_{n,lm} c_{n,lm} R_n(u) = \int d\Omega_u P(\mathbf{u}) Y_{lm}(\Omega_u). \quad (5.164)$$

The parameters of the vibration ellipsoid, u_x , u_y and u_z , are fit parameters in the LEED calculations; both the expansion coefficients and the radial functions are calculated in each iteration step from these parameters. The number of expansion coefficients needed to match the Gaussian shape of the PDF depends on the anisotropy of the vibration ellipsoid and on the electron energy through the Bessel functions in Eq. (5.141). In the calculations for CO/Ru(0001) shown in Section 5.5.9, two radial functions R_0 and R_1 with $l_{\max} = 12$ are found to be sufficient.

The orientation of the ellipsoid of the thermal vibration provides another three degrees of freedom. The rotation of the ellipsoid can be performed by rotator functions for the atomic t -matrix [5.89]:

$$t_{l_1 m_1, l_2 m_2}^{rot} = \sum_{m' m''} D_{m_1 m'}^{(l_1)}(\alpha \beta \gamma) t_{l_1 m', l_2 m''} D_{m_2 m''}^{(l_2)*}(\alpha \beta \gamma), \quad (5.165)$$

where α, β, γ are the Euler angles of the rotation. The calculation of the rotation operators $D_{mm'}^{(l)}(\alpha \beta \gamma)$ can be found in textbooks on quantum mechanics (e.g., [5.93]); a computer program for the rotation of t-matrices has been published by M. Blanco-Rey et al. [5.94; 5.95].

When an ellipsoid with large anisotropy must be represented in the multipole expansion, terms with higher order l, m are required. When a limited order of coefficients is given it is also convenient to obtain the expansion coefficients by an optimisation procedure to approximate the expanded distribution to a Gaussian with given parameters.

The shape of the PDFs which can be obtained with a given number of angular momentum components is illustrated in Figure 5.23. We see that a small number of angular momentum components is totally inappropriate to describe a PDF with high anisotropy. This circumstance is not specific to the multipole expansion and cannot be overcome by alternative formulations using a spherical wave expansion.

5.5.7 Multipole Expansion Coefficients for Anharmonic Vibrations

The expansion in Eq. (5.137) allows using non-Gaussian PDFs, so that one can easily treat anharmonic vibrations as well. It also allows describing static displacements by choosing the appropriate expansion coefficients in accordance with the local symmetry of the site. A priori there are no assumptions whether the vibrating atoms move in a harmonic potential or not. As the PDF is determined by the atomic potential within which the atom vibrates, anharmonic contributions to the one-particle potential can be analysed in terms of the resulting PDF itself. Anharmonic vibrations produce a deviation of the PDF from a Gaussian. Two examples are shown in Figure 5.24. As the parity of the spherical harmonics is $(-1)^l$, that is, $Y_{lm}(\pi - \vartheta, \varphi + \pi) = (-1)^l Y_{lm}(\vartheta, \varphi)$, a generalised, non-Gaussian PDF can be expanded as a sum of centrosymmetric and antisymmetric components (the radial functions are always centrosymmetric):

$$p(\mathbf{u}) = \sum_n R_n(u) \left(\sum_{lm} c_{n,lm} Y_{lm}(\vartheta, \varphi) + \sum_{l'm'} c_{n,l'm'} Y_{l'm'}(\vartheta, \varphi) \right), \quad (5.166)$$

with even l and odd l' . The antisymmetric contributions represent an anharmonic distortion of the Gaussian, while they shift the first moment (mean) of the PDF which corresponds to the averaged position of the vibrating atom.

Anharmonic deviations caused by the centrosymmetric components of the distribution function leave the atomic position unchanged but affect the even moments of the distribution and therefore the mean square amplitude in a given direction. In this way the shape of the ellipsoid of thermal vibrations is modified, for example, with lobes constrained by local symmetry of the surface atom, cf. Figure 5.24. By

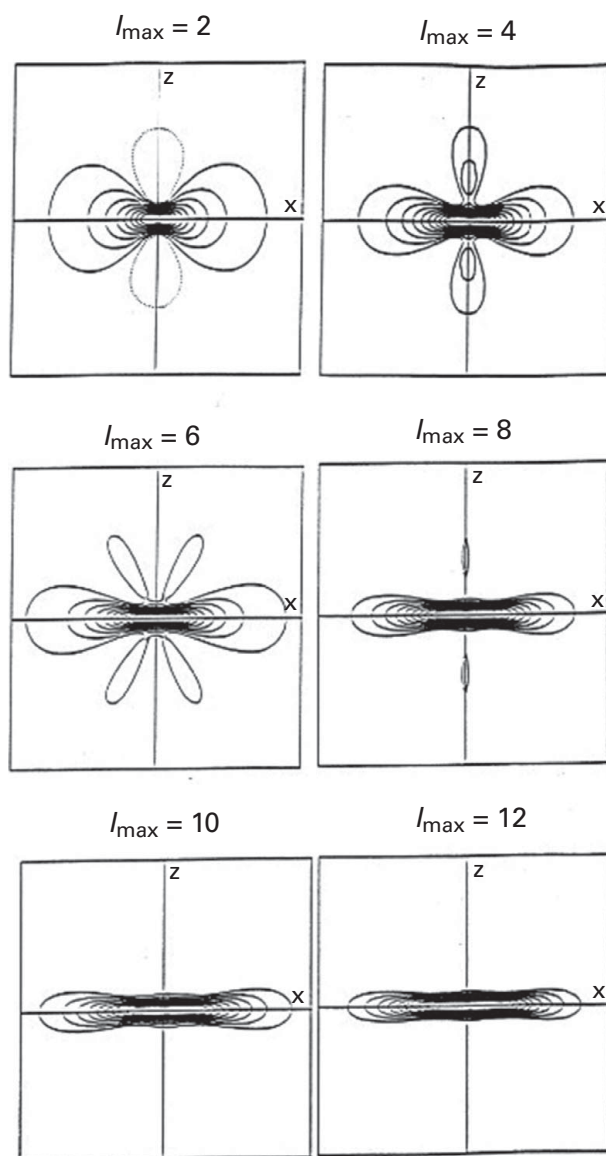


Figure 5.23 Illustration of the influence of the maximum number of angular momentum components of the shape of the PDF; $l_{\max} = 12$ in the expansion, Eq. (5.157), is the minimum number required to approximate an ellipsoid with an axis ratio of 1:10. Reprinted from [5.91] W. Moritz and J. Landskron, "Thermal Vibrations at Surfaces Analysed with LEED", in *Solid-State Photoemission and Related Methods*, W. Schattke and M. A. Van Hove, eds., Wiley-VCH, pp. 433–459, 2003. With permission from Wiley.

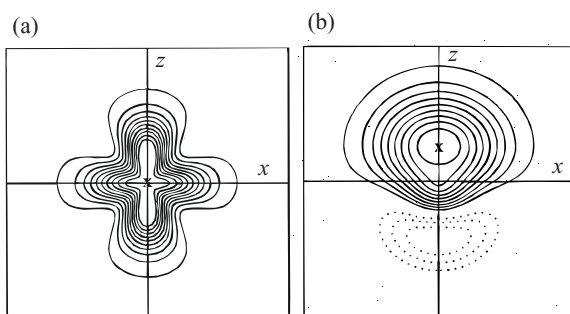


Figure 5.24 Examples for PDFs resulting from an anharmonic one-particle potential, presented as sections of the PDF in the x - z plane. (a) A PDF obtained from even order coefficients up to quadrupole terms in Eq. (5.166). The $l = \text{even}$ coefficients produce a centrosymmetric distribution. (b) The shift of the mean position due to an odd-order coefficient $c_{0,10} \neq 0$. The dotted lines correspond to negative PDF. Reprinted from [5.91] W. Moritz and J. Landskron, “Thermal Vibrations at Surfaces Analysed with LEED”, in *Solid-State Photoemission and Related Methods*, W. Schattke and M. A. Van Hove, eds., Wiley-VCH, pp. 433–459, 2003. With permission from Wiley.

considering anharmonic effects, the number of non-vanishing off-diagonal elements in the atomic t -matrix increases in comparison to the harmonic case.

5.5.8 Example: Cu(110)

The multipole expansion of the probability density function is the appropriate way to introduce anisotropic and anharmonic thermal vibration into the multiple scattering formalism. The averaged non-diagonal scattering matrices can be used in conventional LEED codes without large changes, as well as for XPD, NEXAFS, or other spectroscopic methods. The computational effort can be reduced by using symmetries in real space and separate calculation of structural and thermal parameters, as both sets of parameters can be separately optimised in most cases.

As an example, anisotropy of the thermal motion was determined from temperature dependent LEED I(V) measurements of the clean Cu(110) surface, cf. Figure 5.25.

In the first step of the analysis, isotropic vibrations were assumed. The result for the rms displacements in the first three layers is shown in Figure 5.26(a).

The analysis optimised the four outermost layer distances, as well as rms displacements in the outermost three layers. In the second step anisotropic displacements were allowed only in the top layer, cf. Figure 5.26(b). Isotropic displacements could in principle be determined using Pendry’s R-factor in which the scale factors for the intensities disappear, since the logarithmic derivative of the intensities is used in the Y-function. However, in the analysis of anisotropic displacements it is necessary to use a common scale factor for all I(V) curves, so the R-factor R_2 was chosen since it directly compares the intensities.

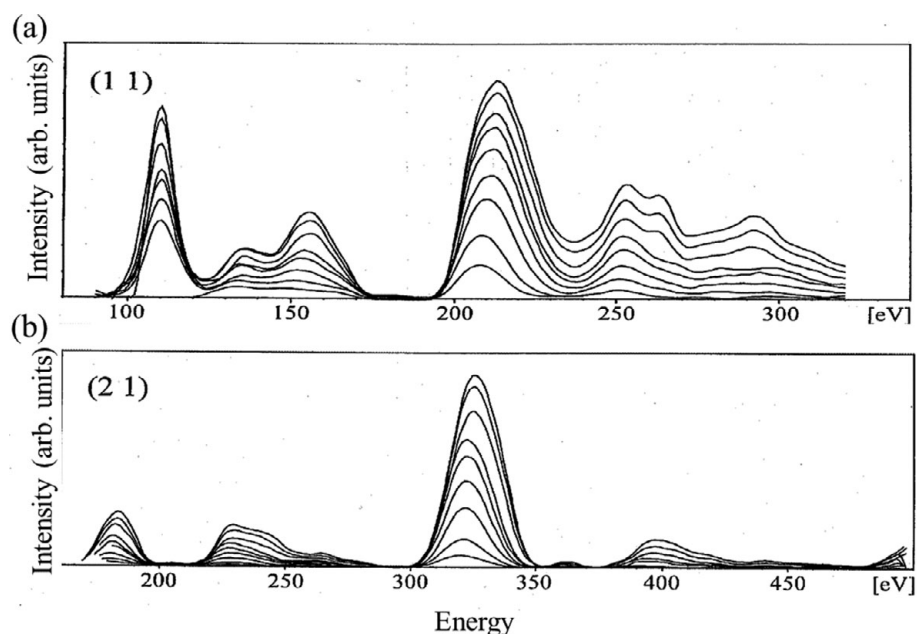


Figure 5.25 Experimental $I(V)$ curves from Cu(110) for (a) the (11) beam and (b) the (21) beam at nine temperatures from 110 K (uppermost curves) to 465 K (lowest curves). Reprinted from [5.91] W. Moritz and J. Landskron, “Thermal Vibrations at Surfaces Analysed with LEED”, in *Solid-State Photoemission and Related Methods*, W. Schattke and M. A. Van Hove, eds., Wiley-VCH, pp. 433–459, 2003. With permission from Wiley.

The results show clearly an enhancement of the displacement amplitudes in the [100] direction, cf. Figure 5.27, from about 0.011 nm (0.11 Å) in the $[1, \bar{1}, 0]$ direction to about 0.014 nm (0.14 Å) in the [100] direction, in agreement with theoretical calculations and with ion scattering results. The amplitudes normal to the surface are approximately the same as determined assuming isotropic vibrations.

5.5.9 Example: $\text{Ru}(0001) + (\sqrt{3} \times \sqrt{3})\text{R}30^\circ\text{-CO}$

As an example of anisotropic thermal motion in adsorbate layers, the structure of CO molecules on Ru(0001) has been investigated by temperature-dependent LEED measurements [5.76]. In its $(\sqrt{3} \times \sqrt{3})\text{R}30^\circ$ structure, CO stands perpendicular to the Ru(0001) surface, bonding through C to a top site; it occupies one third of the top sites and thus induces a slight out-of-plane buckling in the outermost Ru layer. The structure model and the notation of the parameters used in the analysis of rms displacements are shown in Figure 5.28.

The $I(V)$ analysis was performed with both isotropic and anisotropic displacements. The geometrical results are practically identical. The possibility of anisotropy in the vibration of the topmost Ru atoms has been checked as well, although it seems *a priori* unlikely. No indications were found for such anisotropy, so that for all substrate

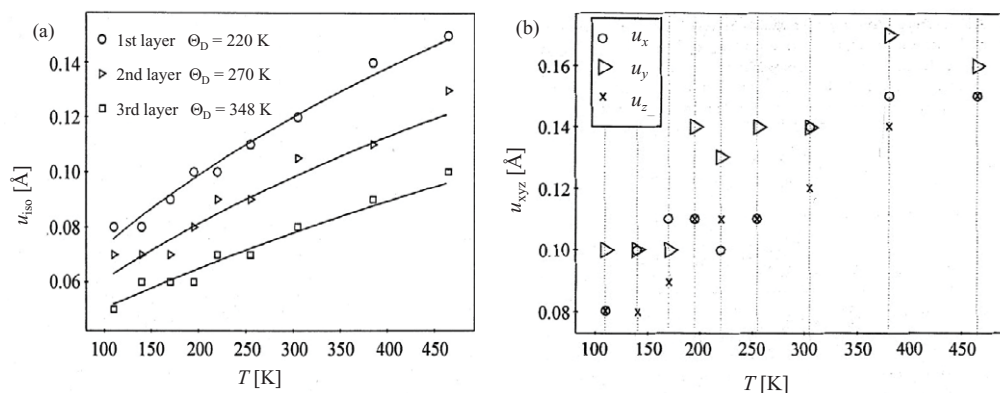


Figure 5.26 (a) Results of the vibration analysis of Cu(110) with isotropic displacements, showing rms displacements in the three outermost layers as a function of temperature; the values of Θ_D have been fitted for the top three layers and the corresponding u_{iso} are obtained through Eq. (5.118). (b) Results of the analysis with anisotropic displacements in the outermost layer (but isotropic displacements in the second and third layers); u_x and u_y are parallel and normal, respectively, to the ridges in the surface, while u_z is normal to the surface. Reprinted from [5.91] W. Moritz and J. Landskron, “Thermal Vibrations at Surfaces Analysed with LEED”, in *Solid-State Photoemission and Related Methods*, W. Schattke and M. A. Van Hove, eds., Wiley-VCH, pp. 433–459, 2003. With permission from Wiley.

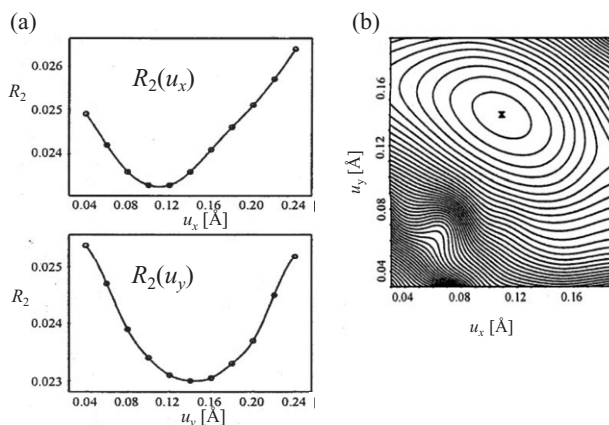


Figure 5.27 R-factor R_2 as a function of the lateral displacements of the Cu atoms in the top layer of Cu(110). (a) In the directions $[1\bar{1}0]$ (u_x) and $[100]$ (u_y). (b) Contour plot of the R-factor, where \times marks a minimum. Reprinted from [5.91] W. Moritz and J. Landskron, “Thermal Vibrations at Surfaces Analysed with LEED”, in *Solid-State Photoemission and Related Methods*, W. Schattke and M. A. Van Hove, eds., Wiley-VCH, pp. 433–459, 2003. With permission from Wiley.

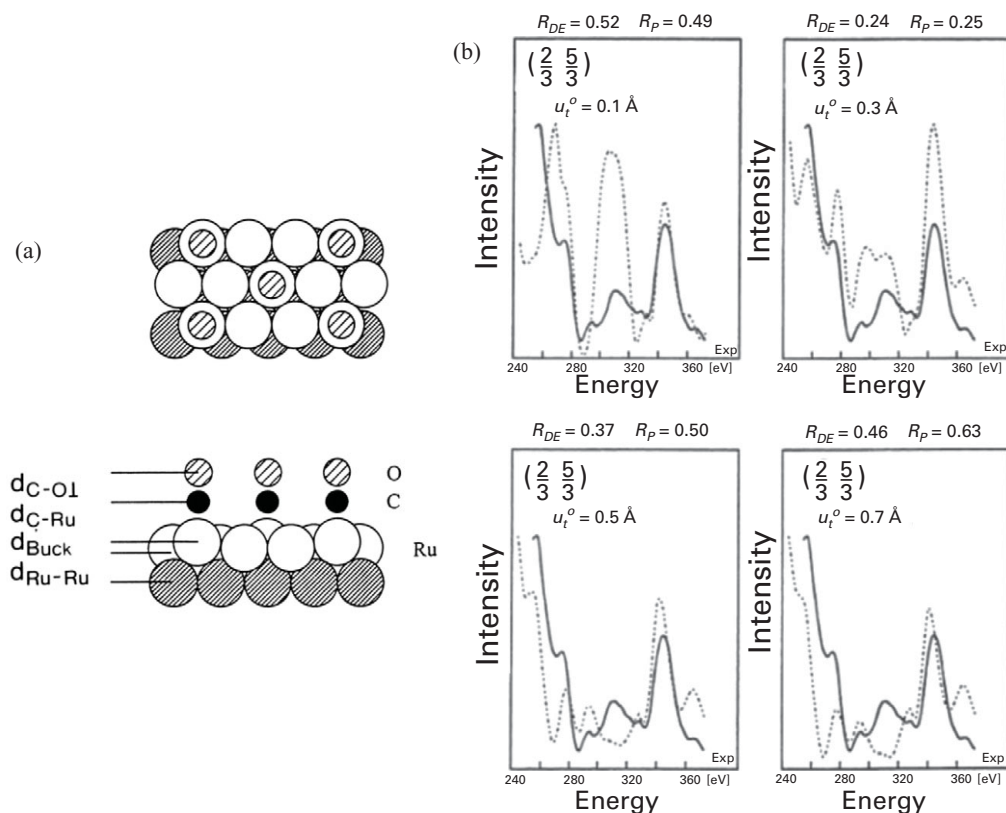


Figure 5.28 (a) Model of the $(\sqrt{3} \times \sqrt{3})R30^\circ$ structure of CO on Ru(0001), with top view in the upper panel and side view in the lower panel showing layer spacings. (b) I(V) curves of the $(2/3, 5/3)$ beam illustrating the influence of the rms displacements of oxygen parallel to the surface: solid lines are experimental, dashed lines theoretical best fits. Shown are four calculated I(V) curves where the parallel vibration amplitude of oxygen is kept fixed at values between 0.1 and 0.7 Å, as indicated in the figure. The peak positions fit best at 0.3 Å. All other structural parameters are optimised and all data were used in the analysis. Reprinted from [5.76] J. Landskron, W. Moritz, B. Narloch, G. Held, and D. Menzel, *Surf. Sci.*, vol. 441, pp. 91–106, 1999, with permission from Elsevier.

layers isotropic vibrations were used in the final analysis. The best-fit Debye temperatures were 310 K in the top substrate layer and 410 K in the second and subsequent layers. For each temperature, the perpendicular and parallel components of the displacement parameters for C and O were optimised. Note that in this treatment the motions of C and O are independent of each other, which is probably not quite realistic, as C and O likely have correlated motions due to their strong mutual bonding. Two R-factors were used to compare theory to experiment, R_1 and R_P (defined in Section 6.1.2), both leading to practically the same result. R_1 is the average of the absolute values of the difference to the experimental data. The R-factors show a

noticeably better agreement between experimental and calculated data with anisotropic rather than isotropic vibrations. With isotropic vibrations the R-factor is $R_p = 0.29$ at 25 K and increases to 0.39 at 350 K, while with anisotropic vibrations the optimum values for R_p are 0.26 at 25 K and 0.34 at 350 K, showing significant improvement.

The increase of the R-factors with temperature could be the result of anharmonicity, that is, a non-Gaussian probability density or a dependence of the lateral vibrational amplitude on the azimuthal direction in-plane. A 3-fold shape of the PDF in-plane would not be allowed in the harmonic approximation and for an atom in a 3-fold coordinated site. By inclusion of higher-order terms in the multipole expansion it was tested whether a deviation from the lateral isotropy in the PDF could be detected, but no significant improvement was found. From previous ESDIAD results [5.96] it is indeed not expected that preferential directions exist for the vibration parallel to the surface. Nevertheless, it is conceivable that the actual correlated motion of the C and O atoms is important, although this was not considered in this LEED analysis. The remaining deviation from ideal fit could also result from defects, whose number increases with temperature. Some discussion about correlated motion and estimates of errors is given by E. Prince [5.85] which refers to the kinematic theory. The applicability to the multiple scattering theory in LEED has not yet been investigated.

The results for the temperature dependence of the vibration amplitudes are shown in Figure 5.29. All amplitudes increase with temperature. The parallel rms displacement for the oxygen atom is noticeably larger than that for the carbon atom except for the lowest temperature where both amplitudes are equal. Both parallel components are larger than the perpendicular components, as one would expect. After optimising the thermal vibrations, the structural parameters were optimised again, but no deviations were detected within the error limits. To show how sensitive the superlattice intensities are to the thermal parameters, $I(V)$ curves for the (2/3, 5/3) beam are shown in Figure 5.28(b), together with the corresponding R-factors for this particular beam. The displacements do not reach the zero-point motion at low temperatures, which indicates the presence of static contributions to the displacements, probably resulting from point defects and steps.

5.6 From Calculated Amplitudes to Intensities

We connect here the wave amplitude to the diffracted intensity, that is, calculation to experiment. Equation (2.49) provided this link for the kinematic theory, where structure factor and lattice factor can be decoupled for identical atoms. We must generalise that result to the case of multiple scattering in the dynamical theory.

Assume an incident plane wave $A_{\text{in}} e^{i\mathbf{k}_{\text{in}} \cdot \mathbf{r}}$ and a diffracted plane wave $A_{\text{out}} e^{i\mathbf{k}_{\text{out}} \cdot \mathbf{r}}$, where A_{in} is usually set to unity, while A_{out} can come from \mathbf{T} of Eq. (5.17) (in the case

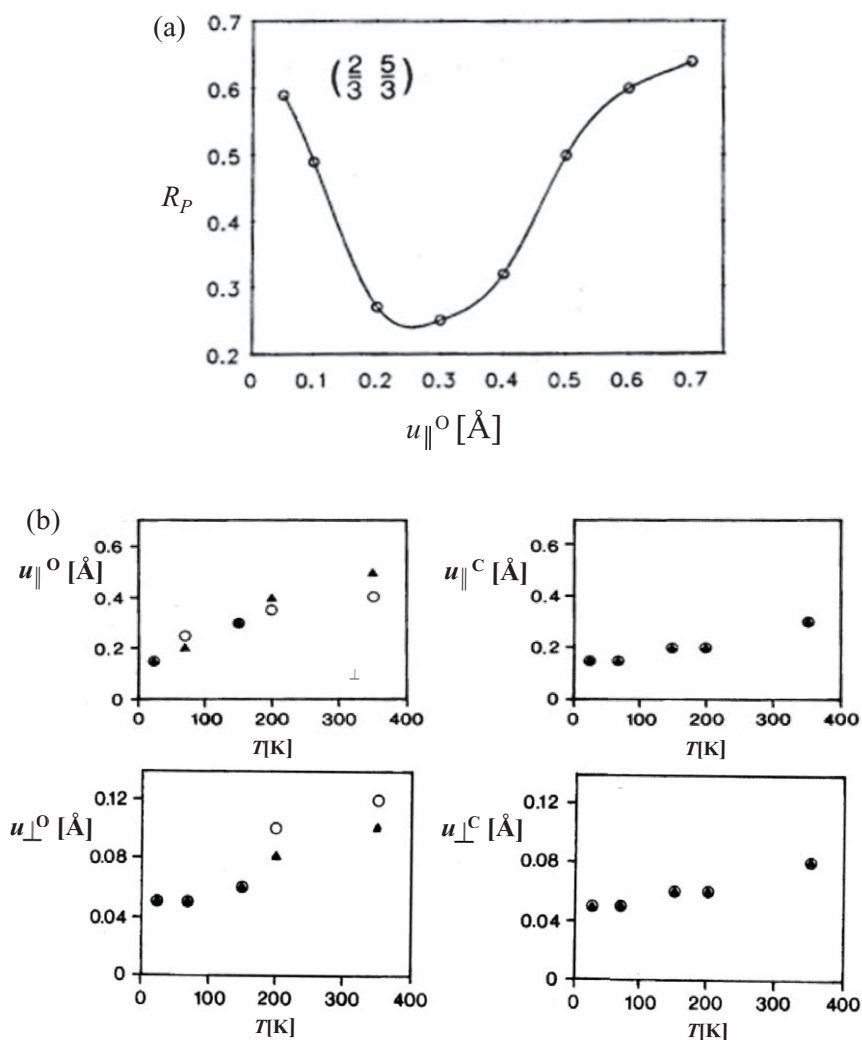


Figure 5.29 (a) Pendry R-factor of the $(2/3, 5/3)$ beam as function of the parallel displacement of the O atoms in $\text{Ru}(0001) + (\sqrt{3} \times \sqrt{3})\text{R}30^\circ\text{-CO}$. (b) Displacements of O and C parallel and normal to the surface as a function of temperature. All experimentally available beams were used in the analysis. Reprinted from [5.76] J. Landskron, W. Moritz, B. Narloch, G. Held, and D. Menzel, *Surf. Sci.*, vol. 441, pp. 91–106, 1999, with permission from Elsevier.

of divergent outgoing waves, as for diffraction from a nanocluster, \mathbf{k}_{out} gives any chosen outgoing direction). For plane waves, the quantities $k|A_{\text{in}}|^2$ and $k|A_{\text{out}}|^2$, where $k = |\mathbf{k}_{\text{in}}| = |\mathbf{k}_{\text{out}}|$ are the fluxes in the incident and diffracted beams (or directions), namely the number of electrons per unit time crossing through a unit area oriented perpendicular to the direction of electron motion. For plane waves and a planar surface, the fluxes integrated over the beam cross-sections are then, in

the theory, $Ck|A_{\text{in}}|^2$ and $Ck|A_{\text{out}}|^2(\cos \vartheta_{\text{out}}/\cos \vartheta_{\text{in}})$, respectively, where C is the cross-section of the incident beam and $C(\cos \vartheta_{\text{out}}/\cos \vartheta_{\text{in}})$ the corresponding cross-section of the diffracted beam, given the polar angles of incidence ϑ_{in} and of emergence ϑ_{out} relative to the surface normal. The theoretical reflectivity R^{calc} of the surface thus becomes

$$R^{\text{calc}} = \frac{\cos \vartheta_{\text{out}}}{\cos \vartheta_{\text{in}}} \frac{|A_{\text{out}}|^2}{|A_{\text{in}}|^2}. \quad (5.167)$$

The equivalent experimental reflectivity, to which the theoretical reflectivity of Eq. (5.167) should be compared, is the ratio of the measured intensity (current) I_{out} of a diffracted beam to that of the incident beam, I_{in} :

$$R^{\text{exp}} = \frac{I_{\text{out}}}{I_{\text{in}}}. \quad (5.168)$$